AEROSPACE RESEARCH IN BULGARIA

Volume 27, Sofia, 2015
Space Research and Technology Institute
Bulgarian Academy of Sciences

Editorial Board

Address

AEROSPACE RESEARCH IN BULGARIA
Space Research and Technology Institute
bl. 1, *Acad. G. Bonchev* St., Sofia 1113, Bulgaria

e-mail: journal@space.bas.bg

Pre-Publication Processing
Tsveta Srebrova

ISSN 1313 – 0927

This issue of *Aerospace Research in Bulgaria* is published with financial support from the Bulgarian National Science Fund – Contract No ДНП 04/85

Bulgarian Academy of Sciences **ISSN 1313 – 0927**

Aerospace Research in Bulgaria

27

Sofia, 2015

Contents

Hypotheses

New books

СЪДЪРЖАНИЕ

Хипотези

Нови книги

Bulgarian Academy of Sciences. Space Research and Technology Institute.
Aerospace Research in Bulgaria. 27, 2015, Sofia

COSMOLOGICAL MODEL OF BUBBLE MULTIVERSE

Alexander Yosifov

e-mail: alexander_yosifov@abv.bg

Abstract

The conventional singular hot Big Bang scenario is questioned. A new model which does not include an initial singularity ($g_{00}=\infty$ *at* $t=0$)*, neither a brief period of exponential expansion* $a(t)\sim e^{Ht}$ *is considered. The main parameters* T *and* ρ *are kept finite. The proposed cosmological picture represents our Universe as part of a multiverse. The beginning of the Universe we occupy is revisited in the framework of quantum field theory in curved spacetime. However, a straightforward alternative mechanism for not only solving the most fundamental problems in modern cosmology – flatness problem, horizon problem and magnetic monopole problem, but even suppressing their number is provided. In the particular paper I discuss the very nature of the spacetime and the apparent contradiction between quantum mechanics and general relativity in terms of a classical field theory in 3+1 dimensions.*

Introduction

For the past decades the prevailing view, regarding the beginning of the universe and its evolution in the first fraction of a second, has been a combination of the big bang theory and the theory of cosmic inflation [1]. However, recently this paradigm has been challenged. According to The Big Bang Theory (TBBT), if we extrapolate the current picture of the Universe backwards in time, temperature T and density ρ start increasing until we reach the initial singularity $g_{00}=\infty$ at the beginning of time $t=0$. At that moment the whole Universe is compressed to a single point of zero size, $t\rightarrow 0$ and $a(t)\rightarrow 0$ while $T\rightarrow\infty$ and $\rho\rightarrow\infty$. At this point our laws of physics break down. The central problem of TBBT is namely the singularity. Furthermore, the theory does not provide any explanation regarding the initial conditions. The model is completely ignorant about the events prior to the expansion phase as neither space, nor time existed.

The theory of cosmic inflation states that right after the Big Bang the universe went through a brief period, 10^{-36}s, of superluminal exponential expansion $a(t)\sim e^{Ht}$. The concept was originally pioneered to smooth and flatten the Universe, starting from random initial conditions, and thus solve the horizon, flatness and magnetic monopole problems with a straightforward mechanism. The conventional theory dictates that in order for inflation to be triggered, a scalar field ϕ, *inflaton*, satisfying the property $V(\phi) >> E_k$ has to be present. Because of the small kinetic energy E_k, the inflaton ϕ settles down to a state of potential well adiabatically. Once the scalar field ϕ is settled, the potential energy $V(\phi)$ starts dominating. When the potential takes over, the Lagrangian $L = E_k - V(\phi)$, becomes negative and the universe starts expanding. The measure of the expansion, *e-folds*, is given by $\frac{a(t_f)}{a(t_i)}=e^N$, where $a(t_f)$ and $a(t_i)$ is the scale factor after and prior to inflation, respectively. The number of *e-folds*, N, is defined as $N \equiv (t_f - t_i)H$, where $H = \dot{a}/a$, is the Hubble parameter. Large kinetic energy value would prevent inflation from initiating. I am not going to provide a detailed description of inflation; neither will I examine its different models, as this is not of interest to the particular paper. Great effort in this direction has been devoted in the past [2-4]. However, this view has to be abandoned. Recent data, gathered by the Planck satellite [5], seriously questions the paradigm. A subsequent paper, based on the obtained results, [6], shows problems with inflation that until now were not present. According to the data, for inflation to start smoothing and flattening the Universe, it has to have extremely low initial anisotropy prior to the exponential expansion phase. Moreover, *Planck*2013 rules out most of the inflationary models and favors only the simple ones [7-9]. It shows we live in an amazingly elegant Universe; the spatial curvature is negligible and the fluctuations are Gaussian. The overall data, collected by *Planck* satellite, calls for a new and simple description of the Universe. The contemporary cosmological model suffers from many problems which force us to rethink our understanding concerning the early history of the Universe. I discuss an alternative non-singular and inflation-free model which predicts finite values for both space and time. The proposed picture is simple in a sense that it does not require the addition of n compacted extra dimensions. The model eliminates the flatness of the spacetime geometry as a problem, and solves both of the remaining ones, horizon and monopoles problems, with a straightforward mechanism motivated by certain string theory models.

Bubble multiverse

I will describe a scenario which provides a non-inflationary solution to the horizon and magnetic monopoles problems. The Bubble Multiverse (BM) suggests our Universe is part of an Multiverse. The model represents each Universe as a separate 3+1 dimensional bubble, described by the Friedmann-Robertson-Walker (FRW) metric

$$\mathrm{d}s^2=-\mathrm{d}t^2+a^2(\mathrm{t})\left[\frac{dr^2}{1-kr^2}+r^2 d\Omega^2\right]\equiv g_{\mu\nu}\mathrm{d}x^\mu \mathrm{d}x^\nu, \tag{1}$$

where $\Omega^2 = d\Theta^2 + sin^2\Theta d\phi^2, k = +1,$ in which case the scale factor $a(t)$ becomes the radius curvature of space, denoted as $R(t)$. Einstein's equation for the particular metric reads

(2) $$G_\mu^\nu=\frac{8\pi G}{3}T_\mu^\nu,$$

where T_μ^ν is the energy-momentum tensor. The Friedmann equation for the evolution of the FRW universe is provided by (3):

(3) $$(\frac{\dot{a}}{a})^{\wedge}2=H(t)^{\wedge}2=\frac{8\pi G}{3c^2}\varepsilon(t)-\frac{kc^2}{R_0^2a(t)},$$

where $k = +1$, $\varepsilon(t)$ is the energy density and $a(t)$ is the FRW scale factor. Initial homogeneity and isotropy of the Universe on large scales (>100 Mpc) is assumed. The bubbles are taken to propagate in a quantum vacuum background and interact only via gravity. Hence, we suppose different bubbles can approach each other. This is a semi-classical theory, matter fields are quantized and gravity is treated classically. In the presence of a gravitational source, the spacetime geometry becomes non-Euclidean, thus allowing for trivial description of the dynamics using Einstein's field equation

(4) $$G_{\mu\nu}=8\pi\langle T_{\mu\nu}\rangle$$

Given the metric of the spacetime, depending on the matter and radiation density one might expect the universe to reach a maximum size R_{max} and then start contracting or keep expanding forever *a(t)* -> ∞ as *t->0.* In the framework we describe, it is more convenient to assume finite size of the different universes. It is therefore plausible, I believe, to assume every single bubble has a boundary layer exhibiting superfluid properties. Numerous experiments with superfluids have been done in the last couple of decades [10-12]. Of particular interest is He-3, a type of Fermi superfluid. It has proved to be extremely useful medium for studying the effects of quantum field theory and high-energy physics. Furthermore, superfluid He-3 is a good environment for mimicking event horizons of black holes [13-15]. As a result, when two "parent" universes come close together, due to the superfluid properties of their shells, a force of repulsion, that overcomes the force of gravity, occurs. Hence, the bubbles repel each other. Because of the strong gravitational field, generated by the two universes, the quantum vacuum *in-between* gets polarized. The idea of vacuum polarization in the presence of a strong gravitational field was presented by Stephen Hawking [16]. He proved mathematically that at the vicinity of its horizon, $g_{00} = 0$, a black hole polarizes the quantum vacuum under the influence of its own gravitational field, which leads to an increase of the local energy density of the quantum fluctuations $\delta\phi$, hence pairs of positive frequency oscillations are produced. The expectation value of the field fluctuations in curved spacetime is given by $\langle\phi^2\rangle$. The change of the area of the event horizon due to the particle absorption, is non-negative. Consequently, high frequency outgoing modes of the quantum field, Hawking radiation, are emitted to infinity and the black hole evaporates. A static black hole emits Hawking quanta with a black body thermal spectrum of temperature $T=\frac{\hbar c^3}{8\pi GM}$, where $\hbar$ is the reduced Planck constant. Because of the quantum nature of the environment, Quantum Field Theory in Curved Spacetime (QFTCS) is the framework behind the mechanism for creating a new Universe in the particular paradigm. The no-hair theorem [17-18] implies black holes are indistinguishable from one another. It posits they are entirely described by three classical parameters – angular momentum *J*, charge *Q*, and mass *M*. The theorem states that all of the information regarding the matter that has collapsed to form the black hole is trapped behind the event horizon and is inaccessible to the external observers. Similarly, bubble universes can be described by the same parameters. This line of reasoning allows us to assume the boundary surface of an individual bubble is a flat surface. This was first proposed by G.'t Hooft in the context of the holographic principle. I have come to the same conclusion based on completely different arguments from black hole physics which suggests the proposed view might have deep implications. Furthermore, since both the boundary layer of an Universe and the event horizon of a black hole are flat surfaces and polarize the vacuum in their vicinity, an analogy between them could be made. Describing the quantum vacuum polarization in the spacetime region *between* two bubble universes, we apply the Hermitian operators $\Psi^\dagger$(x) and Ψ(x) to the scalar field ϕ. They are defined as follows (5):

$$(5) \qquad \Psi^\dagger(x) = \sum_i \Psi_i^*(x)\, a_i^+, \qquad \Psi(\mathrm{x}) = \sum_i \Psi_i(x)\, a_i,$$

where $a_i^\dagger$ and a_i are the creation and annihilation operators, respectively. When we apply a creation operator on the lowest possible energy state, the vacuum $|0>$, we get (6)

$$(6) \qquad a_i^+|0> = |x> .$$

We find that a positive frequency oscillation is produced at point x. This is due to the instability of the quantum vacuum in the presence of a strong gravitational field. The initial vacuum will not appear entirely particle-free to all observers. An annihilation operator, acting on the vacuum yields

(7) $$a_i|0>=|0> \text{ for } \forall \text{ states.}$$

The number of particles in this case is not globally determined but rather observer-dependent. The expectation value of the particle production is given by

(8) $$\langle N_i\rangle=\langle 0|a_i^\dagger a_i|0\rangle,$$

where N_i is the number operator and it is defined as $N_i=a_i^\dagger a_i$. We expand the creation and annihilation operators by a Bogoliubov transformation

(9) $$a_i=\sum_j(\alpha_{ij}^* a_j-\beta_{ij}^* a_j^\dagger),$$

where α_{ij} and β_{ij} are the Bogoliubov coefficients. The scalar fields are time-independent; they solely depend on position. Therefore, we assign a Hermitian operator to every point in space

(10) $$\Psi^\dagger(x)=\sum_i \Psi_i^*(x)a_i^+.$$

We can calculate the density by applying the operators $\Psi^\dagger(x)$ and $\Psi(x)$. Integrating over a particular region allows us to find the approximate number of particles in the given volume of space

(11) $$\int dx\, \Psi^\dagger(x)\Psi(x)$$

(11.1) $$\int dx \sum_{ij} a_i^\dagger\Psi_i^*(x)a_j\Psi_j\,(x)$$

(11.2) $$\sum_{ij} a_i^\dagger\, a_j\delta_{ij}\ \ .$$

Due to the quantum nature of the process, the number varies. The Dirac delta function shows continued distribution. We can now proceed and calculate the energy density in the present region. I will start by first considering the more familiar example with only one particle. The energy of each produced quanta is given by the time-independent one-particle *Schrödinger* equation

(12) $$\Psi_i H = \Psi_i \omega,$$

where H is the Hamiltonian. Substituting H in equation [(8)] gives us

(12.1) $$\Psi_i \left[\frac{-\hbar^2}{2m}\boldsymbol{\nabla}^2 + V(\phi)\right] = \Psi_i \omega_i,$$

where $\boldsymbol{\nabla}^2$ is the Laplace operator and in 3D Cartesian coordinates yields the form

(13) $$\boldsymbol{\nabla}^2 = \frac{\partial^2}{\partial x^2} + \frac{\partial^2}{\partial y^2} + \frac{\partial^2}{\partial z^2}\ .$$

Hence, by applying Hermitian operators to the Hamiltonian of each one-particle state we find the total amount of energy in a given region of space to be

(14) $$E = \int dx\, \Psi^+(x) \left[\frac{-\hbar^2}{2m}\boldsymbol{\nabla}^2 + V(\phi)\right] \Psi(x).$$

Let me now consider the many-particles case. Despite we are now dealing with a more complex system, consisting of N number of particles, and one might expect it to be more complicated, we do, however, apply the same formalism as in equation [(12.1)]

(15) $$H = -\frac{\hbar^2}{2}\sum_i^N \frac{\boldsymbol{\nabla}^2{}_i}{m_i} + V(\phi),$$

where the dot product of the del operator denotes the kinetic energy of the N-particle system. The above-developed concept creates the initial causally connected patch of matter which will later expand to become our Universe. We initially begin with a non-zero value of the scale factor $a(t)$, thus we avoid the formation of a cosmic singularity and keep the parameters ρ and T finite. The matter patch is in low entropy state and must satisfy the extremely low initial anisotropy condition in order for expansion to be initiated. Considering an inflation-free model, depending chiefly on the initial expansion rate Λ, leads to two extreme possible scenarios in the early universe: (i) adiabatic expansion and (ii) very rapid initial expansion, corresponding to $\Lambda << 1$ and $\Lambda >> 1$, respectively. In the first case, the critical value of the density ρ_{crit} will be exceeded quickly, thus gravitational attraction will take over, resulting in an immediate collapse. Whereas in the second case, numerous Planckian-size low entropy state horizons will form, each of which containing several bits of information. In both cases the lifespan of the Universe will be incredibly short; thus being, for all practical purposes, meaningless. Aside from the extreme scenarios, for the Universe to grow and form large-scale structures, the initial expansion Λ, has to take an arbitrary value somewhere between the extreme velocities (16)

(16) $$\Lambda << 1 < \Lambda_{right} < \Lambda >> 1 .$$

Cosmological problems

A period of chaotic exponential expansion is not required in order for the main cosmological problems to be solved. Alternative solutions are presented in the present section. I argue the apparent flatness of the spacetime geometry, at least on the scales we observe, should not be considered a problem but rather a consequence. The metric of the Universe depends chiefly on two parameters, ρ and H. A stable closed model, however, can be constructed. A non-singular patch with extremely low degree of initial anisotropy in low entropy state, going through a non-exponential expansion phase, can result in an apparent flatness. The 4D spacetime within the Bubble Universe we live in might appear flat on smaller scales. Although one can set local coordinates that exhibit Minkowski metric, they do not represent the complete manifold. It is possible, however, for the Universe to exhibit flat geometry on fairly large scales ($>H^{-1}$). Based on the requirements for expansion to be initiated, the flatness of the spacetime, observed today, is simply a natural consequence of the initial conditions.

Let us now consider the horizon problem. A non-inflationary solution, which was inspired by some string theory models, is proposed. Let us suppose the existence of a tachyon field in the low entropy state of the Universe. The tachyon field coupled to 4D gravity has a non-canonical action, which can be written as

(17) $$S_T = -\int d^4 x\sqrt{-g}\left[V(T)\sqrt{1+\partial_\mu T\partial^\mu T}\right],$$

where $V(T)$ is the positive effective potential of the field with maximum value at $\phi = 0$ and g is the coupling constant. The Lagrangian of the scalar field in curved spacetime is written as

(18) $$\mathcal{L}(x) = \frac{1}{2}[-g(x)]^\wedge 1/2\left[g^{\mu\nu}(x)\partial_\mu\phi(x)\partial_\nu\phi(x) - [m^2 + \varepsilon R(x)]\phi^2(x)\right],$$

where m is the mass of the field, R is the Ricci scalar and ε is the coupling constant. The tachyon field is in a state of unstable equilibrium at the top of its potential energy $V(\phi)$. Due to quantum fluctuations the field is taken out of its present state, consequently, it rapidly decays, converting all of its effective potential into *metastable* spin-0 electrically neutral particles, *tachyons*, which obey the following energy-momentum relation $E^2 = p^2 + m^2$, where $c = 1$. Because the tachyons are metastable, they dilute before their energy reaches zero, as this would imply infinite propagation velocity, $v_T \rightarrow \infty$ as $E \rightarrow 0$. As the field rolls down, it relaxes to a stable configuration, corresponding to the minimum of its potential. Once the field is settled, no more particles are produced. The particles propagate superluminally for an extremely brief period of time. When the tachyons dilute, they release the remaining of their energy. Therefore they can even the temperature of the universe and produce the near-isotropy of the cosmic microwave background (CMB) radiation. The apparent lack of monopoles in the Universe today is one of the central puzzles in modern cosmology. We do, however, strongly believe in their existence. Contemporary particle models, like Grand Unified Theories (GUTs) and Superstring Theory predict the existence of magnetic monopoles. Furthermore, experiments for artificially creating monopoles bolster our view even more [19]. Most of the GUTs suggest that when the temperature of the early Universe dropped below the GUT threshold $T < T_{GUT}$, the Universe went through a phase transition, associated with spontaneous symmetry breaking, and hence the creation of topological defects, like domain walls, cosmic strings, and magnetic monopoles, for example. The rest energy of the magnetic monopoles at the time of the GUT phase transition, based on most particle models, is estimated to be $m_M c^2 = 10^{12}\, TeV$, which yields an approximate energy density of $\rho_M \sim 10^{94}\, TeV\, m^{-3}$. The same, string-theory-borrowed mechanism, used to resolve the horizon problem, is applied. We emphasize here on the inversed proportionality between the energy of the particles and their velocity. As we have explained, when the field decays, it produces tachyon condensate. The condensate is highly energetic at first, and then its energy E_T exponentially decreases as the velocity v_T increases, in accordance the following relation $E_T = \frac{1}{v_T}$. As a result, a fraction of the magnetic monopoles is annihilated.

Discussions and Conclusions

In the present section, I will first discuss the apparent contradiction between quantum mechanics and general relativity by conducting a simple *gedanken* experiment. I will then present an early-Universe phenomena which reinterprets the nature of the spacetime. The scenario occurs naturally as we approach Planck energy scale and addresses the cosmological principle which we have been taken for granted. The phenomena show the crucial role quantum mechanics plays in the early history of the Universe. A lot of work towards unifying quantum mechanics and relativity has been done in the past. However, developing a comprehensive theory of quantum gravity has proven to be extremely difficult. The conclusions, which I draw, are based on a *gedanken* experiment which I will now put forward. For the purposes of the current experiment I will consider the fundamental building blocks of nature to be tiny constructor pieces which behave quantum mechanically. Imagine Charlie starts playing with the constructor pieces by adding the individual blocks together. We assume he has created a bigger structure. Although the new construction is somewhat bigger, suppose it still behaves probabilistically. If he keeps playing though, a point will be reached, at which the whole system (consisting of N number of pieces), will start exhibiting deterministic properties. However, consider Charlie decides to take a piece away from his toy, so that the new structure now consists of $N-1$ pieces. As a result, we assume his actions would bring back the random nature of the system. The difference in the behavior between the *N number* configuration and the *N-1 number* configuration is believed to be discrete. Following the *gedanken* experiment described above, we narrow it down to two possibilities. The first possibility relies on the well-bounded difference between the intuitive laws in the macroscopic world and the seemingly chaotic laws in the quantum realm. That is why it is plausible to assume that at particular scale a *transition* between quantum mechanics and general relativity occurs. Building on that, it is then feasible for us to speculate that every $N\text{-}particle$ quantum system will change its nature to general relativistic one in the $N+1-particle$ case when the transition point, corresponding to a certain number of particles, is passed. However, it is still unknown at what scale exactly does the transition between stochastic and deterministic behavior occur. The second interpretation of the *gedanken* experiment includes the naive conclusion that since the fundamental building blocks of nature act quantum mechanically, then the large-scale structures they make should act in the same manner. In this case the reason why we tend to experience our macro world as deterministic could be attributed to our ability to perceive the physical reality. It should be noted that I have covered the second possibility despite my skepticism towards it.

Based on the provided interpretations of the thought experiment, I argue *general relativity is nothing more than a macroscopic manifestation of quantum mechanics*. A contradiction is present because we are trying to unify a manifestation of a theory with the theory itself. The homogeneity and isotropy of the Universe on large scales (> 100 Mpc) is formulated as the cosmological principle. A satisfactory explanation about which has not yet been provided, and the very notion has been so far taken for granted. As we go backwards in time both the temperature and the density of the Universe increase. If we go as far back as $10^{-36}s$ the temperature of the Universe is approximately$10^{28}\ K$, corresponding to energy levels of $10^{12}\,TeV$. At that energy scale the electromagnetic, weak and strong forces unify in GUT. We expect if we go even further back in time to $10^{-43}s$ the temperature of the universe to be $10^{33}K$, corresponding to Planck energy, E_p~$10^{16}\ TeV$. This is believed to be the so-called Theory of Everything scale, at which gravity unifies with the other gauge forces. I claim *quantum* *mechanics acts differently* in a certain way when $T >> T_{GUT}$. Therefore, I argue the *monogamy of entanglement is violated* at Planck energy scale and what I call “global entanglement” or “polygamy of entanglement” is present. The notion of global entanglement in the very early Universe can naturally explain the cosmological principle we observe today. In that sense, objects separated by distance greater than the Hubble radii never lose causal contact, as one might expect. On a deeper quantum mechanical level, the different regions of the Universe are always in causal contact, regardless of the physical distance. Because of the fundamental implications of quantum mechanics, it is plausible for us to assume the polygamy of entanglement played an essential role in the early history of the Universe. Recent developments in theoretical physics opened the possibility for a different approach to the nature of the spacetime. Work by Mark Raamsdonk [20] and others point out that we might have to reconsider our understanding of the spacetime. A proposal was made that the classical spacetime geometry emerges from quantum entanglement. In a sense, quantum entanglement holds space together and the structure of the spacetime is combinatorial rather than continues. The contemporary, and somewhat radical views, fit elegantly with the idea of polygamy of entanglement at Planck energy scale. In this picture the “spooky action at a distance” becomes a feature of the combinatorial structure of the Universe. The naïve interpretation would be that in a combinatorial structure, held together by quantum entanglement, any two points in space should be able to communicate instantaneously. We observe this not to be the case. From what we know if two particles have not interacted in the past they should not be able to communicate. The reason points to the ER=EPR relation. As it has been suggested by Susskind and Maldacena [21] any pair of entangled particles should have a tiny wormhole connecting them. The new view regarding the structure of the spacetime strongly advocates this proposal. An integral feature of the combinatorial structure of the spacetime should be namely the possibility for creating tiny wormholes between any pair of entangled particles.

Acknowledgements

I would like to thank Prof. Lachezar Filipov, Head of Astrophysics Department at Space Research and Technology Institute, the Bulgarian Academy of Sciences, for the productive discussions.

References

1. Guth, A. H. Inflationary universe: A possible solution to the horizon and flatness problems, Phys.Rev. **D23**, 347, 1981.
2. Linde, A. “Inflationary Cosmology”, arXiv:0705.0164v2 [hep-th].
3. Tsujikawa, S. “Introductory review of cosmic inflation”, arXiv:hep-ph/0304257v1
4. Liddle, A. R. “An introduction to cosmological inflation”, arXiv:astro-ph/9901124v1

5. Planck Collaboration, 2013.
6. Ijjas, A., P. J. Steinhardt, A. Loeb, “Inflationary paradigm in trouble after Planck2013”, arXiv:1304.2785v2 [astro-ph.CO].
7. Guth, A. H. Inflationary universe: A possible solution to the horizon and flatness problems, Phys.Rev. **D23**, 347, 1981.
8. Linde, A. D. A new inflationary universe scenario: A possible solution of the horizon, flatness, homogeneity, isotropy and primordial monopole problems, Phys.Lett. **B108**, 389, 1982.
9. Albrecht, A. and P. J. Steinhardt, Cosmology for Grand Unified Theories with Radiatively Induced Symmetry Breaking, Phys.Rev.Lett. **48**, 1220, 1982.
10. Takeuchi, H., M. Tsubota, G. E. Volovik, “Zel'dovich-Starobinsky Effect in Atomic Bose-Einstein Condensates: Analogy to Kerr Black Hole”, arXiv:0710.2178v1 [cond-mat.other].
11. Volovik, G.E. “Superfluid 3He, Particle Physics and Cosmology”, arXiv:cond-mat/9711031v2
12. Volovik, G.E. “Superfluid analogies of cosmological phenomena”, arXiv:gr-qc/0005091v3
13. Jacobson, T. A. G.E. Volovik, “Event horizons and ergoregions in 3He”, arXiv:cond-mat/9801308v4
14. Volovik, G. E. “Horizons and Ergoregions in Superfluids”, arXiv:gr-qc/0603093v4
15. Volovik, G. E. “Black-hole horizon and metric singularity at the brane separating two sliding superfluids”, arXiv:gr-qc/0208020v3
16. Hawking, S.W. “Particle creation by black holes”, Phys. 43, 199-220, 1975.
17. Mavromatos**,** N.E. **“**Eluding the No-Hair Conjecture for Black Holes”, arXiv:gr-qc/9606008v1
18. Gürlebeck**,** N. **“**No-hair theorem for Black Holes in Astrophysical Environments”, arXiv:1503.03240v1 [gr-qc].
19. Ray, M.W., E. Ruokokoski, S. Kandel, M. Möttönen, D.S. Hall, "Observation of Dirac Monopoles in a Synthetic Magnetic Field", arXiv:1408.3133 [cond-mat.quant-gas].
20. Raamsdonk, M.V. "Building up spacetime with quantum entanglement", arXiv:1005.3035 [hep-th].
21. Maldacena, J., L. Susskind, "Cool horizons for entangled black holes", arXiv:1306.0533v2 [hep-th].

КОСМОЛОГИЧЕН МОДЕЛ НА МЕХУРНА МУЛТИВСЕЛЕНА

А. Йосифов

Резюме

Поставя се под съмнение конвенционалната сингулярна теория за Големия взрив. Представя се нов модел, който не включва нито първоначална сингулярност $g_{00} = \infty$ при $t = 0$, нито кратък период на експоненциално разширение $a(t) \sim e^{Ht}$. Основните параметри, T и ρ, са с крайни стойности. Предлаганият космологичен модел представя Вселената, като част от мултивселена. Зараждането на нашата Вселена се описва в контекста на квантова теория на полетата в нагънато пространство. Също така се представя алтернативен механизъм не само за решаване на основните фундаментални проблеми в съвременната космология – плоскостта на Вселената, проблемът с хоризонта, както и магнитните монополи, но и за редуциране на техния брой. В конкретния труд се описва фундаменталната структура на пространство-времето, както и привидното несъответствие между квантовата механика и теорията за гравитацията на Айнщайн от гледна точка на класическа теория на полетата в 3+1 измерения.

Bulgarian Academy of Sciences. Space Research and Technology Institute.
Aerospace Research in Bulgaria. 27, 2015, Sofia

ISS RADIATION ENVIRONMENT AS OBSERVED BY LIULIN TYPE-R3DR2 INSTRUMENT IN OCTOBER-NOVEMBER 2014

Tsvetan Dachev*[1]*, Borislav Tomov*[1]*, Yury Matviichuk*[1]*, Plamen Dimitrov*[1]*,
***Nikolay Bankov*[1]*, Donat-Peter Häder*[2]*, Gerda Horneck*[3]*, Günter Reitz*[3]**

[1]*Space Research and Technology Institute – Bulgarian Academy of Sciences*
e-mail: tdachev@bas.bg
[2]*Neue Str. 9, 91096 Möhrendorf, Germany; e-mail: donat@dphaeder.de*
[3]*DLR, Institute of Aerospace Medicine, Köln, Germany*
e-mail: gerda.horneck@dlr.de, Guenther.Reitz@dlr.de

Abstract

Space radiation was monitored using the R3DR2 spectrometer-dosimeter during the flight outside the Russian "Zvezda" module of ISS in October-November 2014. The instrument was mounted on the ESA EXPOSE-R2 platform. The R3DR2 instrument was first developed and used during the flight of ESA EXPOSE-R platform in 2009-2010 (Dachev et al, 2015a). It is a low mass, small dimension automated device that measures solar visible and ultraviolet (UV) radiation in four channels and ionizing radiation in 256 channels of a Liulin-type energy deposition spectrometer (Dachev et al, 2002). Ionizing radiation was measured and separated in 256 deposited energy spectra, which were further used for determination of the absorbed dose rate and flux. The main results obtained by the R3DR2 instrument are: (1) three different radiation sources were detected and quantified - galactic cosmic rays (GCR), energetic protons from the inner radiation belt (IRB) in the region of the South Atlantic anomaly and energetic electrons from the outer radiation belt (ORB); (2) for the first time in the history of using of the Liulin-type energy deposition spectrometers (Dachev et al, 2015b) an observable flux from solar energetic particles (SEP) was detected in the period 1-4 November 2014; (3) the obtained SEP energy deposition spectra were compared with other spectra to confirm their shape.

Introduction

This paper analyses the results for the space radiation environment outside the Russian "Zvezda" module of ISS generated by different radiation sources including: Galactic Cosmic Rays (GCR), Inner Radiation Belt (IRB) trapped protons in the region of the South Atlantic Anomaly (SAA) and Outer Radiation Belt (ORB) relativistic electrons. Low intensity Solar energetic particles (SEP) were observed in the 1-2 November time interval. In addition, there is secondary radiation produced in the shielding materials of the ESA EXPOSE-R2 platform and Russian "Zvezda" module. Dose characteristics in the R3DR2 instrument also depend on many other variables such as the ISS orbit parameters, solar cycle phase and current helio- and geophysical activity. In this study the orbital parameters were calculated by the software KADR-2 (Galperin et al., 1980). More comprehensive information for the ISS radiation environment was published in the recently overview by Dachev et al. (2015b).

Materials and methods

R3DR2 instrument description

In order to determine and quantify the radiation field outside the ISS, in the ESA EXPOSE-E/R platform, a radiation environment spectrometer-dosimeters R3DE/R was developed through collaboration of the Bulgarian and German teams (Streb et al., 2002; Häder and Dachev 2003; Häder et al., 2009). The teams worked successfully during the ESA EXPOSE-E/R missions in 2008-2009 and 2009-2010 time periods, respectively. The currently used R3DR2 spectrometer-dosimeter on the ISS is in fact the same instrument which was flown in 2009-2010 in the EXPOSE-R facility but here it is named with the extension R2 only for purposes to distinguish between the data from the different EXPOSE-R(1) and EXPOSE-R2 missions.

The R3DR2 is a Liulin-type instrument which was successfully flown: 1) In the USA Laboratory module of the ISS in May-August 1991 (Reitz et al., 2005; Dachev et al., 2002; Nealy et al., 2007; Wilson et a.l, 2007; Slaba et al., 2011, Badavi, 2014); 2) Inside ESA Biopan-5/6 facilities on Foton M2/M3 satellites in 2005/2007 (Häder et al., 2009; Damasso et al., 2009); 3) Inside the ESA EXPOSE-E/R facilities outside the Columbus/Zvezda modules of the ISS in 2008-2010 (Dachev et al., 2012a; Dachev et al., 2015a).

The scientific objectives of the RDR2 spectrometer-dosimeter exposure were: first connected with the quantification of the global distribution and time dynamics of the radiation fields, generated by different radiation sources outside the ISS; the second purpose is the dosimetric support for other passive scientific experiments, related to astrobiology (Rabbow et al., 2015), which were housed

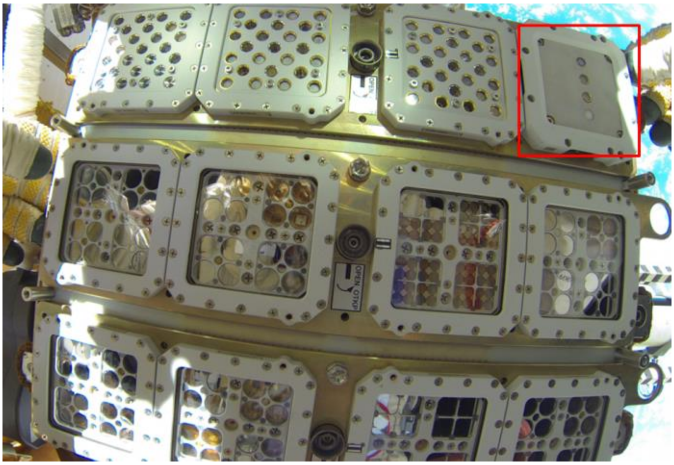

Fig. 1. External view of R3DER instrument (in the red square) as mounted in the EXPOSE-R2 facility. (Picture taken by Russian cosmonaut Aleksandr Samokutyaev on 22 October 2014 during EVA-2 for mounting of EXPOSE-R2 facility outside Russian "Zvezda" module. (Picture credit of ESA/NASA/RKA)

inside the EXPOSE-R2 facility. For all of these experiments the knowledge of the history of solar and ionizing radiation and the total obtained doses is highly important for the interpretation of the data collected during the mission.

Figure 1 presents the external view of the R3DR2 instrument as mounted in the EXPOSE-R2 facility. The R3DR2 instrument is a low mass, small dimension automatic device that measures solar radiation in four channels and ionizing radiation in 256 channels of a Liulin-type energy deposition spectrometer (Dachev et al., 2015b). The four solar UV and visible radiation photodiodes are seen as small circles on the surface in the central part the R3DR instrument. The ionizing radiation detector is located behind the aluminum wall of the instrument and is not seen in the figure. The aluminum box of R3DR instruments has a size of 76×76×34 mm and weight of 120 g.

The cosmic radiation is determined using a semiconductor detector (2 cm^2 area and 0.3 mm thick). A pulse height analysis technique is used to measure the deposited energies (doses) in the detector. Charge pulses generated in the detector are preamplified and then passed to the discriminator. The amplitudes of the pulses are detected and converted into digital signals by a 12 bit analog to digital converter (ADC), which are subsequently sorted into a 256 channels spectrum according to their amplitudes by a multi-channel analyzer (MCA). One energy deposition spectrum is accumulated over 10 s. The 256th energy channel stores all pulses with amplitudes higher than the sensitivity range (19.5 mV–5.0 V) of the detector, which corresponds to the energy deposition range (0.081-20.83 MeV).

The dose D [Gy] by definition is one Joule deposited in 1 kg of matter. We calculate the absorbed dose in the silicon of the detector by dividing the summarized energy deposition in the spectrum in Joules by the mass of the detector in kilograms.

$$D = K\sum_{i=1}^{255} ik_i A_i MD^{-1}, \tag{1}$$

where MD is the mass of the detector in kilograms (kg), k_i is the number of pulses in channel “i”, A_i is the amplitude in Volts (V) of pulses in channel “i”, $i.k_i.A_i$ is the deposited energy (energy loss) in Joules (J) in channel “i” and K is a coefficient. Incoming space radiation sources are characterized using the methods described by Dachev (2009).

Instrument calibrations

The R3DR2 instruments were calibrated in a wide range of radiation fields. First, they were irradiated in gamma and neutron (^{137}Cs, ^{60}Co, AmBe and ^{252}Cf) isotope sources radiation fields and at the CERN-EC high energy reference field (Spurny and Dachev, 2003, Dachev et al., 2002). The absolute values of the dose rates obtained from the spectrometer are in very good agreement with the dose rates calculated using the EGS4 transport code (http://rcwww.kek.jp/research/egs/). The values of the measured doses were found to be within 2.8% of the reference value for the ^{137}Cs source and within 8% of the ^{60}Co source (Spurny and Dachev, 2003). The calibrations showed that the spectrometer had high effectiveness with respect to gamma rays, which allowed monitoring of the natural background radiation. Next, the Liulin type spectrometer was calibrated at the cyclotron at Universite Catholique de Louvain, Louvain-la-Neuve, Belgium (Dachev et al., 2002) and by using proton and heavy ion beams in the National institute for radiological sciences (NIRS) Cyclotron facility and the HIMAC heavy ion synchrotron facility at NIRS, Chiba, Japan (Uchihori at al., 2002, 2008). All calibration results and also the GEANT-4 and PHITS code simulations (Ploc et al., 2011) revealed very good coincidence between the measured and predicted energy deposition spectra and proved the effectiveness of the Liulin spectrometers for the purposes of characterization of the space radiation field (Uchihori at al., 2008). A recent review paper (Dachev et al. 2015b) gives a comprehensive description of the Liulin type spectrometers developed since 1996 and their calibrations and space results.

The DES effectiveness for neutrons depends on their energy, being minimal for neutrons with energy of 0.5 MeV and having a maximum of a few percent for neutrons with energies of 50 MeV. According to the “neutron-induced nuclear counter effect” introduced for the Hamamatsu PIN diodes of type S2744-08 (Zhang et al., 2011). Almost all DESs used the same type PIN diodes, and neutrons could be observed in all channels of the spectrum with a higher probability in the first 14 channels.

The ionizing radiation detector of the R3DR2 instrument was mounted about 3 mm below the 1 mm thick aluminium cover plate. Additionally, there was a technological shielding of 0.2 mm copper and 0.2 mm plastic material, resulting in less than 0.6 g cm^{-2} total shielding. This allows the measurement of direct hits by electrons with energies higher than 1.18 MeV and by protons with energies higher than 27.5 MeV (Berger, 2014).

Data analysis and results

All data presentation

The first month (24 October-25 November 2014) of EXPOSE-R2 active data collection mission took place in the middle phase of the 24th solar cycle after the secondary maximum in 2014 (http://www.swpc.noaa.gov/products/solar-cycle-progression). One relatively small solar energetic proton (SEP) event was measured by the R3DR2 instrument, the maximum of which occurred about 22:00 h UTC on 3 November 2014 in the GOES 15 “Space Environment Monitor (SEM)" (http://goes.gsfc.nasa.gov/text/databook/section05.pdf, 30 MeV channel data). No real enhancement in the GOES 15 proton flux with energies above 100 MeV was observed (ftp://ftp.swpc.noaa.gov/pub/warehouse/2014). The geomagnetic field during the period of the ISS flight was at a moderate level with two “strong” and one “moderate” (http://www.swpc.noaa.gov/noaa-scales-explanation) geomagnetic storms on 4, 10 and 16 November 2014. The global geomagnetic storm index Kp (Bartels et al., 1939) reached three noticeable maxima: The first with a maximum of Kp=6 in the interval 09:00-12:00 UT on 4 November 2014; the second maximum with a Kp=7 in the interval 09:00-12:00 UT on 10 November 2014; a third maximum with a Kp=7 in the interval 09:00-12:00 UT on 16 November 2014 (ftp://ftp.swpc.noaa.gov/pub/warehouse/2014).

Radiation sources selection procedures

The following four expected radiation sources can be detected in the data obtained with the R3DR2 instrument: (i) globally distributed GCR particles and their secondaries; (ii) protons with more than 27.5 MeV energy in the SAA region of the IRB; (iii) relativistic electrons and/or *bremsstrahlung* with energies above 1.18 MeV in the high latitudes of the ISS orbit where the ORB is situated; (iv) solar energetic protons (SEP) in the high latitudes of the ISS orbit.

Historically we developed two similar radiation source data selection procedures. The simplest method to distinguish between the contribution of the IRB protons and the ORB electrons is based on the Heffner formulae (Heffner, 1971; Dachev, 2009), which uses the dose to flux ratio (D/F) or the specific dose (SD). When the SD is less than 1 nGy cm^2 particle^{-1} then the expected predominant type of radiation in a 10-s exposition time are electrons in the ORB. When the SD is greater than 1 nGy cm^2 particle^{-1}, then the predominant source are protons in the IRB. GCR source contributes to both SD ranges. For the “BION-M” No1 satellite data selection (Dachev et al., 2015c) we extend this procedure adding analysis of total magnetic field strength and flux values. The precise differentiation

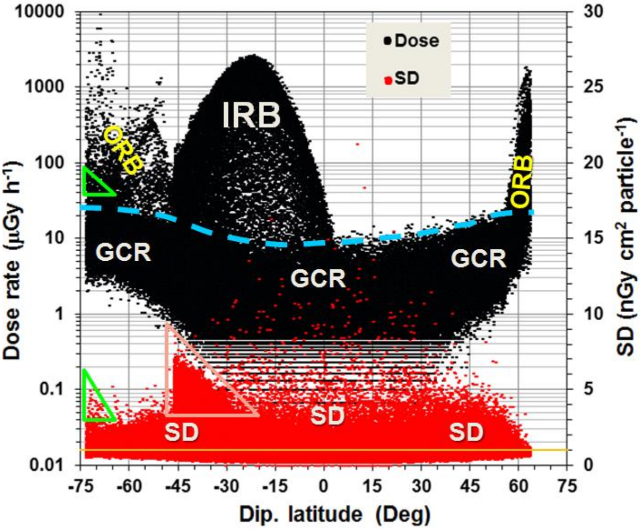

Fig. 2. Presentation of the all R3DR2 data in magnetic dipole coordinates

Table 1. Statistical analysis of the radiation sources obtained with the RDBR2 instrument in the period 23/10-25/11 2014

Source	Number of 10-s meas. [No]/ Duration in days	Hourly av. dose rate min./av./max. [μGy h^{-1}] Daily av. dose rate min./av./max. [μGy d^{-1}]	Obs. dose rate min./max. [μGy h^{-1}] Obs. flux min./max [cm^{-2} s^{-1}]	Total dose rate [mGy] Fluence [No of events/ particles]	Aver. Alt. [km]	Aver. Lat. [Deg.] Aver. L Value	Aver. Long. [Deg.]	Selecting requirem.	
								Dose rate [μGy h^{-1}] Flux [cm^{-2} s^{-1}]	SD [nGy cm^2 $part^{-1}$]/ B [Gauss]/ L
All data	285,418 33.03	Hourly aver.=30.16 Daily aver.=724	0.4/10,506 0.26/4,315	23.913 24,582,180	420	-0.05° 1.83	0.044°	No	No
GCR	249,717 28.9	**R3DR=2.841/3.392/ 3.737** R3DR2=2.969/3.143/ 3.413 **R3DR=68.18/81.4/ 89.69** R3DR2=71.26/75.43 81.91	0.033/29.6 0.34/6.95	2.19 4,078,000	419.5	3.38° 1.8	3.1°	Flux<7	B>0.23
IRB (SAA)	17,018 1.97	**R3DR=239/343/431** R3DR2=322/371/431 **R3DR=326/506/713** R3DR2=518/598/704	20/2,670 0.6/295	19.36 14,141,360	424	-32.4° 1.64	-34.7°	Dose>20	SD>1.12
ORB	5,018 0.58	**R3DR=18/110/1562** R3DR2=20/106/330 **R3DR=0.64/89/2348** R3DR2=0.1/63/235	16/10,506 7/4,315	2.1 5,961,520	425	0.5° 4.33°	0.71°	Flux>7	SD<0.8
SEP	50 0.0058	57.2	40/84.6 2.6/10.8	0.0081 5,440	431	-51° 5.4	116°	D>40 Lat.<0°	SD>1.12 B>0.26

of the CGR source in the dose rate interval of values between 5 and 30 μGy h^{-1} from IRB and ORB source continues to be problematic because even the deposited energy spectra are looking very similar.

For the hourly and daily averaged data of R3DE instrument we developed another similar data selection procedure, described comprehensively in Dachev et al. (2012a). This procedure was used historically for data selection of the R3DR instrument on the EXPOSE-R mission (Dachev et al., 2015a). For the purposes of continuity here we will continue to use, for the hourly and daily averaged data (column 3 of Table 1), the procedure described by Dachev et al. (2012a), while for other average data selections and calculations we use the procedure developed by Dachev et al. (2015c). Both procedures are giving very similar averaged results.

The absorbed dose rates and specific doses obtained by the RDR2 instrument during the whole monitoring period (from 23 October to 25 November 2014) are plotted in Fig. 2. The black points against the left axis in the upper part of the figure correspond to the observed dose rates in μGy h^{-1}. The specific dose (SD) variations calculated from the dose rate to flux ratio in nGy cm^{2} particle^{-1} (Heffner, 1971, Dachev, 2009, Dachev, 2013b) are plotted in red color against the right axis in the lower part of the figure. On the horizontal axis we choose the geomagnetic dipole latitude (Fraser-Smith, 1987), which, similar to the L value (McIlwain, 1961), organizes well the geomagnetic dependent parameters of the space radiation but allows understanding the differences in both geomagnetic hemispheres. The dark yellow line in the bottom of the Fig. 2 shows the position of the SD value equal to 1.

The heavy, light blue, dashed curve in the center of Fig. 2 is drawn for better understanding the contribution of the different radiation sources. The GCR source is distributed below the curve, while the IRB trapped protons source in the region of the SAA and ORB relativistic electrons source are plotted above the curve. Fig. 2 shows the whole dynamics of the observed dose rates over 8 orders of magnitude. The smallest GCR dose rate values of about 0.033 μGy h^{-1} are situated close to the geomagnetic equator, while the largest obtained are in the Southern Hemisphere ORB region where they reach 10,000 μGy h^{-1}.

The large maximum situated in the Southern Hemisphere of Fig. 2 reaching about 2500 μGy h^{-1} were obtained during the ISS crossings of the SAA region where the inner radiation belt, populated with high-energy protons is encountered. The IRB comes at the ISS altitudes due to a displacement of the magnetic dipole axes from the Earth’s center. The maxima in the high latitude regions of both hemispheres are obtained during the crossings of the ORB source. Their poleward boundaries are at different latitudes (65°N in the Northern and 75°S in Southern Hemisphere) because of the asymmetry in the Earth’s magnetic field. The poleward boundaries seen as vertical lines are generated in the dipole latitude coordinate system when the station reaches its maximal magnetic elongation and starts to return back to the magnetic equator.

The analysis of the specific dose variations (lower part of Fig. 2) shows the following: (i) the specific doses corresponding to the points of the GCR source, close to the geomagnetic equator, are distributed in the whole range between 0.187 and 22 nGy cm^2 particle^{-1}. This is explained with the large variations of the dose rates being dependent of the deposited energy from the very low amount of particles; (ii) at higher latitudes the relative deviation of GCR source is smaller with a tendency of all data to be close to 1 nGy cm^2 particle^{-1}; (iii) the data separated in the pink triangle in the Southern Hemisphere correspond to the South-Eastern part of the SAA. The calculated SD values there are relatively large, reaching values of 7−8 nGy cm^2 particle^{-1}. This is explained with relatively low proton energies there, which will be further studied in Fig. 8 of this paper; (iv) the SD data separated in the green triangle in the region above 65°S dipole latitude shows unexpected large SD values between 1 and 5 nGy cm^2 particle^{-1}, which suggests the existence of a source different from ORB, the SD values of which are smaller than 1 nGy cm^2 particle^{-1}. We explain this with the observation of proton fluxes in the SEP in the 1-2 November time period. An analog green triangle is drawn in the dose rate data but because the contamination by ORB dose rates the SEP contribution is not clearly seen.

In Table 1 are summarized the observations for the different radiation sources, presented on Fig. 2, and is provided statistics of the measured values. All b text refers to the R3DR2 data. The limited amount of bold text (in the third column) was obtained during R3DR mission in 2009−2010. Here the R3DR data are presented for comparison with the R3DR2 data. The data in column 3 of Table 1 are selected using the selecting procedure published in (Dachev et al., 2012). The selecting requirements presented in the last 2 columns of Table 1 are valid for the selection of all other columns of Table 1.

The number of measurements, the hourly and daily average, and total accumulated dose rates, and fluences are calculated and presented for all data and for each of the four major sources. The averaged coordinates: longitude, latitude, L value and altitude where the averaged values are obtained, are also presented in 3 columns. The presented values in the “All data” row of the table cover all data collected in the period 23 October − 25 November 2014.

GCR radiation source data were selected using two requirements: (i) The flux values to be less than 7 cm^{-2} s^{-1}, which cuts the high flux level in the ORB (cf. Fig. 2); (ii) The total magnetic field strength to be greater than 0.23 Gauss, which cuts the data obtained inside the SAA region (cf. Fig. 7c) where only the isoline with a total magnetic field strength of 0.23 Gauss is presented with a heavy dashed line). The average daily value was obtained by averaging all observed GCR single measurements for each full day. The data of 31 full days are used.

The IRB (SAA) radiation source data in Table 1 were selected also by two requirements. The first is that the dose rate values have to be higher than 20 μGy h^{-1}. This cuts the GCR dose rates, which usually deposited smaller values.

The second requirement is the SD value has to be higher than 1.12 nGy cm^2 particle^{-1}. According to Heffner's formulae (Heffner, 1971) this selects only depositions by protons excluding relativistic electrons and/or *bremsstrahlung* dose rates higher than 20 μGy h^{-1}. The IRB data covered 31 full days.

The ORB radiation source data in Table 1 were selected by: (i) the flux values to be higher than 7 cm^{-2} s^{-1}, which cuts the low flux level in the GCR; (ii) the SD value to be less than 0.8 nGy cm^2 particle^{-1}. According to Heffner's formulae (Heffner, 1971) this selects only depositions by relativistic electrons and/or *bremsstrahlung* excluding proton depositions from GCR or IRB.

The SEP radiation source data in Table 1 were selected by: (i) only data from 1 and 2 November 2014; (ii) in the Southern Hemisphere because here the ISS reached higher L values; (iii) dose rates to be higher than 40 μGy h^{-1} which excludes any GCR contaminations; (iv) SD values to be higher than 1.12 nGy cm^2 particle^{-1} excluding ORB contamination.

The comparison of the averaged values obtained with the R3DR2 instrument in October−November 2014 with analog R3DR values obtained in the March 2009−August 2010 time interval reveals the following results: (i) the GCR average daily dose rate of 75.43 μGy day^{-1} obtained during the EXPOSE-R2 mission is lower than that measured on the EXPOSE-R mission (Dachev et al., 2015a) of 81.4 μGy d^{-1} because a larger part of the EXPOSE-R mission was performed in the time of lower solar activity and respectively higher GCR flux. The higher EXPOSE-R2 mission orbit of about 420 km in comparison with the 360 km orbit of EXPOSE-R mission does not play an important role because of small GCR altitudinal dependence.

Comparison of R3DR2 L>4 GCR flux data with Oulu NM counts rate data

Our first concern, starting to analyze the R3DR2 GCR data, was how well the data obtained in October−November 2014 follow the tendency of the GCR flux decrease in dependence of the solar activity increase of the 24th cycle. One possible way to answer this question was to compare the GCR “free space” data obtained by the RADOM instrument on the Chandrayaan-1 satellite in 2008 (Dachev et al., 2011a) with the new 2014 R3DR2 GCR data obtained at L values bigger than 4 (McIlwain, 1961; Heynderickx et al., 1996). We choose a L>4 value because the knee in the GCR L-profile is at L=3.5 (Dachev et al., 2012a) and we may expect that all GCR radiation exposure values above L=4 are obtained in the open Earth magnetic field lines, i.e. in conditions very close to the free space. Also these GCR radiation environment data to be compared with the Oulu Neutron Monitor (NM) station count rates (http://cosmicrays.oulu.fi/).

Table 2. Comparison of data obtained by R3DR2 and RADOM instrument with Oulu NM data

RADOM data (GCR, "free space")			**R3DR2 data (GCR, L>4)**			**Oulu NM data**		**Ratio flux R3DR2/ RADOM**	**Ratio dose rate R3DR2/ RADOM**	**Ratio Oulu 2008/ 2014**
Date/ No of meas.	Av. dose rate [μGy h^{-1}]	Av. flux [cm^{-2} s^{-1}]	Date/ No of meas.	Av. dose rate [μGy h^{-1}]	Av. flux [cm^{-2} s^{-1}]	Av. counts 20 Oct.-20 Nov. 2008	Av. counts 23 Oct.-25 Nov. 2014			
04-08 Nov. 2008/ 33,000	12.76	3.14	23 Oct.- 25 Nov. 2014/ 7,438	10.33	2.75	6713	6129	0.876	0.81	0.913

Table 3. Spectra explanation

Spectra name	**Number of primary spectra**	**Av. dose rate (μGy h^{-1})**	**Av. orbit coordinates and selecting requirements**					
			Date	**Lat./Long. (Deg.)**	**Alt. (km)**	**Dose rate (μGy h^{-1})/ Ener. (MeV)**	**L value/ B (Gauss)**	**SD (nGy cm^2 part.$^{-1}$) Flux (cm^{-2} s^{-1})**
GCR; L>4	5687	9.42	23/10- 25/11/2014		430	D<20	L>4	
SEP, 2014	50	54.2	01-02/11/2014	Lat.<0°	431	D>20	L>4	
ORB	5,018	146.1	23/10- 25/11/2014	0.5°/0.71°	425	Flux>7		SD<0.8
IRB	17,018	370.7	23/10- 25/11/2014	-32.4°/- 34.7°	424	D>20		SD>1.12
GCR	249,717	3.16	23/10- 25/11/2014	Lat.<0°	430		B>0.23	Flux<7
GCR; E-E	More than 2,500,000	3.63	03/2008- 09/2009	All/All	365			
IRB; D=45	284	45	23/10- 25/11/2014	-40°/-5°	428	D~45; E~11		
SEP, 2001	66 from MDU-2&3	12.1	20/05/2001				L>5	

In Table 2 is summarized the available information and it is seen that the obtained average flux ratio between R3DR2 and RADOM data in 2014 and 2008 (0.876) coincide relatively well with the Oulu NM count rate ratio (0.913) for similar periods in same years. The dose-rate ratio of 0.81 is not so close to the flux ratio but this can be expected for a stochastic process, which the dose deposition is.

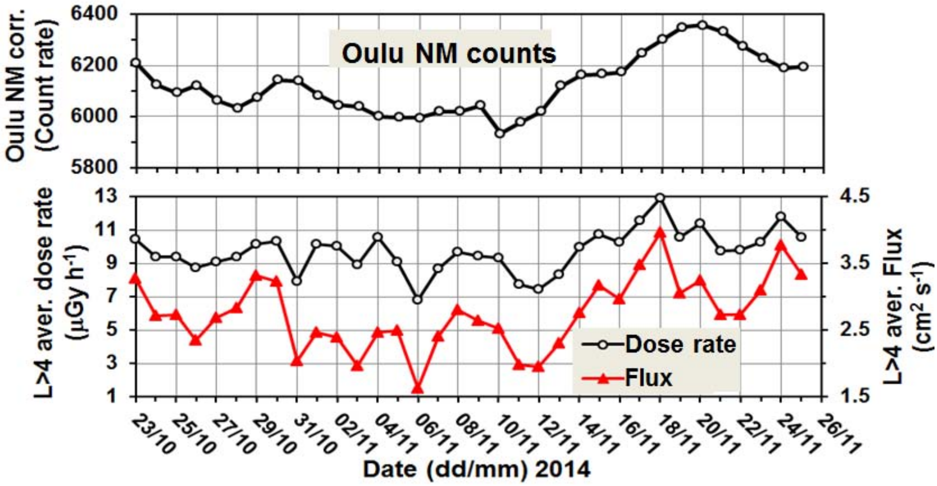

Fig. 3. Comparison between the daily averaged R3DR2 L>4 flux and dose rate data (lower panel) with the Oulu Neutron Monitor (NM) count rates data (upper panel)

On Figure 3 is presented a comparison between the R3DR2 L>4 daily average flux and dose-rate data (lower panel) with the Oulu NM count rates data (upper panel) for the period 23 October−25 November. It could be seen that during the flight of the EXPOSE-R2, in October−November 2014, the averaged flux data per day varied in the interval of 1.5-3.75 cm^{-2} s^{-1}, while the dose rate varied in the interval of 7-13 µGy h^{-1}. The flux and dose rate variations are similar because according to formulae (1) they are in linear dependence. The R3DR2 flux and dose rate curves follow relatively well the Oulu NM curve, which give us the information that the L>4 data obtained by the R3DR2 GCR are representative.

ORB daily variations. Comparison with GOES-15 data and planetary Ap index

Relativistic electrons enhancements (REP) in the outer radiation belt are one of the major manifestations of space weather (Zheng et al., 2006; Wren, 2009; Zhao and Li, 2013) in low Earth orbit (LEO). We keep already long time experience in the REP observations on LEO satellites – Foton M2/M3 and ISS (Dachev et al., 2009, 2012b, 2013a). Our active REP observations in the ISS radiation environment were and are still unique (Dachev et al., 2009).

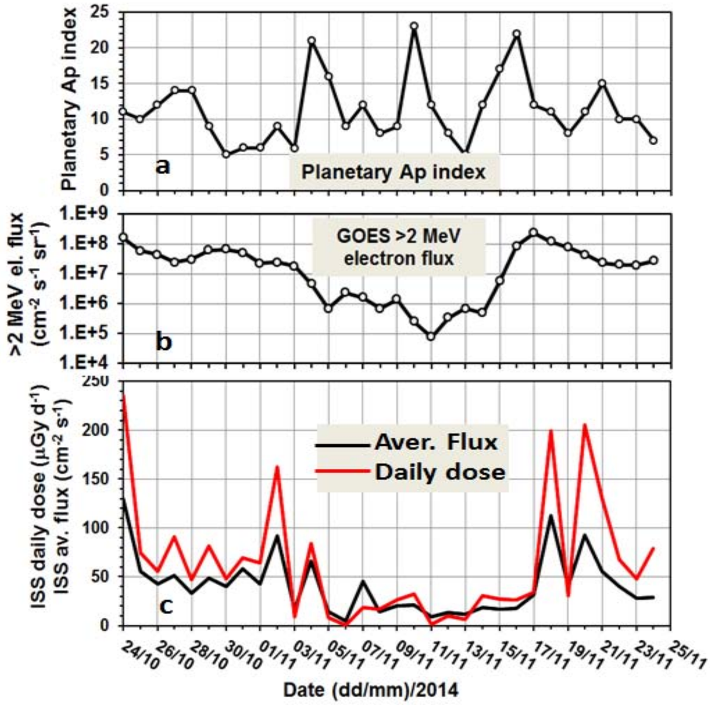

Fig. 4. Daily variations of the ORB dose rates and fluxes (panel "c") observed by R3DR2 instrument. They are compared with GOES-15 >2 MeV electron fluxes in panel "b" and planetary Ap index in panel "a".

The new ISS data in October-November 2014 also contain 5,961,520 counts by relativistic electrons (for more details look at the ORB row in Table 1). In panel "c" of Fig. 4 the daily variations of the ORB relativistic electron dose rates and fluxes observed by R3DR2 instrument are presented. They are compared with GOES-15 >2 MeV electron flux in panel "b" and planetary *Ap* index in panel "a". The *Ap* index is defined as the earliest occurring maximum value for 24 h obtained by computing an eight-point running average of successive three-hour *Ap* indices during a geomagnetic storm event and is uniquely associated with the storm event (http://www.ngdc.noaa.gov/stp/geomag/kp_ap.html). All 3 panels are plotted against the time (date) between 24 October and 24 November 2014.

As it was already noted, the geomagnetic field during the period of the ISS flight in October-November 2014 was at moderate levels with two "strong" and one "moderate" (http://www.swpc.noaa.gov/noaa-scales-explanation) geomagnetic storms on 4, 10 and 16 of November 2014. On Fig. 3 these storms are seen with maxima of the planetary *Ap* index reaching values of 21, 23 and 22 in the central part of panel "a" (ftp://ftp.swpc.noaa.gov/pub/warehouse/2014).

According to our earlier experience with the analysis of the ORB daily variations on the EXPOSE-R mission (Dachev et al., 2015a; see Fig. 6) we expected to observe remarkable enhancements of the ORB daily flux and dose rate after each of the magnetic storm enhancements of the *Ap* index. Unfortunately the first two magnetic storms did not produce any remarkable maxima in both R3DR2 and GOES 15 data. Only the third magnetic storm on 16 November 2014 produced a maxima of the average flux and daily dose rates of >2 MeV electron flux measured by the R3DR2 instrument and GOES-15.

We have to underline that the general trends in the time profiles, obtained on ISS and GOES 15 flux data, match relatively well. The maxima of the relativistic electron flux were observed in the periods 24 October−5 November and 15−24 November, while the minimum was in the period 5−15 November 2014.

The ISS relativistic electron flux maximum on 18 November 2014 in Fig. 4 was delayed by one day in comparison with the >2 MeV flux data from GOES-15 and by two days in comparison with the *Ap* maximum. This is understandable, keeping in mind that there is necessary time for fulfilling of the whole magnetic field line (Zhao and Li, 2013). Our previous experience with the analysis of the R3DR instrument REP data in 2010 (Dachev et al., 2013; see Fig. 5); shows also delay of 2 days between *Ap* maximum on 5 April 2010 and the relativistic electrons flux maximum on 7 April 2010.

The existence of large relativistic electron fluxes in the external radiation environment of the ISS during the October−November 2014 time period, once again confirms our previous findings that this radiation source permanently affects the ISS. That is why it is necessary to keep permanent measurements of the ORB dose rates and especially on the space suit during the ExtraVehicular Activity (EVA) of cosmonauts and astronauts. Under request from our colleagues from Institute of bio-medical problems of the Russian Academy of Science (RAS) we are developing a new Liulin-ISS-2 system (Dachev et al., 2015b), which will perform active measurements on the space suit of the Russian cosmonauts during EVA.

SEP data presentation

Small SEP event was observed in the period 1-7 November 2014. In panel “a” of Fig. 5 are presented the measured proton fluxes by the GOES 15 “Space Environment Monitor (SEM)" with energies >5, >10, and >30 MeV (http://goes.gsfc.nasa.gov/text/databook/section05.pdf). From panel “a” it is seen that the SEP began at about 13:00 UT on 1 November 2014. The maximum in the >30 MeV channel occurred on 3 November 2014 at about 22:00 UTC. The end was on 7 November 2014. No real enhancement in the GOES-15 proton flux with energies >100 MeV was observed (ftp://ftp.swpc.noaa.gov/pub/warehouse/2014).

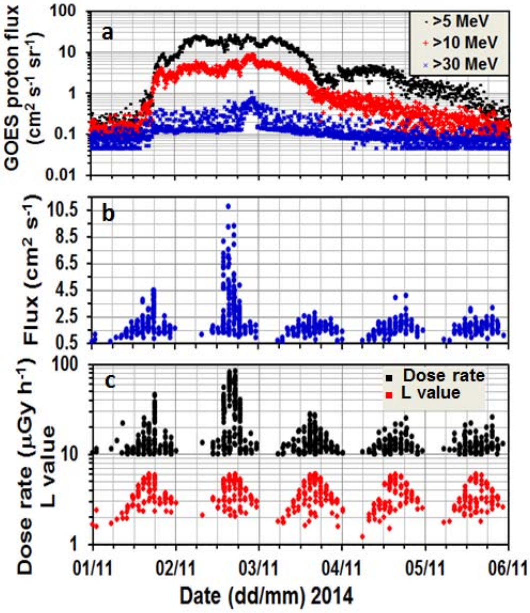

Fig. 5. Presentations of different spectra shapes obtained by the R3DR2 instrument in October–November 2014. (Table 2 presents detailed information for the different curves.)

On Fig. 5 panels "b" and "c" show the dose rates and fluxes measured by the R3DR2 instrument for the same period as the GOES-15 data. In panel "c" except the dose rate in the lower part is presented the L value at which the measurements was made. Data for the panels "b" and "c" were separated under the requirements presented in the last row of Table 1 but dose rates to be more than 10 μGy h^{-1}. We choose this higher dose rate just to show the dynamics of the variations, keeping in mind that only the data with dose rates D>40 μGy h^{-1} undoubtedly belong to the SEP data.

Panels "b" and "c" of Fig. 5 represent the maxima generated when the ISS crosses the Southern Hemisphere from small L values across the maximum of about 6 and back to smaller L values. The main amount of data <20 μGy h^{-1} belongs to the GCR source. The data in the interval 20–40 μGy h^{-1} contains mixed radiation by GCR, ORB, and SPE sources. The SEP data with dose rates D>40 μGy h^{-1} continue to be contaminated by ORB data and this is clearly seen in Fig. 6. We do not have an available procedure to separate them mainly because this is the nature of the radiation sources at these latitudes.

Analysis of the different spectra shapes of the radiation sources

On Fig. 6 are depicted different shapes of the energy deposited spectra obtained mainly by the R3DR2 instrument in October–November 2014. Only the spectra named "SEP, 2001"and "GCR; E-E" were obtained during the DOSMAP and EXPOSE-E missions in 2001 and 2008-2009, respectively. The “SEP 2001” spectrum is presented to show that in the case of very low dose rates (12.1 μGy h^{-1}) the SEP spectrum shape is similar to the “GCR; L>4” spectrum form.

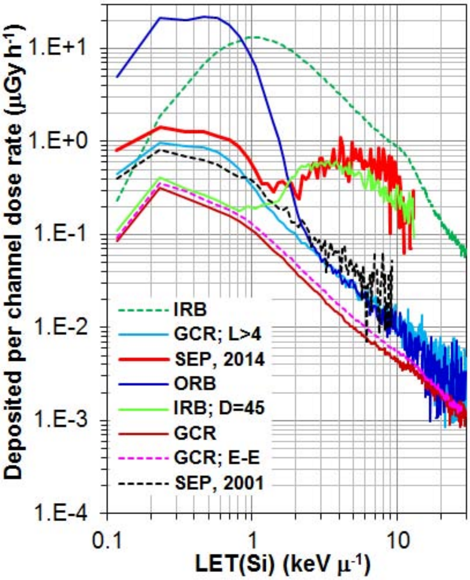

Fig. 6. Presentation of different spectra shapes obtained by the R3DR2 instrument in October–November 2014. (See Table 2 for more detailed information.)

The “GCR; E-E” spectrum is presented to confirm that the EXPOSE-R2 “GCR” spectrum has the same form but lies below the “GCR; E-E” because the solar activity in 2014 was larger than in 2008–2009 and respectively the GCR flux is smaller.

Table 3 contains detailed information for the different spectra in Fig. 6. The individual spectra seen in Fig. 6 are obtained after averaging of various numbers of primary spectra (see column 2 of Table 3.) and are plotted in coordinates of Linear Energy Transfer (LET) in silicon (Si) (keV), per micron/deposited per channel dose rate. This allows a better understanding of the process of formation of the spectra and estimation of the deposited dose rates in the different deposited energy ranges (Dachev, 2009). The deposited dose rate, according to formulae (1), is the area between the abscissa and the curve of the deposited energy spectrum. The “GCR”, “IRB”, and “ORB” spectra are shown in Fig. 6 only to confirm the spectra shapes described by Dachev (2009) that is why we will not further analyze them.

According to our current understanding the “GCR” and “GCR; E-E” spectra averaged over all latitudes are with quasy-linear falling shape in the coordinates deposited energy/deposited per channel dose rate. A more detailed look on the shape shows 2 maxima. The first one is at about 0.9−1 keV μ^{-1}, while the second one is at about 11−12 keV μ^{-1}. This form of the spectra can be interpreted as superposition of 3 single maxima generated by H, He and heavier ions (Ca and O) (Dachev et al., 2013c; Zeitlin, 2014).

Most-interesting and new for us is the spectrum seen in the middle of the figure (Fig. 6) named "SEP; 2014". To explain the different parts of "SEP; 2014" spectrum we add 2 well known and expected spectra. First one is named "GCR; L>4". Its shape in the range 0.1−1.5 keV μ^{-1} deposited energy is similar to the shape of the spectrum named "ORB" and this is reasonable because: (i) the nature of the radiation at these latitudes; (ii) problems, which we have, with the precise differentiation of the GCR and ORB sources in low dose range 5−30 μ□Gy h^{-1}. Further the shape of the "GCR, L>4" spectrum is similar to the two "GCR" and "GCR; E-E" spectra but elevated on the abscissa because of higher dose rates observed at higher latitudes, where the lower geomagnetic vertical cutoff rigidity (Shea and Smart, 2001) allows penetrating in the Earth magnetic field higher primary GCR fluxes. Secondly, an additional spectrum, which is the specially selected "IRB; D=45" spectrum with deposited dose rate and mean energy close to the "SEP; 2014" dose and energy (see Table 3). The low energy deposition part of this spectrum is similar to the "GCR" and "GCR; E-E" spectra, while the high energy part is similar to the "IRB" spectrum, which is generated mainly by protons.

The shape of the "SEP; 2014" spectrum is reasonable because: (i) the low energy deposition part of it is similar to the "GCR; L>4" spectrum because at these deposited energies a mixed radiation of GCR and ORB particles is observed. Also the "SEP; 2014" spectrum is collected at the same high latitudes as the "GCR; L>4" spectrum; (ii) the high energy deposition part of this spectrum is similar to the "IRB; D=45" spectrum, which present low energy protons in the South-East part of the SAA.

Global distributions of the dose rate and flux data

Figures 7b and 7c present the averaged contour view of the R3DR2 flux and dose rate global distribution obtained outside the ISS in the period 23−30 October 2014 with 10-s resolutions. In Figure 7a they are compared with the predicted proton fluxes above 100 MeV and electron fluxes above 4 MeV at an altitude of 420 km by the AP/AE-8 MAX models (http://www.spenvis.oma.be/); Vette, 1991).

In Figure 7b, except the world map of the flux, the isolines of the L value (McIlwain, 1961; Heynderickx et al., 1996) for the 2015 epoch at the altitude of the ISS are also presented with dashed magenta lines for L values 1.7 and 2.1. The L=4 isoline is presented with a heavy line. It is seen that the lines of equal fluxes in the north and south high latitude regions follow well the L-shell isolines as expected.

In Figure 7c, except the global map of the dose rate, the isoline of 0.23 Gauss of the total Earth magnetic field strength B for the 2015 epoch at the altitude of the ISS are also presented with a dashed black line. It is seen that this line separates well the area of the SAA, populated with IRB protons with energies between 30−500 MeV from the GCR region around it.

On Figure 7b and 7c the areas outside the SAA region present the averaged GCR flux and dose rate distribution, forming a wide minimum close to the magnetic equator and rise toward the higher latitudes in both hemispheres.

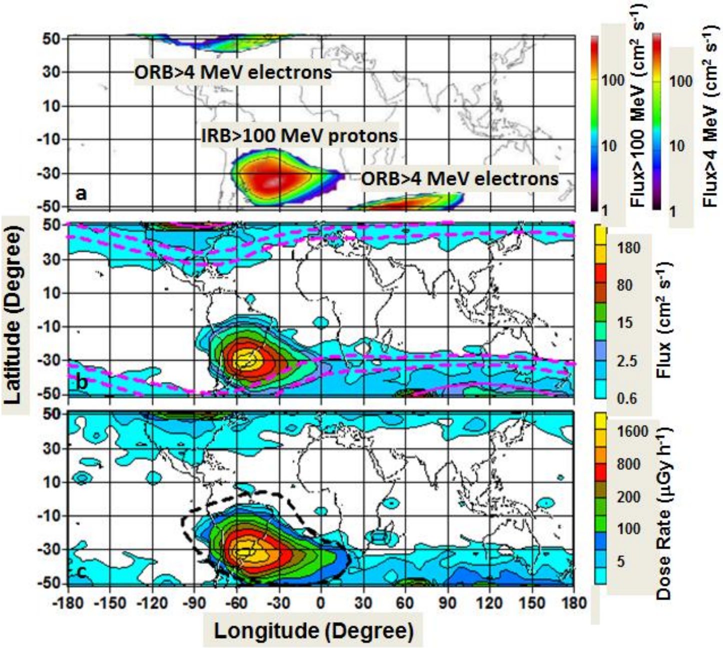

Fig. 7. Figures 7b and 7c present the global distribution of the R3DR2 flux and dose rate data for the period 23−30 October 2014, which are compared with the predicted ones by the AP-8/AE-8 MAX models proton fluxes above 100 MeV and electron fluxes above 5 MeV in Figure 3a.

The observed flux maximum at L=4.4 shows the position and shape of the ORB maximum, which is distributed wider in longitude than the AE8 MAX predictions. The absolute maxima of the R3DR2 ORB data are at latitudes above 45° in both hemispheres. Their coordinates in longitude are 70 °E in the Southern Hemisphere and 80 °W in the Northern Hemisphere. These coordinates coincide well with the AE8 MAX predictions. The comparison of the averaged flux values inside the ORB maxima shows that the predicted model values are in the range 150−300 cm^{-2} s^{-1}, while the measured ones are 140 cm^{-2} s^{-1} in the Southern Hemisphere and 193 cm^{-2} s^{-1} in the Northern Hemisphere.

Recent electron flux data in the 0.5−0.6 MeV and 0.8−1.0 MeV energy range, measured by the energetic particle telescope (EPT) from 29 May 2013 to 20 August 2013 onboard the PROBA-V spacecraft (Cyamukungu et al., 2014; Pierrard et al., 2014) shows well seen global maxima in both hemispheres with a tendency that the Sothern Hemisphere maximum is separated at two parts for the higher energy. The position of the largest electron flux in the 0.8−1.0 MeV energy range of EPT data coincide well with the absolute R3DR2 maximum with coordinates 45°E−80°E, 47°S−50°S (http://space-env.esa.int/index.php/esa-estec-space-environment-tec-ees/articles/EPT_first_results.html). The ORB maximum observed by EPT in the high Northern latitudes also coincides well with our data.

The external oval of the SAA R3DR2 data in Fig. 7b and the one predicted by the AP-8 MAX model in Fig. 7a are very similar and this verifies well our data. We average the coordinates of 373 measurements of the absorbed dose with values more than 2000 μGy h^{-1} and obtain that the R3DR2 SAA maximum is situated at (50.5°W, 31.2°S) at an average altitude of 421 km. 547 measurements of the more than 200 cm^{-2} s^{-1} flux rate gives the average SAA maximum flux coordinates at (51.9°W, 30.0°S). The SAA maximum occurs mainly at the ascending orbits. Only 17 dose rate points of 373 were found at descending orbits. This is in accordance with our previous findings (Dachev et al., 2011b). The explanation is that the R3DR2 instrument is mounted on the left-hand side of *Zvezda* module, against the ISS vector velocity is situated to receive larger amounts of westward drifting protons in the maximum of the SAA on the ascending orbits when the ISS is in the usual XVV attitude (http://spaceflight.nasa.gov/station/flash/iss_attitude.html).

The geographic coordinates of the SAA maximum are influenced by the secular drift of the geomagnetic field (Fraser-Smith, 1987), which leads to a movement of the SAA maximum in the North-West direction. The calculated yearly rate of the SAA flux maximum westward secular drift (Wilson et al., 2006) is 0.3° per year, that is why the calculated 2014 position is 44 (years)*0.3°=13.2° than the calculated SAA flux maximum position is at 48.2°W, which is by 3.7° less than measured with the R3DR2 flux maximum position. The drift rate calculated by us is 0.384° per year, which is in good agreement of the average value of 0.45° per year obtained for the minimum of the solar activity (Qin at al., 2014).

The EPT (Cyamukungu et al., 2014; Pierrard et al., 2014) SAA 90-126 MeV maximum at 820 km altitude can be visually estimated to be at coordinates (55°W, 25°S), which is even more westward than our result. The smaller southward latitude of the SAA maximum in PROBA-V spacecraft data is reasonable because these data are obtained at altitudes around 800 km (Ginet et al., 2008). Qin at al., (2014) also reported that the longitudinal position of the SAA maximum was at 53°W in 2010 for >16 MeV proton flux data obtained with an upgraded version of the Space Environment Monitor (SEM 2) (Evans and Greer, 2000) at 800 km altitude by the NOAA-15 satellite.

Global distributions of the specific dose (SD) data

Figure 8b presents the global distribution of the SD data, which was previously shown in the pink triangle in Fig. 2. The black heavy dashed line presents the isoline of 0.23 Gauss of the total Earth magnetic field strength, which separates the SAA region. It is seen that the calculated SD values in the North-West part of the SAA have values of 1.12 to 2 nGy cm^2 particle^{-1}, which according to the Heffner’s formula (Heffner, 1971; Dachev, 2009) correspond to proton energy in the range of 200−47 MeV. In the South-East part of the SAA region a well-defined maximum is formed. The average SD value in the maximum is 4.8 nGy cm^2 particle^{-1}, which correspond to proton energy at the detector of 13.8 MeV. We suppose that the R3DR2 maximum in SD is formed because of a local maximum in the low energy proton flux, that is why we try to find a confirmation of this idea, preparing Fig. 8a, which presents the proton fluxes above 1.0 MeV energy predicted by AP8 MAX (http://www.spenvis.oma.be/); (Vette, 1991). In contrast to the usual higher energies SAA maximum, two separated maxima are seen: (i) at 5° eastward from the regular position of the SAA and (ii) in the South-Eastern part of it, which extends in the range 0°E−30°E longitude. The form of the AP8 MAX maximum is similar to the form of the R3DR2 maximum in SD, but it is about 30° more towards East than the position of the maximum in Fig. 8b.

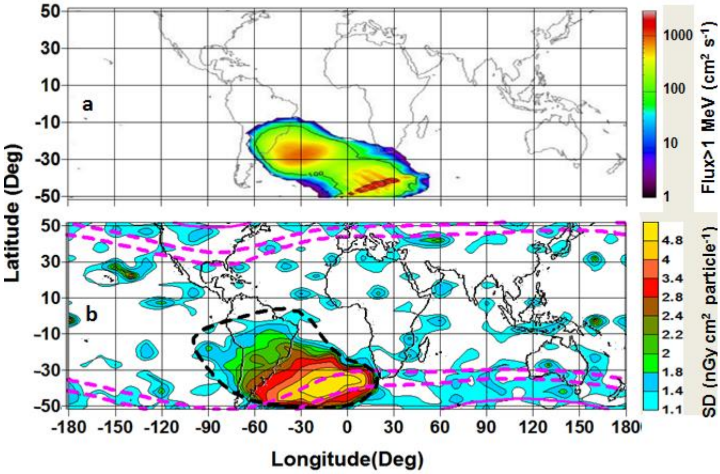

Fig. 8b presents the global distribution of the R3DR2 dose rate to the flux ratio or the specific dose. Data are compared with the world map of the 1 MeV energy proton flux predicted by the AP8 MAX model at 420 km altitude in Fig. 8a.

The centrum of the AP8 MAX 1 MeV maximum in the South-East part of the SAA region in 1970 can be estimated at (15°E, 43°S). The calculated yearly rate of the SAA maximum westward drift is 0.3° per year (Wilson et al., 2006).

Then the calculated position for 2014 in longitude is 44 (years)*0.3°=13.2°. In total, this is giving 15°-13.2°=1.8°, which is about 18° less than necessary to coincide with the R3DR2 maximum in SD. The reported by cellular westward drift rate is dependent by the solar activity (Qin at al., 2014).

On the other hand the geographic distribution of the protons with energies 1−5 MeV measured by the Coronas-F satellite in 2001 show the second maximum at coordinates (6°E, 48°S), which is much closer to the center of the SD maximum in Fig. 8b at (13°W, 38°S) (Kuznetsov et al., 2008; 2010).

On Fig. 9 are presented the longitudinal profiles of the flux, SD and proton energy at the surface of the detector R3DR2 for the latitude range between 35°S and 30°S. To avoid bifurcation of the data only the ascending orbits data are presented. The two trendlines of SD and energy are calculated for six orders polynoms. They are shown only with an illustrative purpose; that is why we do not present the formulas of the polynoms.

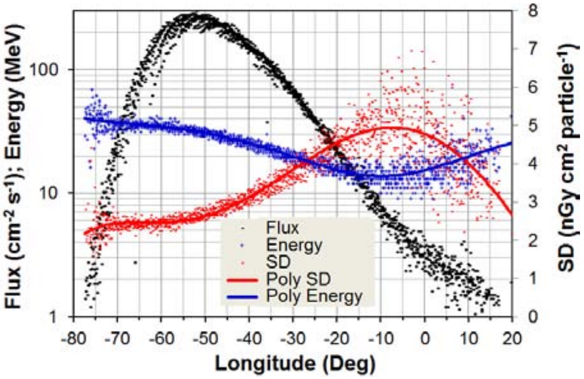

Fig. 9. Longitudinal profiles of the flux, SD, and proton energy for the latitude range between 35°S and 30°S.

It is seen that the absolute flux maximum is at about 52°W longitude where the position of the SAA maximum is. A secondary not very well formed proton flux maximum is seen in the longitude range of about 10°W−10°E. In the same range the maximum of SD is formed and the minimum of the calculated proton energy, respectively.

The proton energy at the surface of the detector is calculated from the SD value using the Heffner formula (Heffner, 1971; Dachev, 2009). The average SD value for the whole Fig. 9 of 3.6 nGy cm^2 particle^{-1} corresponds to 24 MeV protons energy at the surface of the detector. The smallest value of SD of 1.57 nGy cm^2 particle^{-1} corresponds to protons with energy of 69 MeV. The largest SD value, seen in Fig. 9 of 7 nGy cm^2 particle^{-1} corresponds to 9 MeV protons energy at the surface of the detector.

Conclusions

This article analyses the results for the ISS radiation environment obtained by the R3DR2 instrument inside the EXPOSE-R2 facility, generated by different radiation sources, including: galactic cosmic rays (GCRs), inner radiation belt (IRB) trapped protons in the region of the South Atlantic Anomaly (SAA), outer radiation belt (ORB) relativistic electrons, and Solar Energetic Protons (SEP). The first month (24 October–25 November 2014) of the EXPOSE-R2 active data collection mission is covered.

The comparison of the values obtained with the R3DR2 instrument in October–November 2014 with analog R3DR values in the period of 2009–2010 reveal the following results: (i) the GCR average daily dose rate obtained during the EXPOSE-R2 mission is lower than that measured one on the EXPOSE-R mission (Dachev et al., 2015c) because a larger part of the EXPOSE-R mission was performed in the time of lower solar activity and higher GCR flux, respectively; (ii) the IRB average daily dose rate of 598 μGy d^{-1} obtained during the EXPOSE-R2 mission is higher than that measured during the EXPOSE-R mission (Dachev et al., 2015c) of 506 μGy d^{-1} because the EXPOSE-R2 mission orbit was about 60 km higher than the EXPOSE-R mission (360 km); (iii) the ORB average daily dose rate of 63 μGy day^{-1} obtained during the EXPOSE-R2 mission is lower than that measured during the EXPOSE-R mission (Dachev et al., 2015c) of 89 μGy d^{-1} because the EXPOSE-R mission took place during the second largest relativistic electrons precipitation (REP) event in GOES history in the period 7 April–7 May 2010 (Dachev et al., 2013a), when the highest observed values of 2,347 mGy d^{-1} occurred in the R3DR data on 7 April 2010.

For the first time in the history of using of the Liulin-type energy deposition spectrometers (Dachev et al., 2015b) a flux from solar energetic particles (SEP) in the period 1–4 November 2014 were detected; (3) the SEP energy deposition spectra were compared with other well-known spectra and confirmed the SEP spectra shape.

The dynamics of the ORB doses measured for the first month of the EXPOSE-R2-mission periods confirm conclusions made by Dachev et al. (2013) that the ORB relativistic electrons are common on the ISS. Although the obtained doses do not pose extreme risks for the astronauts being on EVA, they have to be considered as a permanently present source, which requires additional comprehensive investigations.

Acknowledgements

The authors are grateful to the following colleagues: Martin Schuster and Michael Lebert from the Cell Biology Division, Department of Biology, Friedrich-Alexander-University, Erlangen, Germany for help in the development, building and data interpretation of the R3DR2 instrument.

References

1. Badavi, F.F., 2014. Validation of the New Trapped Environment AE9/AP9/SPM at Low Earth Orbit, Advances in Space Research, 54, 917-928. http://dx.doi.org/10.1016/j.asr.2014.05.010.
2. Bartels, J., Heck, N.H. & Johnston, H.F., 1939. The three-hour range index measuring geomagnetic activity. Geophys. Res., 44, 411-454.
3. Berger, M.J., Coursey, J.S., Zucker, M.A., Chang, J. Stopping-power and range tables for electrons, protons, and helium ions. NIST Standard Reference Database 124, Available online at: http://www.nist.gov/pml/data/star/index.cfm, October, 2013.
4. Berger, T., Hajek, M., Bilsk, P., Körner C., Vanhavere F., Reitz G. 2012, Cosmic radiation exposure of biological test systems during the EXPOSE-E mission, Journal of Astrobilogy, 12(5), 387-392. DOI: 10.1089/ast.2011.0777.
5. Cyamukungu, M., Benck, S., Borisov, S., Gregoire, G., Cabrera, J., Bonnet, J. L., & Nieminen, P., 2014. The Energetic Particle Telescope (EPT) on board PROBA-V: description of a new science-class instrument for particle detection in space. Nuclear Science, IEEE Transactions on, 61(6), 3667-3681.
6. Cucinotta, F.A., Schimmerling, W., Wilson, J.W., Peterson, L.E., Saganti, P.B., and Dicello. J.F., 2004, Uncertainties in estimates of the risks of late effects from space radiation. Adv. Space Res., 34, 1383–1389.
7. Dachev, T.P., Tomov, B., Matviichuk, Yu., Dimitrov, Pl., Lemaire, J., Gregoire, Gh., Cyamukungu, M., Schmitz, H., Fujitaka, K., Uchihori, Y., Kitamura, H., Reitz, G., Beaujean, R., Petrov, V., Shurshakov, V., Benghin, V., Spurny, F., 2002. Calibration results obtained with Liulin-4 type dosimeters. Advances in Space Research 30, 917–925, http://dx.doi.org/10.1016/S0273-1177(02)00411-8 .
8. Dachev, T.P., 2009. Characterization of near Earth radiation environment by Liulin type instruments. Advances in Space Research, 44, 1441–1449, http://dx.doi.org/ 10.1016/j.asr.2009.08.007.
9. Dachev, Ts., Tomov, B.T., Matviichuk, Yu.N., Dimitrov, P.G., Bankov, N.G. 2009. Relativistic electrons high doses at international space station and Foton M2/M3 satellites. Adv. Space Res., 44 1433–1440, http://dx.doi.org/10.1016/ j.asr.2009.09.023.
10. Dachev, T.P., Semkova, J., Tomov, B., Matviichuk, Yu., Dimitrov, Pl., Koleva, R., Malchev, St., Reitz, G., Horneck, G., De Angelis, G., Häder, D.-P., Petrov, V., Shurshakov, V., Benghin, V., Chernykh, I., Drobyshev, S., and Bankov. N.G., 2011a. Space shuttle drops down the SAA doses on ISS. Adv Space Res. 11:2030–2038, http://dx.doi.org/10.1016/j.asr.2011.01.034.
11. Dachev, T., Angelis, G., Semkova, J., Tomov, B., Matviichuk, Yu., Dimitrov, Pl., Bankov, N., Reitz, G., Horneck, G., Häder, D.-P., 2011b. Further analysis of the space shuttle effects on the ISS SAA doses, paper IAC-11,A1,4,2,x9918, IAF Congress, 2011. http://www.iafastro.net/iac/paper/id/9918/summary.lite/
12. Dachev, T.P., Horneck, G., Häder, D.-P., Lebert, M., Richter, P., Schuster, M., Demets, R., 2012a. Time profile of cosmic radiation exposure during the EXPOSE-emission: the R3D instrument. Journal of Astrobiology 12 (5), 403–411, http://eea.spaceflight.esa.int/attachments/spacestations/ID501800a9c26c2.pdf

13. Dachev, T.P., Tomov, B.T., Matviichuk, Yu.N., Dimitrov, Pl.G., Bankov, N.G., Reitz, G., Horneck, G., Häder, D.-P., Lebert, M., Schuster, M., 2012b. Relativistic electron fluxes and dose rate variations during April–May 2010 geomagnetic disturbances in the R3DR data on ISS. Advances in Space Research 50, 282–292, http://dx.doi.org/10.1016/j.asr.2012.03.028.
14. Dachev T.P., 2013a. Analysis of the space radiation doses obtained simultaneously at 2 different locations outside ISS. Adv. Space Res., 52, 1902-1910, http://dx.doi.org/10.1016/j.asr.2013.08.011
15. Dachev, T.P., 2013b. Profile of the ionizing radiation exposure between the Earth surface and free space. Journal of Atmospheric and Solar-Terrestrial Physics, 102, 148–156, http://dx.doi.org/10.1016/j.jastp.2013.05.015.
16. Dachev, T.P., Ploc, O., Sihver, L., 2013c. Estimation of the dominant ion composition in space using the Liulin and PHITS simulations, Workshop on Radiation Measurements on ISS, Budapest, Hungary, 3-5 September 2013. http://wrmiss.org/workshops/eighteenth/Ploc.pdf
17. Dachev, T.P., G. Horneck, G., D.-P. Häder, D.-P., M. Schuster, M., and M. Lebert, 2015a. EXPOSE-R cosmic radiation time profile, Journal of Astrobilogy, 14, 17-25. http://dx.doi.org/10.1017/S1473550414000093.
18. Dachev, T.P., J.V. Semkova, J.V., Tomov, B.T., Matviichuk, Yu.N., Dimitrov, Pl.G., Maltchev, S., Koleva, R., Bankov, N.G., Shurshakov, V.V. Benghin, V.V., Yarmanova, E.N., Ivanova, O.A. Häder, D.-P., Lebert, M., Schuster, M.T. Reitz, G., Horneck, G., Uchihori, Y., Kitamura, H., Ploc, O., Kubancak, J., Nikolaev, I., 2015b. Overview of the Liulin type instruments for space radiation measurement and their scientific results, Life Sciences in Space Research, 4, 92–114, 2015. http://dx.doi.org/10.1016/j.lssr.2015.01.005
19. Dachev, T.P., Tomov, B.T., Matviichuk, Yu.N., Dimitrov, Pl.G., Bankov, N.G., Shurshakov, V.V., Ivanova, O.A., Häder, D.-P., Schuster, M.T., Reitz, G., Horneck, G., 2015c. "BION-M" No1 spacecraft radiation environment as observed by the RD3-B3 radiometer-dosimeter in April-May 2013, Journal of Atmospheric and Solar-Terrestrial Physics. 123, 82-91, 2015. http://dx.doi.org/10.1016/ j.jastp.2014.12.011.
20. Damasso, M., Dachev, Ts., Falzetta, G., Giardi, M.T., Rea, G., Rea, G., Zanini, A., 2009. The radiation environment observed by Liulin-Photo and R3D–B3 spectrum-dosimeters inside and outside Foton-M3 spacecraft. Radiat. Meas. 44 (3), 263–272, http://dx.doi.org/10.1016/j.radmeas.2009.03.007.
21. Evans, D. S., and Greer, M. S., 2000. Polar Orbiting Environmental Satellite Space Environment Monitor-2: Instrument Description and Archive Data, U.S. Dep. of Commer., Natl. Oceanic and Atmos. Admin., Oceanic and Atmos. Res. Lab., Space Environ. Cent., Boulder, Colo.
22. Fraser-Smith, A. C., 1987. Centered and eccentric geomagnetic dipoles and their poles 1600-1985. Rev. Geophys., 25, 1-16.
23. Galperin, Yu.I., Ponamarev, Yu.N., Sinizin, V.M., 1980. Some Algorithms for Calculation of Geophysical Information along the Orbit of Near Earth Satellites. Report No 544. Space Res. Inst., Moscow (in Russian).

24. Ginet, G.P., Madden, D., Dichter, B.K., Brautigam, D.H. Energetic Proton Maps for the South Atlantic Anomaly, AFRL-RV-HA-TR-2008-1060, 2008. http://www.dtic.mil/cgi-bin/GetTRDoc?AD=ADA485155.
25. Heffner, J., Nuclear radiation and safety in space. M, Atomizdat, 115 p., 1971. (in Russian).
26. Heynderickx, D., Lemaire, J., Daly, E. J. 1996, Historical review of the different procedures used to compute the L-Parameter. Rad. Measur. 26, 325-331.
27. Häder, D.-P. and Dachev, T.P., 2003. Measurement of solar and cosmic radiation during spaceflight. Kluwer Press, Surveys in Geophysics, 24, 229-246.
28. Häder, D.-P., Richter, P., Schuster, M., Dachev, Ts., Tomov, B., Dimitrov, P., Matviichuk, Yu., 2009. R3D-B2—Measurement of ionizing and solar radiation in open space in the BIOPAN 5 facility outside the FOTON M2 satellite. Advances in Space Research, 43, 1200–1211, doi: 10.1016/j.asr.2009.01.021.
29. Kuznetsov N.V., Nikolaeva N.I., Panasyuk M.I., Trapped proton fluxes observed by LEO satellites in 23d solar cycle, 2008. WRMISS13Kraków, PolandSeptember8-10, 2008. http://wrmiss.org/workshops/thirteenth/Kuznetsov.pdf
30. Kuznetsov, N. V., Nikolaeva, N. I. and Panasyuk M. I., 2010. Variation of the trapped proton flux in the inner radiation belt of the Earth as a function of solar activity, Cosmic Res., 48(1), 80–85.
31. McIlwain, C. E., 1961. Coordinates for mapping the distribution of magnetically trapped particles. J. Geophys. Res., 66, 3681-3691.
32. Nealy, J.E., Cucinotta, F.A., Wilson, J.W., Badavi, F.F., Zapp, N., Dachev, T., Tomov, B.T., Semones, E., Walker, S.A., Angelis, G.De, Blattnig, S.R., Atwell, W., 2007. Preengineering spaceflight validation of environmental models and the 2005 HZETRN simulation code. Advances in Space Research 40, 1593–1610, doi: 10.1016/j.asr.2006.12.029.
33. Nymmik, R.A., 2007. Improved environment radiation models. Adv. Space Res. 40, 313–320.
34. Pierrard, V., Rosson, G. L., Borremans, K., Lemaire, J., Maes, J., Bonnewijn, S., ... & Nieminen, P., 2014. The Energetic Particle Telescope: First Results. Space Science Reviews, 184(1-4), 87-106.
35. Ploc, O., Spurny, F., Dachev, Ts.P., 2011. Use of energy depositing spectrometer for individual monitoring of aircrew. Radiat. Prot. Dosim.144 (1–4), 611–614. http://dx.doi.org/10.1093/rpd/ncq505.
36. Qin, M., X. Zhang, B. Ni, H. Song, H. Zou, and Y. Sun, 2014. Solar cycle variations of trapped proton flux in the inner radiation belt, J. Geophys. Res. Space Physics, 119, 9658–9669, doi:10.1002/2014JA020300.
37. Rabbow, E., Rettberg, P., Barczyk, S., Bohmeier, M., Parpart, A., Panitz, C., ... & Reitz, G. (2015). The astrobiological mission EXPOSE-R on board of the International Space Station. International Journal of Astrobiology, 14(01), 3-16 doi: 10.1017/S147355041400069X.
38. Reitz, G., Beaujean, R., Benton, E., Burmeister, S., Dachev, T., Deme, S., Luszik-Bhadra, M., Olko, P., 2005. Space radiation measurements on-board ISS-The DOSMAP experiment. Radiation Protection Dosimetry 116 (1–4), 374–379.

39. Slaba, T.C., Blattnig, S.R., Badavi, F.F., Stoffle, N.N., Rutledge, R.D., Lee, K.T., Zapp, E.N., Dachev, T.P., Tomov, B.T., 2011. Statistical validation of HZETRN as a function of vertical cutoff rigidity using ISS measurements. Advances in Space Research 47, 600–610, http://dx.doi.org/10.1016/j.asr.2010.10.021.
40. Spurny, F., Dachev, Ts., 2003. Long-term monitoring of the onboard aircraft expo-sure level with a Si-diode based spectrometer. Adv. Space Res.32 (1), 53–58. http://dx.doi.org/10.1016/S0273-1177(03)90370-X.
41. Spurny, F., 2005. Response of a Si-diode-based device to fast neutrons. Radiat. Meas. 39, 219–223. http://dx.doi.org/10.1016/j.radmeas.2004.05.006.
42. Streb, C., Richter, P., Lebert, M., Dachev, T., Häder, D.-P., 2002. R3D-B, radiation risk radiometer-dosimeter on BIOPAN (Foton) and expose on the International Space Station (ISS). Proceedings of the Second European Workshop on Exo/Astrobiology, Graz, Austria, 16–19 September, (ESA SP-518), 71–74.
43. Uchihori, Y., Kitamura, H., Fujitaka, K., Dachev, T.P., Tomov, B.T., Dimitrov, P.G., Matviichuk, Y., 2002. Analysis of the calibration results obtained with Liulin-4J spectrometer–dosimeter on protons and heavy ions. Radiat. Meas.35, 127–134.
44. Uchihori, Y., H. Kitamura, N. Yasuda, H. Kentaro, K. Yajima, T.P. Dachev, Chapter 7: Liulin-4J portable Silicon Spectrometer, Results of the ICCHIBAN-3 and ICCHIBAN-4, Experiments to Inlercompare the Response of Space Radiation Dosimeters, HIMAC-128, NIRS, Japan, pp 76-88, March, 2008.
45. Vette, J.I., 1991. The NASA/National Space Science Data Center Trapped Radiation Environment Model Program (1964–1991). NSSDC/WDCA-R&S, pp. 91–92.
46. Wilson, J.W., Nealy, J.E., Dachev, T., Tomov, B.T., Cucinotta, F.A., Badavi, F.F., De Angelis, G., Leutke, N., Atwell, W., 2007. Time serial analysis of the induced LEO environment within the ISS 6A. Adv. Space Res.40 (11), 1562–1570. http://dx.doi.org/10.1016/j.asr.2006.12.030.
47. Wren, G.L., 2009. Chronology of 'relativistic' electrons: solar cycles 22 and 23. J. Atmos. Solar-Terr. Phys. 71, 1210–1218.
48. Zhang, L., Mao, R., Zhu, R., 2011. Fast neutron induced nuclear counter effect in Hamamatsu silicon PIN diodes and APDs. IEEE Trans. Nucl. Sci.58 (3), 1249–1256.
49. Zhao, H., and X. Li, 2013, Inward shift of outer radiation belt electrons as a function of Dst index and the influence of the solar wind on electron injections into the slot region, J. Geophys. Res. Space Physics, 118, 756–764, doi:10.1029/2012JA018179.
50. Zheng, Y., Lui, A.T.Y., Li, X., Fok, M.-C., 2006. Characteristics of 2–6 MeV electrons in the slot region and inner radiation belt. J. Geophys. Res. 111, A10204.
51. Zeitlin, C., 2014. Results from the MSL-RAD Experiment on the Curiosity Mars Rover, Nineteenth WRMISS, Krakow, Poland, 9-11 September 2014. http://wrmiss.org/workshops/nineteenth/Zeitlin_MSL-RAD.pdf

РАДИАЦИОННАТА ОБСТАНОВКА НА МЕЖДУНАРОДНАТА КОСМИЧЕСКА СТАНЦИЯ (МКС), КАКТО СЕ НАБЛЮДАВА ОТ ПРИБОРА R3DR2 ПРЕЗ ОКТОМВРИ-НОЕМВРИ 2014

Цв. Дачев, Б. Томов, Ю. Матвийчук, Пл. Димитров,
Н. Банков, Д.-П. Хедер, Г. Хорнек, Г. Райтц

Резюме

Космическата йонизираща радиация е изследвана с помощта на спектрометъра-дозиметъра R3DR2 по време на неговият полет извън руския модул "Звезда" на МКС през октомври-ноември 2014 г. Приборът е монтиран на платформата на ESA EXPOSE-R2. Приборът R3DR2 е разработен и използван за първи път по време на полета на платформата на ESA EXPOSE-R през 2009-2010 г. (Dachev et al., 2015a). Той е автоматизирано устройство с малко тегло и размер, което измерва видимата слънчева и ултравиолетова (UV) радиация в четири канала и йонизиращото лъчение в 256 канала със спектрометър на депозираната енергия от типа „Люлин“ (Dachev et al., 2002). Основните резултати, получени от работата на R3DR2 са:

(1) открити са и са характеризирани количествено три различни източници на радиация - галактически космически лъчи (GCR), енергични протони от вътрешния радиационен пояс- (IRB) в района на Южно-атлантическата аномалия и енергични електрони от външния радиационен пояс (ORB);

(2) за първи път в историята на използването на спектрометри от тепа „Люлин“ (Dachev et al., 2015a) е наблюдаван поток от слънчеви енергийни частици (SEP) в периода 1-4 ноември 2014;

(3) получените спектри на депозираната енергия са сравнени с други спектри и е потвърдена тяхната форма.

Bulgarian Academy of Sciences. Space Research and Technology Institute.
Aerospace Research in Bulgaria. 27, 2015, Sofia

SUBSTORMS OVER APATITY DURING THE PERIOD OF ENHANCED GEOMAGNETIC ACTIVITY 7-17 MARCH 2012

Veneta Guineva[1], Irina Despirak[2], Boris Kozelov[2], Rolf Werner[1]

[1]Space Research and Technology Institute – Bulgarian Academy of Sciences
[2]Polar Geophysical Institute, Apatity, Russia
e-mail: v_guineva@yahoo.com

Abstract

The period 7–17 March 2012 is one of the most geomagnetically active periods during the ascending phase of Solar Cycle 24. Therefore the solar and interplanetary phenomena during this period along with the consequent processes in the magnetosphere and ionosphere were object of study of the scientific society. The whole chain of events was discussed on several scientific conferences. The solar flares, coronal holes, coronal mass ejections, high speed solar wind streams and interplanetary shocks were identified and the resulting response of the magnetosphere and ionosphere was examined. Four strong geomagnetic storms occurred during this period. The substorms generated in this time are the final effect of all these events. Measurements of the Multiscale Aurora Imaging Network (MAIN) in Apatity (Russia) and data of IMAGE magnetometers network have been used to verify the substorms onset and subsequent development. The characteristics of these substorms were studied and they were compared to substorms originated during similar or different conditions.

Introduction

It is known that certain types of solar wind, mainly Interplanetary Coronal Mass Ejections (ICME) and Corotating Ineraction Regions (CIR) (e.g. 1, 2]), generate magnetic storms. During solar maxima, most common are the sporadic flows associated with CME [3]. Near the Earth, they are observed as magnetic clouds (MC) (e.g. [4]). The magnetic clouds (MC) are characterized as regions, where the magnetic field strength is higher than the average, the density is relatively low and the magnetic pressure strongly exceeds the ion thermal pressure; the magnetic field direction changes through the cloud by rotating parallel to a plane, which is highly inclined with respect to the ecliptic [4]. In front of MC, a region of interaction with undisturbed solar wind (Sheath) is known to form, which is characterized by high density, increased pressure and strong Interplanetary Magnetic Field (IMF) variability. CIR is a region of the interaction between high-speed recurrent streams and the adjacent slower streams. Recurrent streams and their CIR are more frequent during solar minima. CIR is defined as a region with magnetic field and plasma compression [5]. It should be noted that there are differences between storms generated by Sheath, MC, and CIR (in intensity, recovery phase duration, etc.) (e.g. [6, 7, 8]). However, there are more complicated storm cases, when the magnetic storms are caused by several sources in the solar wind, coming consecutively one after the other or partly overlapping. Events of strong geomagnetic activity are of special interest because magnetic storms can affect the energetic systems, the spacecrafts, or the ground based systems. That is why coordinated actions of the scientific community are needed to perform and gather observations, to create models of the whole chain of phenomena from the Sun to the Earth in order to make successful predictions of space weather and to prevent failures in the technologic infrastructure caused by strong geomagnetic storms [9]. Storms are the final effect of the enhanced solar and interplanetary activity. Substorms generated during geomagnetic storms are significant features. Therefore, it is important to have more observations of substorms during storms, especially under strongly disturbed conditions.

In this paper, a period of high geomagnetic activity (7–17 March 2012) was examined by ground based aurora observations at Apatity (Russia) and the observed substorms were studied.

Instrumentation and data used

The *Apatity*'s location at auroral latitudes: geographic coordinates (67.58ºN, 33.31ºE) and Corrected GeoMagnetic (CGM) ones (63.86ºN, 112.9ºE) is expedient to examine the variety of substorms.

Measurements from the Multiscale Aurora Imaging Network (MAIN) in *Apatity* (Russia), during the strongly disturbed period 7–17 March 2012, have been used. The all-sky camera observation system has been built in *Apatity* since 2008. The cameras' characteristics, their mutual situation and the measurement process are described in detail by Kozelov et al. [10].

To study the substorm development data from the *Apatity*'s all-sky camera (images and keograms) and the Guppy F-044C (GC) camera, with a field of view ~67° (keograms), were used. The GC camera data were corrected regarding the exposition time, the gain, the heterogeneity of the dark field, and the objective transmittance change depending on the angle of observation. The keograms were constructed in direction magnetic North (up). The zero angle coincides with zenith.

Solar wind and interplanetary magnetic field parameters were taken from OMNI database (http://sdaweb.gsfc.nasa.gov/cdaweb/istp_public). The *Kp* indices were taken from NOAA database: (http://www.ngdc.noaa.gov/stp/GEOMAG/kp_ap.html). Substorm presence was verified by ground-based data of IMAGE magnetometers network (using the meridional chain Tartu (TAR) /CGM latitude=54.47°/ – Ny Ålesund (NAL) /CGM latitude= 75.25°/).

Overview of the interplanetary conditions

The time interval 7–17 March 2012 (11 days) is one of the first major geomagnetically active periods of the ascending phase of SC24 [11]. It was examined and the detected features were described [11, 12]. Magnetic storms occurred on 7, 9, 12, and 15 March, and they were called the S1, S2, S3, and S4 events. These storms were caused by Sheath, MC, and HSS, the detailed scenario for all four storms were different. The storms are classified by the maximal k_p index value. During the four periods of storm activity the k_p index exceeded the limit of the "storm" conditions (k_p=5). During S2 the level of severe storm (k_p=8) was reached, the three other events are at the level of moderate storms (k_p=6). The interplanetary conditions during the examined period and the geomagnetic responses are presented in Fig.1. In all frames, from top to bottom the panels are: the magnitude of the IMF B, the IMF B_z component, the solar wind velocity v, its x component v_x, the proton density, the proton temperature, the flow pressure and two geomagnetic activity indices, AE and SYM/H. On Fig.1a is presented an overview of the interplanetary conditions from 7 to 20 March 2012. The vertical lines point out the beginning of the four events. On Fig.1 *b*, *c*, and *d* are represented the conditions during S1, S2, and S4 in more detail. The continuous vertical lines indicate the interplanetary shocks (S) and the borders of the solar wind streams (for details, see [11]).

Results

The measurements during the time interval 7–17 March 2012 were examined together with the interplanetary conditions during the measuring periods. Ten substorms were identified over *Apatity* under clear sky conditions: 4 of them developed during S1, 3 – during S2, and 3 – during S4. The times of the substorms are marked by dashed vertical lines in Fig. 1*b*, *c*, and *d*. They occurred during different interplanetary conditions and at different stages of the geomagnetic storms development. Two typical cases of substorms were chosen presenting a substorm generated during the recovery phase in the vicinity of the maximal development and a substorm during the late recovery phase.

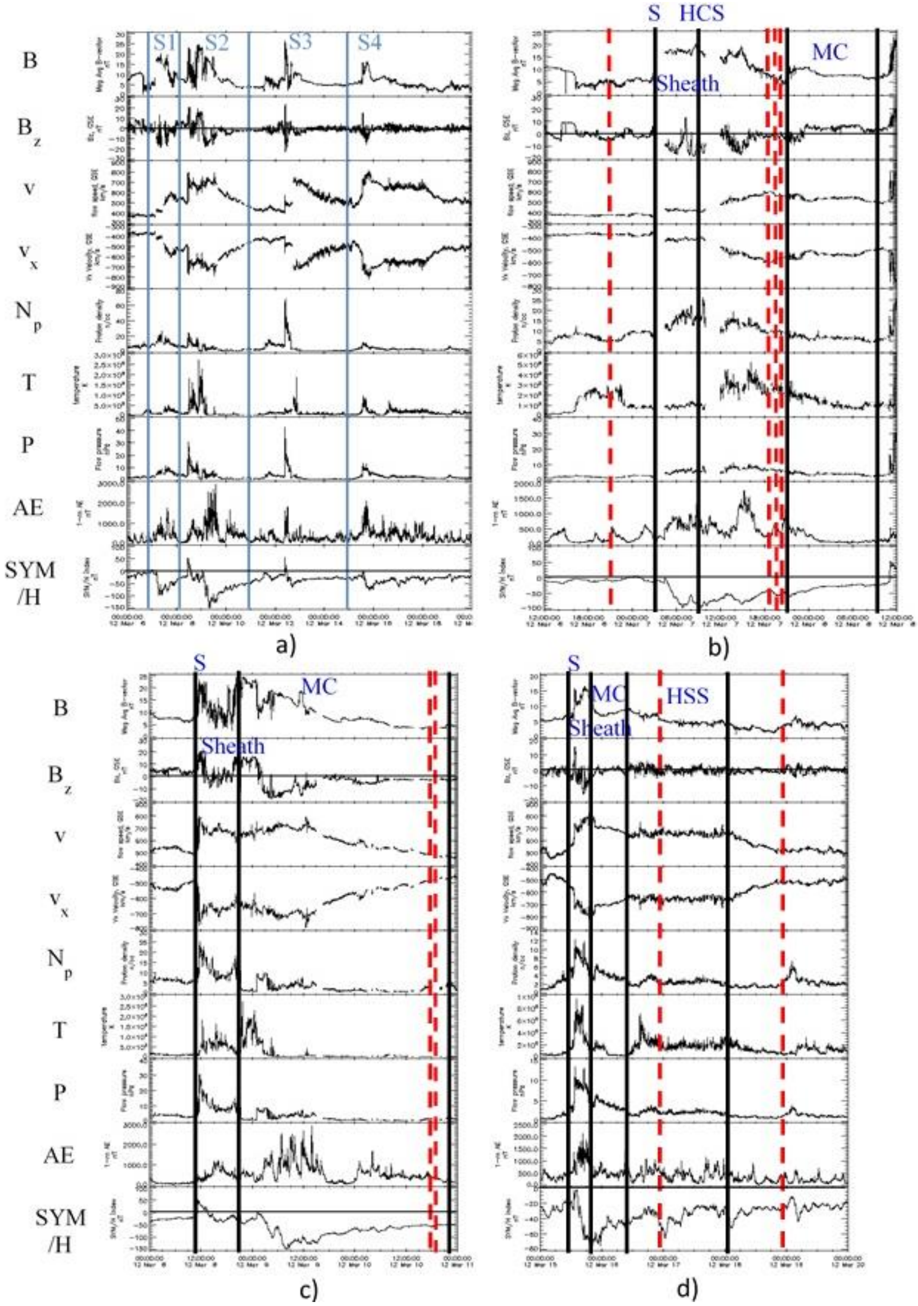

Fig. 1. a) Overview of the interplanetary conditions during the time period 7–20 March 2012; b) Detailed view of the interplanetary conditions during S1 event (6–8 March 2012); c) The same as b) for S2 event (8–11 March 2012); d) The same as b) for S4 event (15–20 March 2012).

Case 1. Substorm at 18:45 Universal Time (UT), 7 March 2012.

The substorm began during the first event (S1) of the disturbed interval 7-17 March 2012 during a storm with Dst_{min} = -98 nT caused by the southward directed sheath fields (Fig.1b). In Fig.2 are shown the variations of x magnetic field component from 12:00 to 24:00 UT on 7 March 2012 by the IMAGE meridional chain TAR-NAL. The substorm time is indicated by an ellipse. The magnetic disturbance began at *Oulujärvi* (OUJ) at CGM latitude=60.99°N and spread to *Sørøya* (SOR) at CGM latitude=67.34°N. The substorm development is presented in Fig. 3 by chosen images of the all-sky camera. The world directions are shown on the first image and UT is written above the images. The substorm occured during the recovery phase of the storm, near the maximal storm development and the *Dst* was -45 nT. Subtsorm auroras appeared in the South part of the field of view in 18:45 UT. The auroras moved towards North, reached zenith in about 18:53 UT and after that auroras surpassed it. The substorm development can be studied in more detail by the GC keograms (Fig. 4). In the GC keograms the substorm auroras are seen first in 18:52 UT. The substorm development is clearly expressed up to 19:20 UT.

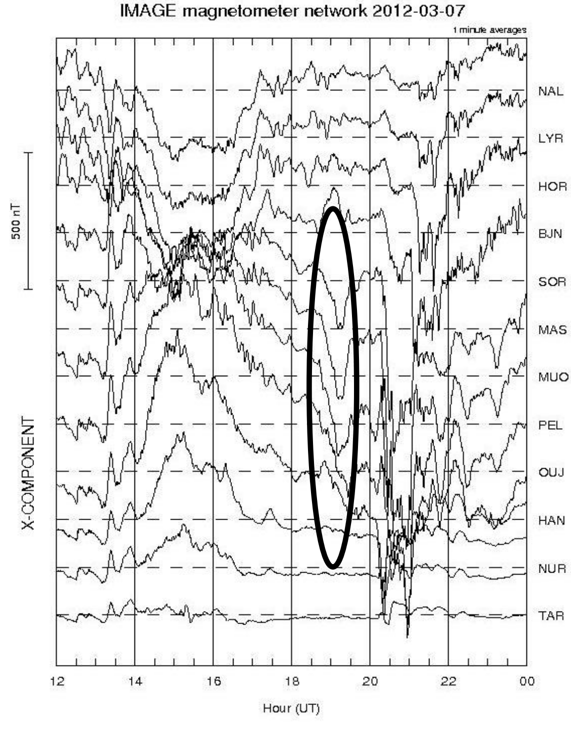

Fig. 2. Magnetic field x-component data, 12:00–24:00 UT, 7 March 2012. The substorm time is marked by an ellipse.

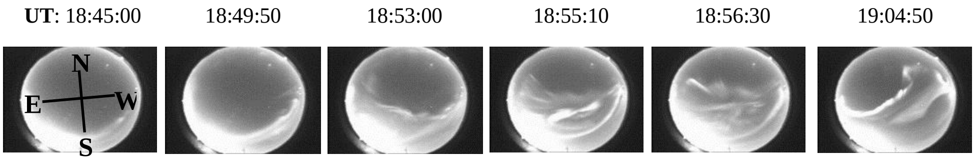

Fig. 3. The substorm development by all-sky images at 18:45 UT, 7 March 2012.

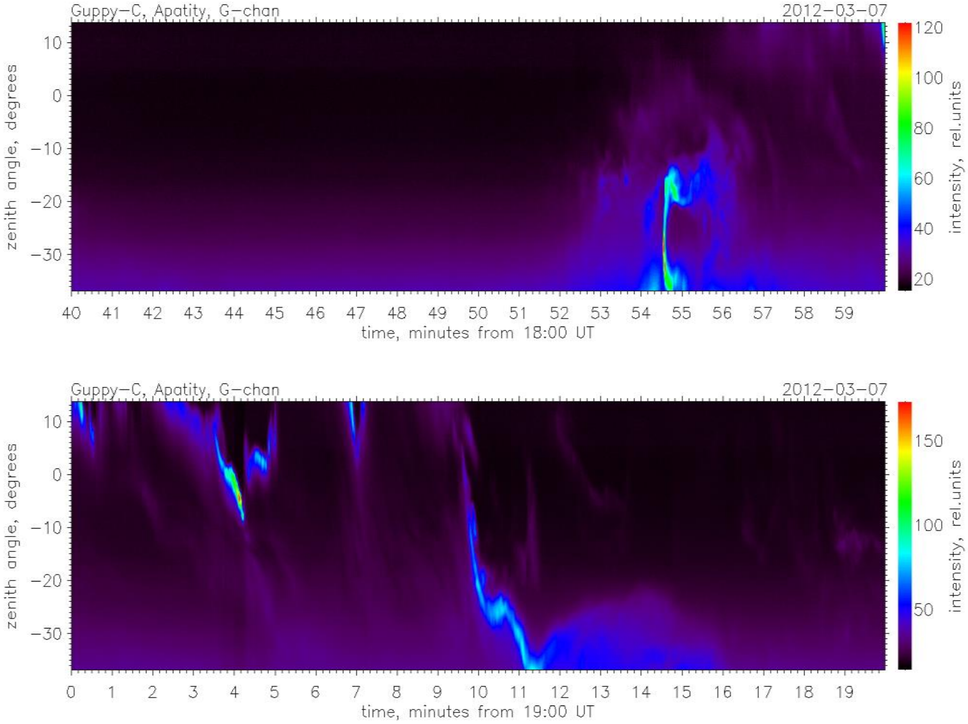

Fig. 4. The substorm development by the GC camera keograms: 18:40–19:00 UT (up) and 19:00–19:20 UT (down).

Case 2. Substorm at 18:35:50 UT, 10 March 2012.

The substorm developed during the second event (S2), when a geomagnetic storm was generated by a MC. $Dst_{\min}$ reached -148 nT. The substorm occurred in the late recovery phase, *Dst* was -50 nT (Fig. 1*c*). The magnetic field data during this time are shown in Fig. 5. The magnetic disturbance in this case was at higher geomagnetic latitudes. It extended from *Pello* (PEL) at 63.55°N

CGM lat. to *Longyearbyen* (LYR) at 75.12°N CGM lat. The substorm development is presented in Fig. 6 by selected AS images. The format is the same as in Fig. 3. The substorm onset over *Apatity,* towards the North of the station, was at 18:35:50 UT on 10.03.2012. The auroras traveled to South, reached zenith at 18:39 UT and moved further to South. A more detailed picture is given by the GC keograms (Fig. 7). In the keograms, the substorm auroras are seen from 18:38:30 UT at about 15° to North from zenith (the upper panel). The fast movement to South and the occupation of the field of view by substorm aurora are seen (the bottom panel).

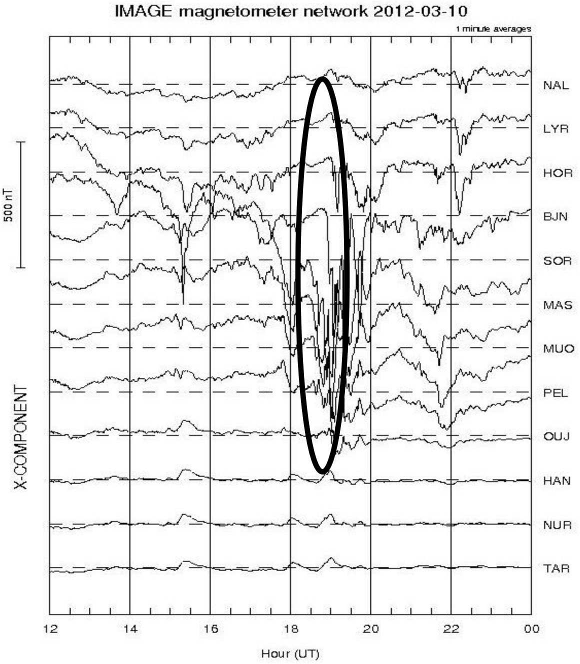

Fig. 5. Magnetic field x-component, 12:00–24:00 UT, 10 March 2012. The ellipse indicates the substorm time.

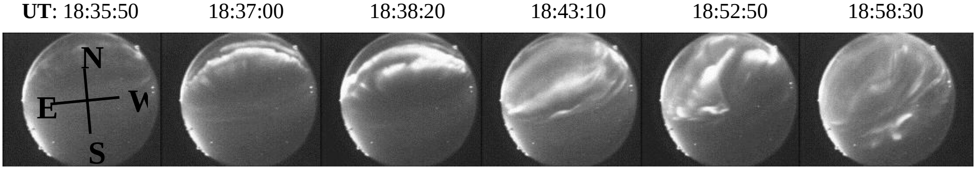

Fig. 6. Development of the substorm on 10 March 2012 at 18:35:50 UT by chosen all-sky images.

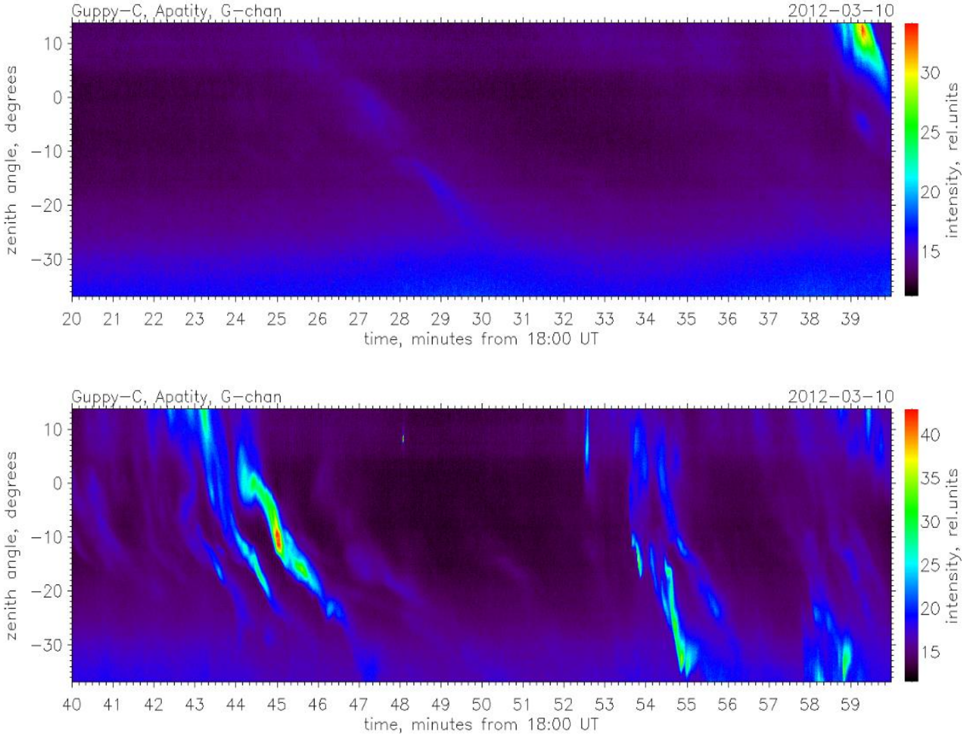

Fig. 7. The substorm on 10 March 2012 by the GC keograms: 18:20–18:40 (up) and 18:40–19:00 UT (down).

Discussion

We studied substorms occurring during the highly disturbed period 7–17 March 2012 when different sources in the solar wind provoked four consecutive geomagnetic storms by data of the *Apatity*'s MAIN system. The substorm onset location is connected to the auroral oval position. It is known that under normal condition, i.e. moderate disturbance, the auroral oval is located at ~65-67° CGM latitudes ("normal oval"), under quiet conditions the auroral oval shrinks and moves to higher latitudes (>70° CGM latitudes, "contracted oval"), and in disturbed conditions the oval expands up to 50° CGM latitude ("expanded oval") [13]. Thus, in quiet conditions *Apatity* (63.86° CGM latitude) is expected to turn out equatorward the auroral oval, and in disturbed conditions – poleward the auroral oval. This was confirmed by the observations of auroras in *Apatity* during 2012/2013 winter season [14].

Therefore, for substorms generated during a geomagnetic storm the onset location depends on the stage of storm development. During the main phase of the storm or in the recovery phase, but near the *Dst* minimum, the auroral oval lies to the South of *Apatity*, the substorm onset is to the South as well, and the flash of auroras from South to North is observed from the station (Case 1). During the recovery phase the auroral oval moves to higher latitudes and in the late recovery phase it is located to the North from *Apatity*. Then the substorm onset is to the North, and auroras propagate from North to South (Case 2). Besides, it appears that the *Dst* limit between the cases of onset to the South and the ones of onset to the North is not constant and depend on the rank of the geomagnetic storm. More observations are needed to find out how to estimate this limit.

Conclusions

It was shown that substorms, originated during strong geomagnetic storms near the *Dst* minimum, occurred to the South of *Apatity*, and substorm auroras expanded in North direction. For substorms during the late recovery phase, auroras were observed to the North of the *Apatity* station, and their motion from North to South was registered.

Acknowledgments

This study was supported by Program No 9 of the Presidium of the Russian Academy of Sciences (RAS). The study is part of a joint Russian-Bulgarian Project 1.2.10 of PGI RAS and Space Research and Technology Institute-Bulgarian Academy of Sciences (SRTI-BAS) under the Fundamental Space Research Program between RAS and BAS.

We are grateful to J. N. King and N. Papitashvili at AdnetSystems, NASA GSFC and CDAweb for providing the OMNI data.

References

1. Gonzalez, W. D., A. L. C. Gonzalez, B. T. Tsurutani. Dual-peek solar cycle distribution of intense geomagnetic storms, Planet. Space Sci. 38, 1990, 181–187.
2. Tsurutani, B. T., W. D. Gonzalez, A. L. C. Gonzalez, F. L. Guarnieri, N. Gopalswamy, M. Grande, Y. Kamide, Y. Kasahara, G. Lu, I. Mann, R. McPherron, F. Soraas, V. Vasyliunas, Corotating solar wind streams and recurrent geomagnetic activity: A review. J. Geophys. Res., 111, 2006, A07S01, doi:10.1029/2005JA011273.
3. Webb, D. F., R. A. Howard, The solar cycle variation of coronal mass ejections and the solar wind mass flux, J. Geophys. Res., 99, 1994, 4201-4220.
4. Burlaga, L. F., L. F. Klein, L. Sheeley, N. R. Michels, D. J. Howard, R. A. Koomen, M. J. Schwenn, H. Rosenbauer, A magnetic cloud and a coronal mass ejection, Geophys. Res. Lett., 9, 1982, 1317-1320.
5. Balogh, A., J. T. Gosling, J. R. Jokipii, R. Kallenbach, H. Kunow, Corotating interaction region, Space Sci. Rev., 89, 1999, 141-411.

6. Huttunen, K. E. J., H. E. J. Koskinen, A. Karinen, K. Mursula, Asymmetric development of magnetospheric storms during magnetic clouds and sheath regions, Geophys. Res. Lett., 33, 2006, L06107, doi: 10.1029/2005GL024894.
7. Pulkkinen, T. I., N. Y. Ganushkina, E. I. Tanskanen, M. Kubyshkina, G. D. Reeves, M. F. Thomsen, C. T. Russel, H. J. Singer, J. A. Slavin, J. Gjerloev, Magnetospheric current systems during stormtime sawtooth events, J. Geophys. Res., 111, 2006, A11S17, doi: 10.1029/2006JA011627.
8. Yermolaev, Yu. I., M. Yu. Yermolaev, Statistic study on the geomagnetic storm effectiveness of solar and interplanetary events, Adv. Space Res., 37, 2006, 1175-1181.
9. Schrijver, C. J. et al., Understanding space weather to shield society: A global road map for 2015-2025 comissioned by COSPAR and ILWS, Adv. Space Res., 55, 2015, 2745-2807.
10. Kozelov, B. V., S. V. Pilgaev, L. P. Borovkov, V. E. Yurov, Multi-scale auroral observations in Apatity: winter 2010-2011, Geosci. Insrum. Method. Data Syst., 1, 2012, 1-6.
11. Tsurutani, B. T., E. Echer, K. Shibata, O. P. Verkhoglyadova, A. J. Mannucci, W. D. Gonzalez, J. U. Kozyra, M. Pätzold, The interplanetary causes of geomagnetic activity during the 7-17 March 2012 interval: a CAWSES II overview, J. Space Weather Space Clim., 4, 2014, A02, doi: 10.1051/swsc/2013056.
12. Valchuk, T. E., , Solar wind and magnetic storms in the 24th Solar Activity Cycle, Astron. Tsirkulyar, N1585, 2013, ISSN 0236-2457.
13. Feldstein, Y. L., G. V. Starkov, Dynamics of auroral belt and polar geomagnetic disturbances, Planet. Space Sci., 15, 1967, 209-229.
14. Guineva, V., I. Despirak, B. Kozelov, Substorm observations in Apatity during 2012/13 winter season: a case study, Sun and geosphere, 10, 2015, 79-88.

СУББУРИ НАД АПАТИТИ ПРЕЗ ПЕРИОДА НА ПОВИШЕНА ГЕОМАГНИТНА АКТИВНОСТ 7-17 МАРТ 2012

В. Гинева, И. Деспирак, Б. Козелов, Р. Вернер

Резюме

Периодът 7-17 март 2012 г. е един от периодите с най-висока геомагнитна активност през възходящата фаза на 24 Слънчев цикъл. Поради това слънчевите и междупланетни явления през този период заедно с последващите процеси в магнитосферата и йоносферата са обект на изследване на научната общност. Цялата последователност от събития е дискутирана на няколко научни конференции. Слънчевите потоци, короналните дупки, короналните изхвърляния на маса, високоскоростните потоци в слънчевия вятър и междупланетните ударни вълни са идентифицирани и е изследвана реакцията на магнитосферата и йоносферата. През този период са настъпили 4 силни геомагнитни бури. Суббурите, възникнали през това време, са крайният ефект от всички тези събития. За да се установи началото на суббурите и да се проследи развитието им са използвани измервания от Multiscale Aurora Imaging Network (MAIN) в Апатити и данни от мрежата магнитометри IMAGE. Бяха изследвани характеристиките на тези суббури и бяха сравнени със суббури, възникнали при подобни или различни условия.

Bulgarian Academy of Sciences. Space Research and Technology Institute.
Aerospace Research in Bulgaria. 27, 2015, Sofia

LAND-USE/LAND-COVER CHANGE OF BISTRISHKO BRANISHTE BIOSPHERE RESERVE USING SENTINEL-2 SIMULATED DATA

Lachezar Filchev

Space Research and Technology Institute – Bulgarian Academy of Sciences
e-mail: lachezarhf@space.bas.bg

Abstract

The aim of this study is the evaluation of changes in land-use/land-cover on the territory of Bistrishko Branishte biosphere reserve (UNESCO, MAB), Vitosha; with the use of simulated Sentinel-2 data. For this purpose the CHRIS/PROBA image acquired on 22 June 2012, and on 28 September 2012 are geometrically and atmospheric corrected and co-registered. The topographic normalization is applied to the second image due to shadows cast on the slopes of the Valley of the river Bistrica. In order to simulate the Sentinel-2 bands, the spectral channels of the CHRIS/PROBA are spectraly resampled to spectral width of the Sentinel-2 bands. The spatial resampling of the Sentinel-2 bands is done using a Landsat 7 ETM + panhromatic band (15 m). On the classification of land-use/land-cover an accuracy assessment and cross-validation is made by using ground-based data. The results show that between 60 ha and 72 ha of coniferous plants were devastated by a forest fire in 2012. the results obtained demonstrate the ability of the Sentinel-2 mission to detect sudden changes in land-use/land-cover caused by forest fires.

1. Introduction

In recent decades the Land-Use and Land-Cover (LU/LC) change detection is used as one of the main tools to detect changes of Earth surface. With the advancement of preparation of *Sentinel-2* mission within the COPERNICUS Programme the LU/LC will become even more important tool to get insight of the changes that take place in Europe (Copernicus – observing the world, 2014). The protected forests in Europe are 39 million ha (nearly 19 %) (FOREST EUROPE, 2011) and *Bistrishko Branishte* biosphere reserve is part of them. Its protected area was designated to preserve a high-value Norway spruce (*Picea abies L.*) forests.

Present study aims at revealing LU/LC change of *Bistrishko Branishte* biosphere reserve using simulated *Sentinel-2* high-resolution satellite data. The time frame of the study is June – September 2012. During this period a significant change in the biosphere reserve's LU/LC took place due to a wildfire (Filchev and Dimitrov, 2013; Filchev *et al*. 2014).

1.1. Study area

The *Bistrishko Branishte* biosphere reserve was included in the UNESCO Man And Biosphere (MAB) Programme in 1977. It is located in the upper *Bistrica* river basin in the *Vitosha* Mountain between 1430 and 2282 m a.s.l. The designated protected area is 1061.6 ha (Georgiev, 1995), and according to official statistics 52 % of the reserve is occupied by forests, while the rest is covered with sub-alpine meadows, rocks, and rock screes. The dominant tree species is Norway spruce (*Picea abies L.*), represented by 7 forms and varieties. By 2010 > 27 % (~300 ha) of the reserve's territory was devastated by a tornado which occurred on 22 May 2001 (Gikov and Pironkova, 2005) and the successive European spruce bark beetle (*Ips typographus*) infestation (Filchev, 2012; Filchev *et al*. 2013; Panayotov *et al*., 2011; Panayotov and Georgiev, 2012). Following a wildfire in 2012 part of the dead tree stands (i.e. between 0.60 km^2 and 0.72 km^2) were burned (Filchev, 2012; Filchev *et al*. 2013, Filchev and Dimitrov, 2013; Gikov and Dimitrov, 2013; Panayotov and Georgiev, 2012; EUFODOS Newsletter, 2013).

2. Materials and methods

2.1. Data

The data used in this study consists of: 1) raster data: two Landsat 7 ETM+ and two CHRIS/PROBA Mode 1 images, a subset from ASTER GDEM V. 2; 2) vector data: a boundary (shape-file) of the *Bistrishko Branishte* biosphere reserve. Software used: BEAM VISAT (Brockmann Consult & ESA under GNU license), ArcGIS/ArcInfo 9.2 (ESRI Inc. under Academic License), ENVI 4.7 (Exelis ITT VIS under Academic License). The methodology of this study is presented on a flowchart (Fig. 1).

2.2. Sentinel-2 simulation procedure

Prior to simulation of *Sentinel-2* from CHRIS/PROBA a higher Spatial Resolution (SR) image was required to resample the original CHRIS/PROBA bands to the *Sentinel-2*'s SR. The *Sentinel-2* sensor will acquire its images in three SR modes, i.e. 10 m, 20 m, and 60 m (Fletcher, 2012). For this purpose two Landsat 7 ETM+ images, acquired on closer dates to CHRIS/PROBA acquisitions – i.e. before and after the wildfire, were selected from USGS LP DAAC online archive, (Table 1). The dates were selected to be as close as possible due to seasonal changes which effects on vegetation in the high-mountainous area. The image values of panchromatic band № 8 (15 m SR) of Landsat 7 ETM+, were converted from digital numbers (DN) to reflectance using the build in correction parameters in the metadata files (.MTL). Atmospheric correction was applied using the QUick Atmospheric Correction (QUAC) algorithm in ENVI (ENVI Atmospheric Correction Module, 2009).

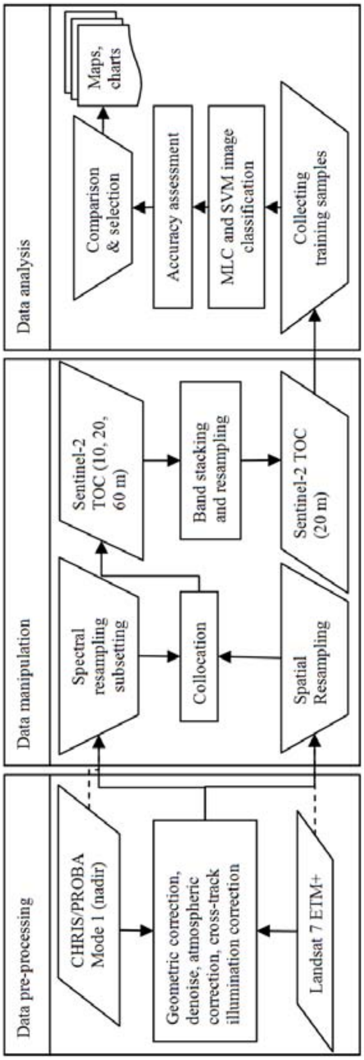

Fig. 1. Workflow of the study

Table 1. Dates of acquisition and ID of the Landsat 7 ETM+ and CHRIS/PROBA images used for simulation of the Sentinel-2 images

Landsat 7 ETM+ | Image ID(date)	CHRIS/PROBA Mode 1 | Image ID(date)
LE71840302012181ASN00 (29 June 2012) (PAN)	CHRIS_HQ_120622_E48E_41 (22 June 2012)
LE71840302012245ASN00 (1 September 2012) (PAN)	CHRIS_HQ_120928_EA88_41 (28 September 2012)

The first CHRIS/PROBA Mode 1 (CHRIS_HQ_120622_E48E_41_c) image used for *Sentinel-2* simulation was acquired on 22 June 2012, i.e. before the wildfire in the reserve. In present study it is used only the nadir image from the five image stack. The second post-fire CHRIS/PROBA Mode 1 image used in the analysis (CHRIS_HQ_120928_EA88_41) was acquired in nadir on 28 September 2012. Both images were spectrally resampled in ENVI 4.7 (Academic license) using the following band information, Table 2 (Law and Nichol, 2004; Drusch *et al*. 2012). The CHRIS/PROBA spectral coverage is not as wide as the one of *Sentinel-2*. Thus, only those *Sentinel-2* bands which correspond to the CHRIS/PROBA's bands in Mode 1 were simulated.

Table 2. Spectral characteristics of Sentinel-2 simulated bands. After Law and Nichol, (2004) and Drusch et al. (2012) with modifications

Sentinel-2' bands	Central wavelength λ (nm)	FWHM* (nm)
1	443	20
2	490	65
3	560	35
4	665	30
5	705	15
6	740	15
7	783	20
8	842	115
8b	865	20
9	945	20

*Full width at half maximum (FWHM)

The image was subsequently corrected for topography using Minnaert topography correction algorithm implemented in SAGA GIS (Verrelst *et al*. 2010). The so-formed bands were spectrally subset from the *Sentinel-2* simulated image (inheriting from CHRIS/PROBA the 30 m SR) in order to provide an input for simulation of 10, 20, and 60 m SR *Sentinel-2* bands. The spectral subsets are: 1) 2, 3, 4, and 8 bands (10 m SR); 2) 5, 6, 7, and 9 (natively the 8b *Sentinel-2* band) band (20 m SR); 3) 1 and 10 band (60 m SR) (Law and Nichol, 2004). Then the high resolution (15 m SR) panchromatic Landsat 7 ETM+ bands were degraded to 20 m SR. The next step in the simulation approach was collocating the Landsat 7 ETM+ spatially degraded panchromatic band to 20 m SR with the spectral subsets from *Sentinel-2* simulated images before and after the wildfire, using BEAM-VISAT 'Collocate' procedure. Three Top Of Canopy (TOC) (atmospherically corrected) *Sentinel-2* simulated images at three different SR (10 m, 20 m, and 60 m) were simulated for both dates. Finally, before image classification the simulated *Sentinel-2* bands were all stacked and spatially resampled to 20 m SR using Cubic Convolution (CC) algorithm.

2.3. Image classifications

On the stacked high-resolution (20 m SR) *Sentinel-2* TOC simulated image a supervised Maximum Likelihood Classification (MLC) and Support Vector Machines (SVM) image classifications were performed. The accuracy of the classification outputs were assessed after using a stratified random sampling (seed proportionally – 10 % to the class weigh). Finally, the areas estimated after the best performing classification algorithm were compared to each other.

3. Results and Discussions

The false colour composites of *Sentinel-2* TOC simulated images (20 m SR) from both dates are presented on (Fig. 2).

The major challenge in performing an image classification on the *Sentinel-2* simulated images was the difference in illumination conditions of two CHRIS/PROBA scenes due to the seasonal changes (Fig. 2). Those difference were persistent even after performing a topographic correction on the images which later on imposed on adding to the LU/LC classification scheme an additional LU/LC class ‘Shadows’. The quality of the second image was additionally deteriorated due to an airplane trail, which crossed just above the burnt area. The classification scheme for LU/LC classification is based on expert knowledge for the distinctive LU/LC classes on both images. The spectrally discriminated classes in present study are: 1) for first-date *Sentinel-2* simulated image: ‘Urban area’, ‘Rock screes’, ‘Grassland’, ‘Bushes’, ‘Broadleaf forest’, ‘Coniferous forest’, and ‘Unclassified’. The latter LU/LC class is practically void because no probability threshold was applied to either MLC or SVM and images were completely classified. This was done intentionally in order to assess whether the *Sentinel-2* spectral bands are providing enough information to discriminate between those classes; 2) for the second-date *Sentinel-2* simulated image some additional classes were introduced due to different image spatial coverage and the wildfire occurred in the nature reserve: ‘Water bodies’, ‘Fire scar’, and ‘Shadows’. The results from the LU/LC classifications differed significantly in their accuracies and barely reached 80 % accuracy. The worst performing LU/LC classification outputs were discarded in the subsequent analysis. On (Fig. 3) are presented the most accurate results for *Sentinel-2* image classification. The visual comparison, between 22 June 2012 and 28 September 2012 image classification results, bring some interesting insights to the seasonal changes and the changes in LU/LC caused by the wildfire in July 2012. Firstly, the ‘Shadows’ class is introduced in the LU/LC classification due to the high extent of shadows casted on the slopes of Bistrica river valley. The presence of this class is explained with the changed solar zenith angle due to the autumn season. The applied atmospheric and topographic corrections gave little visible effect which also reflected the introduction of the new ‘Shadows’ class. The thematic accuracy of classification of the ‘Fire scar’ class was also lessened due to the fact that the fire scar falls almost completely in the ‘Shadow’ class, see Fig. 2d and Fig. 3, image 2. Another complication was the presence of an airplane trail, which trespasses exactly over the burned up area as well as the atmospheric haze which was abnormal for this day, Fig. 2c. Furthermore, the extension of the ‘Rock screes’ class in expense of ‘Bushes’ and ‘Grassland’ classes are due to the seasonal changes of insulation and the drying out grass from mountain meadows which either uncover the rock screes in some places or become spectrally similar with the rocks.

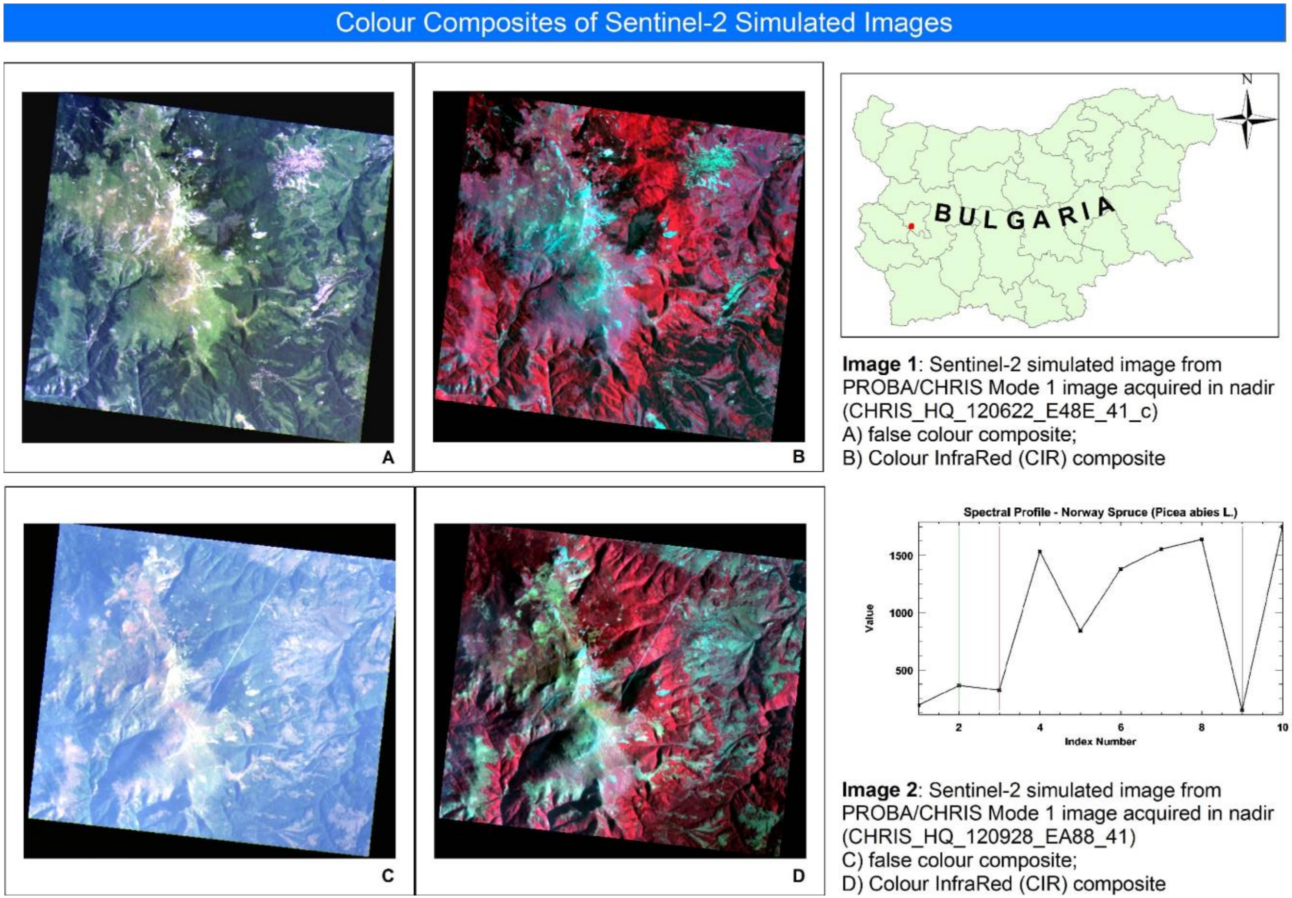

Colour Composites of Sentinel-2 Simulated Images

Image 1: Sentinel-2 simulated image from PROBA/CHRIS Mode 1 image acquired in nadir (CHRIS_HQ_120622_E48E_41_c)
A) false colour composite;
B) Colour InfraRed (CIR) composite

Image 2: Sentinel-2 simulated image from PROBA/CHRIS Mode 1 image acquired in nadir (CHRIS_HQ_120928_EA88_41)
C) false colour composite;
D) Colour InfraRed (CIR) composite

Fig. 2. Colour composites of Sentinel-2 TOC simulated images (20 m SR). A) and B) false-colour composites of Sentinel-2 TOC (22 June 2012); C) and D) false-colour composites of Sentinel-2 TOC (28 September 2012)

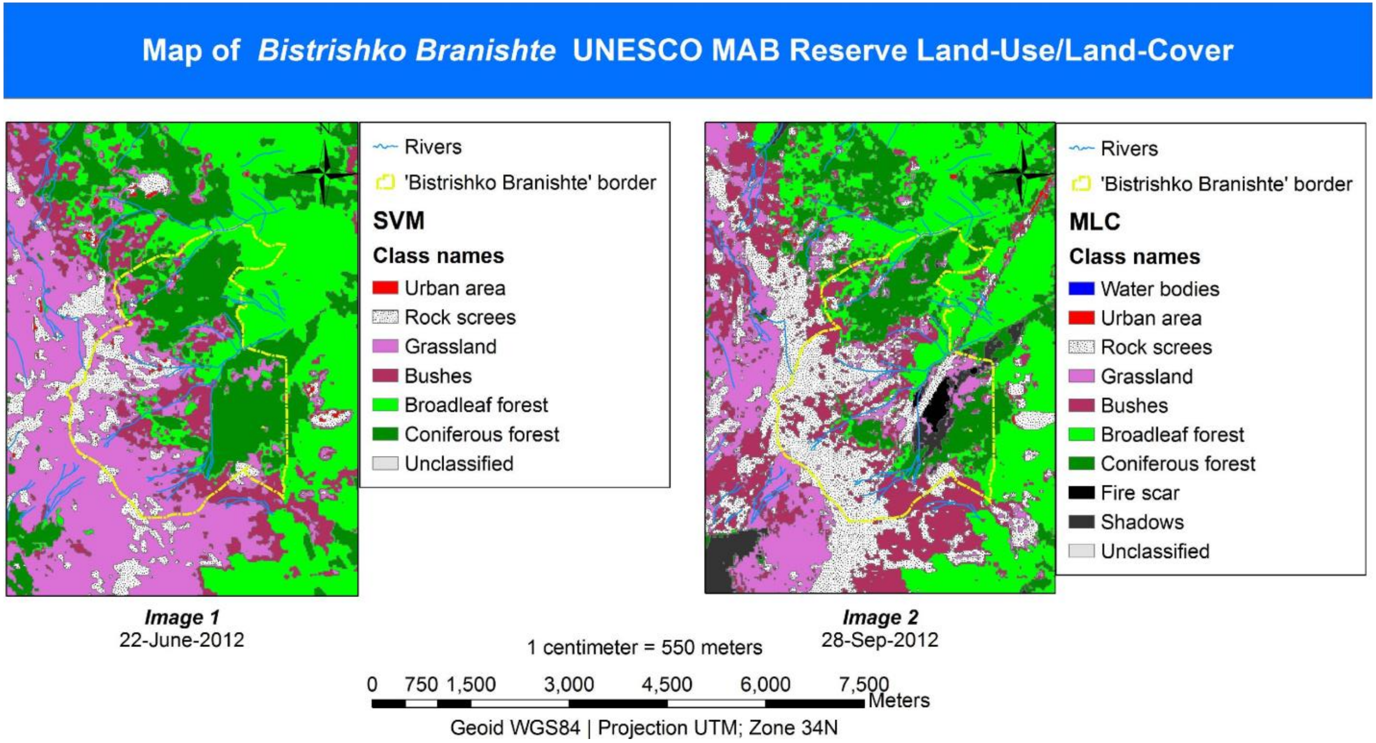

Fig. 3. LU/LC maps of Bistrishko Branishte UNESCO MAB reserve, prepared from the Sentinel-2 TOC simulated images

Table 3. Accuracy assessment of SVM LU/LC classification performed on Sentinel-2 TOC simulated image (22 June 2012) (in percentage)

LU/LC Class	Rock screes	Broadleaf forest	Grassland	Coniferous forest	Urban area	Bushes	Total
Rock screes	45.61	0	1.91	0	36.11	0	8.08
Broadleaf	0	98.31	1.27	22.22	0	5.88	28.65
Grassland	10.53	0	79.62	0	0	23.53	25.96
Coniferous	5.26	0	0	77.78	0	0	20.77
Urban area	38.6	1.69	0.64	0	63.89	0	9.23
Bushes	0	0	16.56	0	0	70.59	7.31
Total	100	100	100	100	100	100	100

Table 4. Accuracy assessment (omission and commission) of SVM LU/LC classification performed on Sentinel-2 TOC simulated image (22 June 2012) (cont.)

LU/LC class	Commission (Percent)	Omission (Percent)	Commission (Pixels)	Omission (Pixels)	Prod. Acc. (Percent)	User Acc. (Percent)	Prod. Acc. (Pixels)
Rock screes	38.1	54.39	16/42	31/57	45.61	61.9	26/57
Broadleaf forest	22.15	1.69	33/149	2/118	98.31	77.85	116/118
Grassland	7.41	20.38	10/135	32/157	79.62	92.59	125/157
Coniferous forest	2.78	22.22	3/108	30/135	77.78	97.22	105/135
Urban area	52.08	36.11	25/48	13/36	63.89	47.92	23/36
Bushes	68.42	29.41	26/38	5/17	70.59	31.58	12/17

The highest producer's accuracy features the 'Broadleaf forest' class, while the highest user's accuracy has 'Coniferous forest' and 'Grassland' classes. The 'Urban areas' class is largely misclassified with 'Rock screes' due to the spectral similarity of the materials used in urbanized areas with rocks. The results from for MLC LU/LC classification (after wildfire) are presented on Table 5 and Table 6. The overall accuracy of MLC is 76.98 %, which is well below for routine LU/LC mapping purposes (Kappa 0.7293). It could be inferred, that the highest user's accuracy has the 'Urban areas' class followed by 'Broadleaf forest', and 'Coniferous forest' class. Conversely, the highest producer's accuracy have in descending order 'Broadleaf forest', 'Bushes', 'Coniferous forest', and 'Urban areas' classes. This discrepancy is explained with the differences between ground-truth data and the classification output. Finally, the classification outputs were updated using on-screen digitizing to avoid the airplane trail. The mapped area is found to be close to formerly published estimates of the burnt area (Filchev, 2012; Filchev *et al*. 2013, Filchev and Dimitrov, 2013; Gikov and Dimitrov, 2013; Panayotov and Georgiev, 2012; EUFODOS Newsletter, 2013).

Table 5. Accuracy assessment of MLC LU/LC classification performed on Sentinel-2 TOC simulated image (28 September 2012) (in percentage)

LU/LC Class	Unclassified	Grasslands	Rock screes	Urban areas	Fire scar	Water bodies	Shadows	Bushes	Broadleaf forest	Coniferous forest	Total
Unclassified	0	0	0	0	0	0	0	0	0	0	0
Grasslands	0	83.51	38.16	11.86	7.69	0	4.08	10.91	0	0	20.42
Rock screes	62.5	1.03	56.58	8.47	0	18.18	0	0	0.86	0.75	9.4
Urban areas	0	4.12	0	74.58	0	0	0	0	0	0	7.78
Fire scar	0	0	0	0	23.08	0	0	0	0	0	0.49
Water bodies	0	0	0	0	0	54.55	0	0	0	0	0.97
Shadows	25	2.06	0	1.69	69.23	18.18	69.39	0	0	9.02	10.05
Bushes	12.5	7.22	3.95	1.69	0	9.09	0	89.09	4.31	0.75	11.02
Broadleaf forest	0	0	1.32	1.69	0	0	0	0	92.24	8.27	19.45
Coniferous forest	0	2.06	0	0	0	0	26.53	0	2.59	81.2	20.42
Total	100	100	100	100	100	100	100	100	100	100	100

Table 6. Accuracy assessment of MLC LU/LC classification performed on Sentinel-2 TOC simulated image (28 September 2012) (cont.)

Class	Commission (Percent)	Omission (Percent)	Commission (Pixels)	Omission (Pixels)	Prod. Acc. (Percent)	User Acc. (Percent)	Prod. Acc. (Pixels)	User Acc. (Pixels)
Unclassified	0	100	0/0	8/8	0	0	0/8	0/0
Grasslands	35.71	16.49	45/126	16/97	83.51	64.29	81/97	81/126
Rock screes	25.86	43.42	15/58	33/76	56.58	74.14	43/76	43/58
Urban areas	8.33	25.42	4/48	15/59	74.58	91.67	44/59	44/48
Fire scar	0	76.92	0/3	10/13	23.08	100	3/13	3/3
Water bodies	0	45.45	0/6	5/11	54.55	100	6/11	6/6
Shadows	45.16	30.61	28/62	15/49	69.39	54.84	34/49	34/62
Bushes	27.94	10.91	19/68	6/55	89.09	72.06	49/55	49/68
Broadleaf forest	10.83	7.76	13/120	9/116	92.24	89.17	107/116	107/120
Coniferous forest	14.29	18.8	18/126	25/133	81.2	85.71	108/133	108/126

Conclusions

In conclusion of present study, the following have been found:

The simulated *Sentinel-2* TOC data can serve for mapping and monitoring of coniferous, deciduous forests, and grasslands due to the achieved high-level of producer's and user's thematic accuracies, i.e. between 78 % and 98 %.

Depending on the illumination conditions, throughout the seasons, the accuracy of specific LU/LC classes such as 'Bushes', 'Rock screes', and 'Urban area' vary significantly, due to the spectral similarity.

The 'fire scar', area estimate by the second *Sentinel-2* TOC simulated image, was not found reliable enough due to the airplane trail which passed through the burnt area.

In summary, in future more studies on *Sentinel-2* capabilities of detection and mapping of forest-fire area estimation are needed.

4. Acknowledgements

The CHRIS/PROBA images used in the study were acquired within the ESA Third-Party Mission Category-1 Project No 8072 *Model for Assessment of Coniferous Vegetation Stress Using Multispectral and Hyperspectral Satellite Data*, PI: Dr. Lachezar Filchev. The author is also deeply appreciated to RSAC (UK) for the precise planning of the CHRIS/PROBA acquisitions during the summer campaign of 2012. The ASTER GDEM Ver.2 and Landsat 7 ETM+ satellite data is courtesy United States Geology Survey, Land Processes Distributed Active Archive Center (USGS LP DAAC), ERSDAC, National Aeronautics and Space Administration (NASA), and Ministry of Economy, Trade, and Industry (METI) of Japan. The ENVI (Exelis VIS) and ArcGIS 9.2/ArcInfo Academic licenses are property of SRTI-BAS.

References

1. Copernicus: observing the world. http://www.esa.int/Our_Activities/Observing_the_Earth/Copernicus [Date accessed 19/1/2015]
2. ENVI atmospheric correction module: QUAC and FLAASH user's guide, Version 4.7, 20AC47DOC, August, 2009 ITT VIS. http://www.exelisvis.com/portals/0/pdfs/envi/Flaash_Module.pdf [Date accessed 19/1/2015]
3. Ivanov, I. and V. Vassilev. Disaster mapping in a Bulgarian biosphere reserve. In: *EUFODOS Newsletter*, November 2013. http://www.eufodos.info/sites/default/files/downloads/EUFODOS_Newsletter13_1113_0.pdf [Date accessed 19/1/2015]
4. Filchev, L. An assessment of European spruce bark beetle infestation using Worldview-2 satellite data. In: Proceedings of European SCGIS conference: "Best practices: Application of GIS technologies for conservation of natural and cultural heritage sites", SRTI-BAS, Sofia, Bulgaria, 2012, 9–16. http://dx.doi.org/10.13140/2.1.3005.2647 [Date accessed 19/1/2015]

5. Filchev, L. and P. Dimitrov. Fire scars area estimation using CHRIS-Proba satellite data. In: CD Proceedings of the ESA Living Planet Symposium, 9–13 September, 2013, Edinburgh, United Kingdom (UK), ESA, 2013, SP-722, 163 p.
6. Filchev, L., M. Panayotov, and F. Ling. An assessment of land-use/land-cover change of Bistrishko Branishte biosphere reserve using Landsat data. In: IOP Conference Series: Earth and Environmental Science, 35th International Symposium on Remote Sensing of Environment (ISRSE'35), 22–26 April 2013, Beijing, China, 2014, Vol. 17, Paper ID 012060. http://dx.doi.org/10.1088/1755-1315/17/1/012060 [Date accessed 11-01-2015]
7. Filchev, L., M. Panayotov, and F. Ling. A study of Ips Typhographus pest infestation with the use of multi-angular CHRIS-Proba data. In: CD Proceedings of the ESA Living Planet Symposium, 9–13 September, 2013, Edinburgh, United Kingdom (UK), ESA, 2013, SP-722, 259 p.
8. Fletcher, K. (ed.). Sentinel-2: ESA's optical high resolution mission for GMES operational services. ESA. 2012, SP-1322/2.
9. Drusch, M., U. Del Bello, S. Carlier, O. Colin, V. Fernandez, F. Gascon, B. Hoersch, C. Isola, P. Laberinti, P. Martimort, A. Meygret, F. Spoto, O. Sy, F. Marchese, P. Bargellini. Sentinel-2: ESA's optical high resolution mission for GMES operational services. Remote Sensing of Environment, 120, 2012, 25–36. http://dx.doi.org/10.1016/j.rse.2011.11.026 [Date accessed 11-01-2015]
10. Forest Europe, UNECE and FAO 2011: State of Europe's forests 2011. Status and trends in sustainable forest management in Europe. http://www.foresteurope.org/docs/SoEF/reports/State_of_Europes_Forests_2011_Report_Revised_November_2011.pdf [Date accessed 11-01-2015]
11. Georgiev, G. People's parks and natural reserves in Bulgaria. Prosveta. 1995, 192 p. (In Bulg.)
12. Gikov, A. and Z. Pironkova. (2005). Using geoinformation technologies for assessment of tornado damages in forest areas. In: Proceedings of Scientific Conference with International Participation "Space, Ecology, Safety" (SES' 2005), 10–13 June 2005, Varna, Bulgaria, 269–274. (In Bulg.)
13. Gikov, A., P. Dimitrov. (2013). Application of medium resolution satellite images for assessment of damages caused by the wild fires in Vitosha mountain in 2012. In: Proceedings of 8th Science Conference with International Participation "Space, Ecology, Safety" (SES' 2012), SRTI-BAS, Sofia, 306–315. (URL: http://www.space.bas.bg/SES2012/R-2.pdf) (In Bulg.) [Date accessed 11-01-2015]
14. Law, K. H., J. Nichol. Topographic correction for differential illumination effects on Ikonos satellite imagery. International Society for Photogrammetry and Remote Sensing and Spatial Information Science (ISPRS). 35(3), 2004, 641–646. (URL: http://www.isprs.org/proceedings/XXXV/congress/comm3/papers/347.pdf) [Date accessed 11-01-2015]
15. Panayotov, M., D., Kulakowski, D. S. Laranjeiro, and P. Bebi. Wind disturbances shape old Norway spruce-dominated forest in Bulgaria. Forest Ecology and Management. 262, 2011, 470–481. http://dx.doi.org/10.1016/j.foreco.2011.04.013
16. Panayotov, M. and Georgiev, D. Dynamics in the Ips Typhographus outbreak following the 2001 windthrow in Bistrishko Braniste reserve. Silva Balcanica. 13(1), 2012, 38–48.

17. Sentinel-2 user guides - radiometric resolutions. https://earth.esa.int/web/sentinel/user-guides/sentinel-2-msi/resolutions/radiometric [Date accessed 11-01-2015]
18. Verrelst, J., J. G. P. W., Clevers, and M. E. Schaepman. Merging the Minnaert-k parameter with spectral unmixing to map forest heterogeneity with CHRIS/PROBA data. IEEE Transactions on Geoscience and Remote Sensing, 48(11), 2010, 4014–4022. http://dx.doi.org/10.1109/TGRS.2010.2047400 [Date accessed 11-01-2015]

ОЦЕНКА НА ПРОМЕНИТЕ В ЗЕМНОТО ПОКРИТИЕ НА БИОСФЕРЕН РЕЗЕРВАТ „БИСТРИШКО БРАНИЩЕ“ С ИЗПОЛЗВАНЕ НА СИМУЛИРАНИ SENTINEL-2 ДАННИ

Л. Филчев

Резюме

Целта на настоящото изследване е оценяването на промените в земеползването/земното покритие на територията на биосферен резерват „Бистришко бранище“ (ЮНЕСКО, МАВ) в ПП „Витоша“, с използването на спътникови данни от CHRIS/PROBA и симулирани данни от *Sentinel-2*. Заснетите на 22 юни 2012 г. и на 28 септември 2012 г. CHRIS/PROBA изображения, са геометрично и атмосферно коригирани и ко-регистрирани. Топографската нормализация е приложена на второто изображение поради хвърлената сянка върху склоновете на долината на река Бистрица. С цел симулиране на *Sentinel-2* данни спектралните канали на CHRIS/PROBA са спектрално ресамплирани по ширината на спектралните канали на Sentinel-2. Пространственото ресамплиране на съответните канали на *Sentinel-2* е направено с помощта на панхроматичен канал (15 m) от Landsat 7 ETM+. На направената класификация на земеползването/земното покритие е извършена оценка на точността и крос-валидация с помощта на наземни данни. Резултатите показват, че между 60 ha и 72 ha от иглолистна растителност са опустошени от горския пожар през 2012 г. Получените резултати доказват и потвърждават способността на *Sentinel-2* мисията за откриване на промени в земеползването/земното покритие.

Bulgarian Academy of Sciences. Space Research and Technology Institute.
Aerospace Research in Bulgaria. 27, 2015, Sofia

MAPPING SOFIA PLAIN ARABLE LAND DYNAMICS USING LANDSAT-8 OLI IMAGES AND GROUND DATA

Vassil Vassilev

Space Research and Technology Institute – Bulgarian Academy of Sciences
e-mail: vassilev_vas@yahoo.com

Abstract

The purpose of this article is mapping the arable land dynamics using satellite and ground data. The methodology of this article includes the following working stages: 1) Choosing appropriate satellite images; 2) applying arable land mask from CORINE 2006 land-cover database; 3) Deriving Normalized Difference Vegetation Index (NDVI) images and composing unsupervised classifications on the chosen satellite images; 4) Conducting per-pixel supervised classification using the Maximum Likelihood Classifier (MLC); 5) Applying accuracy assessment tool in ERDAS Imagine and deriving accuracy totals and Kappa statistics; 6) Mapping the arable land dynamics. The investigation shows good results for mapping arable land dynamics. The overall accuracy for the LANDSAT-8 Operational Land Imager (OLI) satellite image, acquired on 23.03.2014, is 77.66 % and Kappa statististics is 0.6906, while the image acquired on 14.08.2014 was estimated at 86.02 % overall accuracy and Kappa statistics of 0.7646. The analysis on the LANDSAT-8 image, acquired on 14.08.2014 shows that it can be used for controlling and monitoring the agricultural threathments accomplished by the farmers like harvest, for example. The presented research shows the big potencial using LANDSAT-8 OLI data for crop identification and mapping arable dynamics purposes at a relatively high accuracy.

1. Introduction[1]

Currently a major challenge in agricultural applications using high resolution (HR) satellite images is controlling area-based subsidies and applying precision agriculture practices. Satellite Remote Sensing (RS) provides synoptic, objective and relatively homogeneous data which can be geographically and temporally registered. Therefore, RS is an efficient tool for providing standard,

---

[1] Abreviations used:
MARS – Monitoring Agriculture with Remote Sensing
LACIE – Large Area Crop Inventory Experiment
CITARS – Crop Identification Technology Assessment for Remote Sensing
NDVI – Normalized Difference Vegetation Index

high quality information on agriculture, evenly over broad-scale territories. The Monitoring Agriculture with Remote Sensing (MARS) project of the European Union (EU) was established in order to define and demonstrate how RS can be used operationally to supplement, interpret, and standartize agricultural statistical data provided by conventional techniques (Meyer-Roux and Vossen, 1994; De Winne, 2004). Satellite RS techniques have been proven to be effective and useful in broad-scale agricultural surveys such as: Large Area Crop Inventory Experiment (LACIE) project in the USA and MARS project in Europe (Cohen and Shoshany, 2002). Furthermore, experiments from LACIE and Crop Identification Technology Assessment for Remote Sensing (CITARS) projects have also been conducted to demonstrate the capabilities of RS for crop inventory and forecasting (MacDonald, 1984; Blaes, 2005).

Winter wheat phenophases like tillering and flowering as well as harvest, can be successfully identified using sensors with different spatial resolution in various band combinations and severe ground surveys, including collecting information for defining training samples for the supervised classification (Townshend et al., 1991). A number of different methods have been developed during the last two decades to discriminate crop types using NDVI data from the Advanced Very High-Resolution Radiometer (AVHRR). These methods employ a variety of different approaches including temporal profiles of crop phenology manifested in the NDVI (DeFries et al., 1995; Reed et al., 1994), and classification of multi-temporal data (Brown et al., 1993; Loveland et al., 1995), which can be applied on variously managed crop areas worldwide.

Crop identification during the growing season is a major challenge for forecasting crop production as well as for controlling area-based subsidies in the EU member states (Blaes, 2005). The basis for separation of one crop from another is the supposition that each crop species has a unique visual appearance and spectral signature on the image. However, separating these species may be difficult because of variations in soil properties, fertilization, pest conditions, irrigation practices, planting dates, as well as intercropping, and tillage practices (Ryerson et al., 1997), all of which can be adopted in precision farming using high resolution satellite images. Thus, high resolution satellite images are the key to the above mentioned difficulties.

The purpose of this case study is mapping the arable land dynamics, and it includes the following tasks:1) Choosing appropriate satellite images; 2) Applying arable land mask from CORINE 2006 land-cover database; 3) Deriving NDVI images and composing unsupervised classifications on the chosen satellite images; 4) Conducting per-pixel supervised classification using the Maximum Likelihood Classifier (MLC); 5) Applying accuracy assessment tool in ERDAS Imagine and deriving accuracy totals and Kappa statistics; 6) Mapping of the arable land dynamics.

2. Materials, methods and data used

2.1. Study area

The study area is part of the *Sofia* plain, surrounding the capital city of *Sofia*. The major cultivated winter crops (winter wheat and winter barley) and spring crop (sunflower) were investigated in the present case study.

2.2. Ground data used

On 30.06.2014 a field survey was conducted where ground data was collected and organized in a GIS geodatabase. The ground-truth data consists of descriptions of the LU/LC types, phenological stages and vegetation cover of crops, GPS measurements, and photos. The collected ground data will contribute of selecting appropriate training samples for the supervised classification on the chosen satellite images.

2.3. Satellite data used

There are two LANDSAT-8 Operational Land Imager (OLI) satellite images chosen for the present study for the year 2014 acquired on: 23.03.2014 and 14.08.2014 (Fig. 1.).

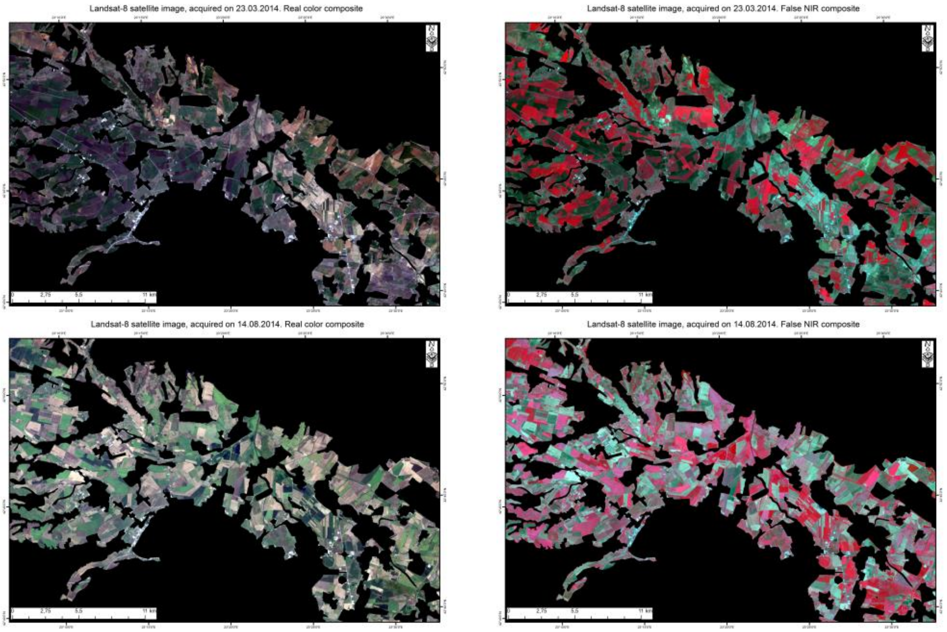

Fig. 1. Selected satellite images from LANDSAT-8 OLI, acquired on 23.03.2014 (top) and 14.08.2014 (bottom)

Table 1. LANDSAT-8 OLI main characteristics

LANDSAT-8 Operational Land Imager (OLI) and Thermal Infrared Sensor (TIRS)	**Bands**	**Wavelength (μm)**	**Resolution (m)**
	Band 1 - Coastal aerosol	0.43 – 0.45	30
	Band 2 - Blue	0.45 – 0.51	30
	Band 3 - Green	0.53 – 0.59	30
	Band 4 - Red	0.64 – 0.67	30
	Band 5 - Near Infrared (NIR)	0.85 – 0.88	30
	Band 6 - SWIR 1	1.57 – 1.65	30
	Band 7 - SWIR 2	2.11 – 2.29	30
	Band 8 - Panchromatic	0.50 – 0.68	15
	Band 9 - Cirrus	1.36 – 1.38	30
	Band 10 - Thermal Infrared (TIRS) 1	10.60 – 11.19	100 * (30)
	Band 11 - Thermal Infrared (TIRS) 2	11.50 – 12.51	100 * (30)

3. Results and discussions

3.1. Applying arable land mask from CORINE 2006 land-cover database

The “2.1.1. Non-irrigated arable land” class was used to build the mask layer from the CORINE Land Cover (CLC) 2006 database in order to classify only the arable land and reduce the occurrence of mixed pixels.

3.2. Deriving NDVI images and composing unsupervised classifications on the chosen satellite images

The *k*-mean and Iterative Self-Organizing Data Analysis (ISODATA) clustering algorithms are the most frequently used ones in RS. The ISODATA algorithm was selected in this study because it allows different number of clusters, while the *k*-mean algorithm assumes that the number of clusters is known *a priori* (Groom et al., 1996; Garcia-Consuerga and Cisneros, 1999; Yang et al., 1999). Unsupervised ISODATA cluster classification with six classes was applied to spectraly discriminate the crops and to collect the necessary information in order to delineate the training samples for the supervised per-pixel classification.

The crop identification process was accomplished firstly by conducting unsupervised classification (using ISODATA algorithm) with 5–6 classes for each satellite image (Fig. 2 and Fig. 3). This spectral information was used together with the ground data as an indicator where to draw training samples for the supervised classification. The unsupervised classification is traditionally the first step and is accommodating the interpretation of the images. The most commonly used RS vegetation index for agricultural applications is the NDVI, expressed by the following formula: NDVI=(NIR-VIS)/(NIR+VIS), where VIS and NIR stands for the spectral reflectance measurements acquired in the visible red and near-infrared regions, respectively (Rouse et al., 1973). NDVI is a commonly used space-observed measure of the chlorophyll activity (Fig. 4 and Fig. 5). It ranges typically from 0.15 (bare soils) to 0.80 (dense vegetation).

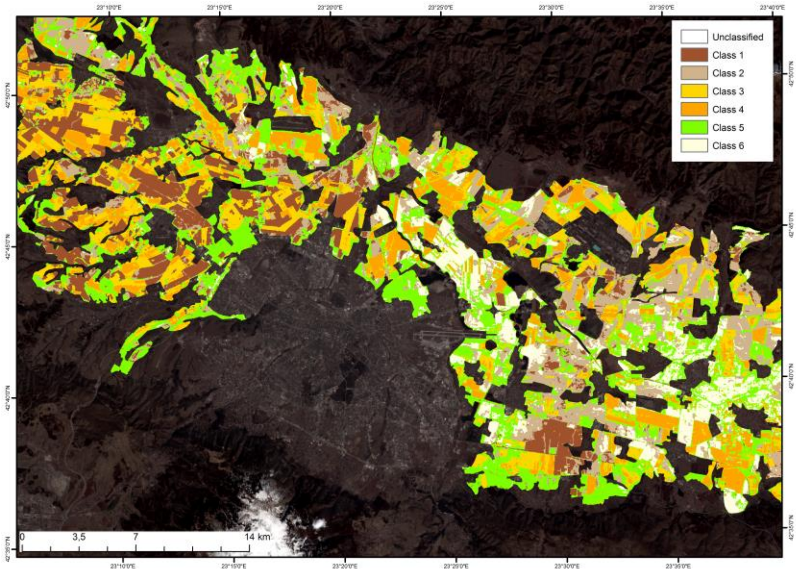

Fig. 2. Unsupervised classification of LANDSAT-8 OLI image acquired on 23.03.2014

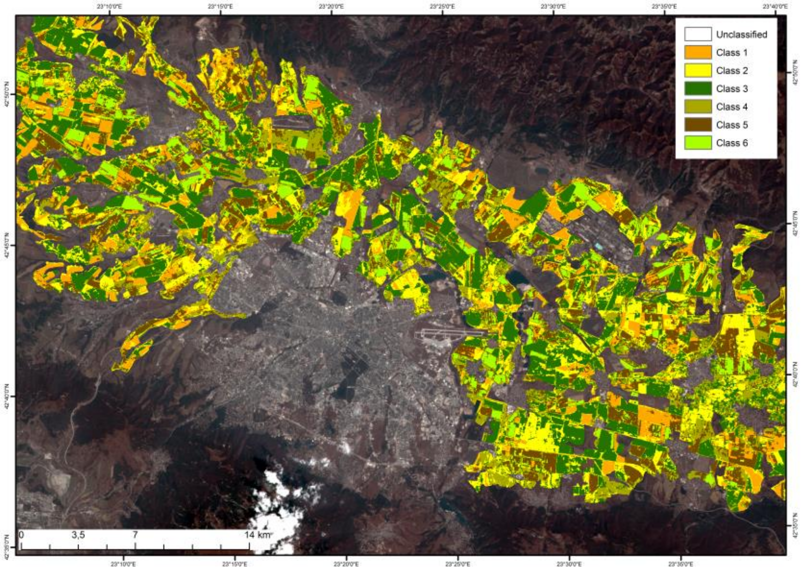

Fig. 3. Unsupervised classification of LANDSAT-8 OLI image acquired on 14.08.2014

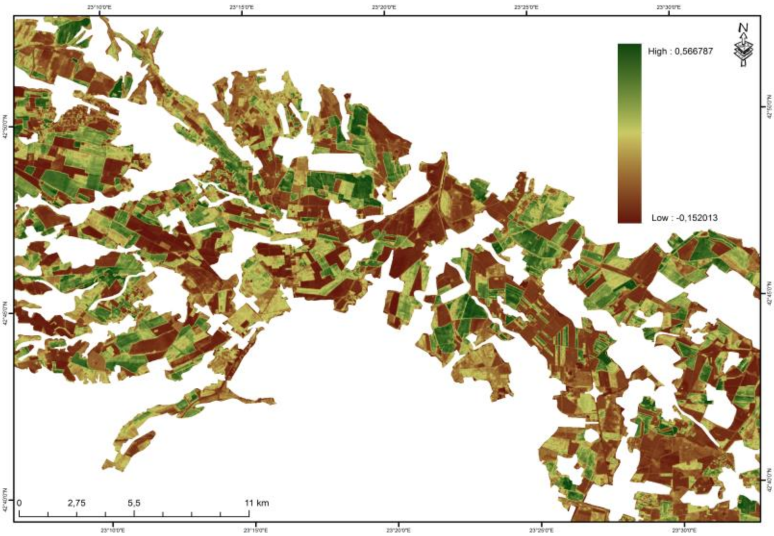

Fig. 4. NDVI image derived from LANDSAT-8 OLI satellite image acquired on 23.03.2014

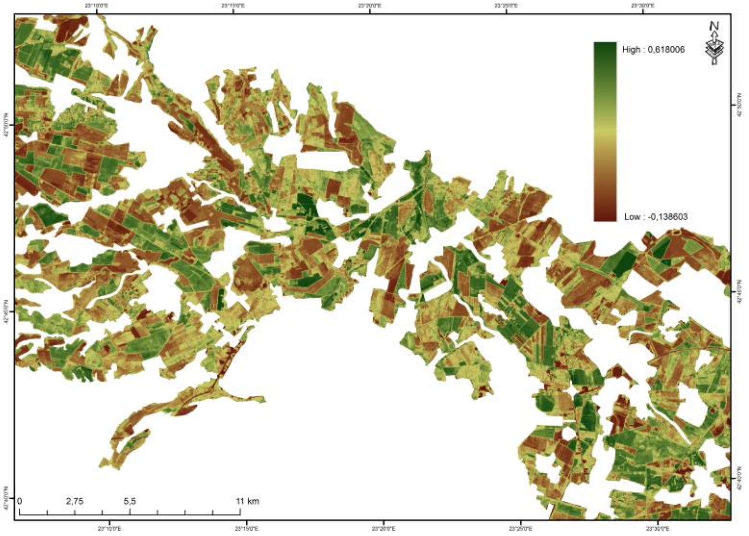

Fig. 5. NDVI image derived from LANDSAT-8 OLI satellite image acquired on 14.08.2014

3.3. Conducting per-pixel supervised classification using the Maximum Likelihood Classifier (MLC) algorithm for crop identification

Per-pixel supervised classification using the MLC algorithm was applied on the arable territories of the test site for crop identification purposes. In the MLC procedure, at least 10–15 independent training cases per class were used, so that its mean and variance can be estimated (Piper, 1992). For example, the spectral response of an agricultural crop class in an image might vary as a function of variables such as: the crops growth stage, topographic position, density of vegetation cover, health, impact of management activities, substrate conditions and instrument view angle (Foody, 2002). The gathered training set from the field data was good enough to make representative training samples for the arable land classes. The unsupervised classification in combination with the ground information helped to choose and delineate appropriate training samples for the supervised classification of the chosen satellite image. The identified classes for the LANDSAT-8 image, acquired on 23.03.2014 are: ‘winter crop condition classes’ (normal state; good state, and very good state), ‘bare soil asphalt and roads’, ‘cultivated arable land/shrubs, grass and meadows’, and ‘cultivated arable land’. For the LANDSAT-8 image, acquired on 14.08.2014 the identified classes are: ‘tillage fields’, ‘spring crops’, and ‘stubble fields’.

3.4. Applying accuracy assessment tool in ERDAS Imagine and deriving accuracy totals and Kappa statistic

Around 100 randomly distributed points were assessed applying the accuracy assessment tool on the classified images for crop identification using visual interpretation on the image, the unsupervised classifications, derived NDVI image, and the ground collected data as a reference.

The achieved results for the per-pixel supervised classification from 23.03.2014 show overall classification accuracy of 77.66 % and overall Kappa statistics of 0.6906 (Table 2). While, the per-pixel supervised classification from 14.08.2014 shows overall classification accuracy of 86.02 % and overall Kappa statistics of 0.7646 (Table 3). For the classification on 23.03.2014 there are not enough reference points to assess reasonable accuracy for winter crops classes – ‘very good state’ and ‘cultivated arable land’.

Table 2. Accuracy totals for supervised classification on NDVI from LANDSAT-8 OLI acquired on 23.03.2014

Class Name - state	**Reference Totals**	**Classified Totals**	**Number Correct**	**Accuracy (%)**	
				Producers	**Users**
Winter Crop – very good	2	2	2	100.00	100.00
Winter Crop – normal	19	23	15	78.95	65.22
Winter Crop – good	12	10	5	41.67	50.00
Bare soil, asphalt, and roads	41	36	33	80.49	91.67
Cultivated land/shrubs/grass/meadows	19	22	17	89.47	77.27
Cultivated arable land	1	1	1	100.00	100.00
Overall	**94**	**94**	**73**	**Accuracy – 77.66 %**	**Kappa – 0.6906**

Table 3. Accuracy totals for supervised classification on NDVI from LANDSAT-8 OLI acquired on 14.08.2014

Class Name	**Reference Totals**	**Classified Totals**	**Number Correct**	**Accuracy (%)**	
				Producers	**Users**
Tillage fields	12	7	7	58.33	100.00
Spring crops	46	38	38	82.61	100.00
Stubble fields	35	48	35	100.00	72.92
Overall	**93**	**93**	**80**	**Accuracy – 86.02 %**	**Kappa – 0.7646**

3.5. Mapping of the arable land dynamics

The mapping of the arable land dynamics is presented in Fig. 8 and Fig. 9.

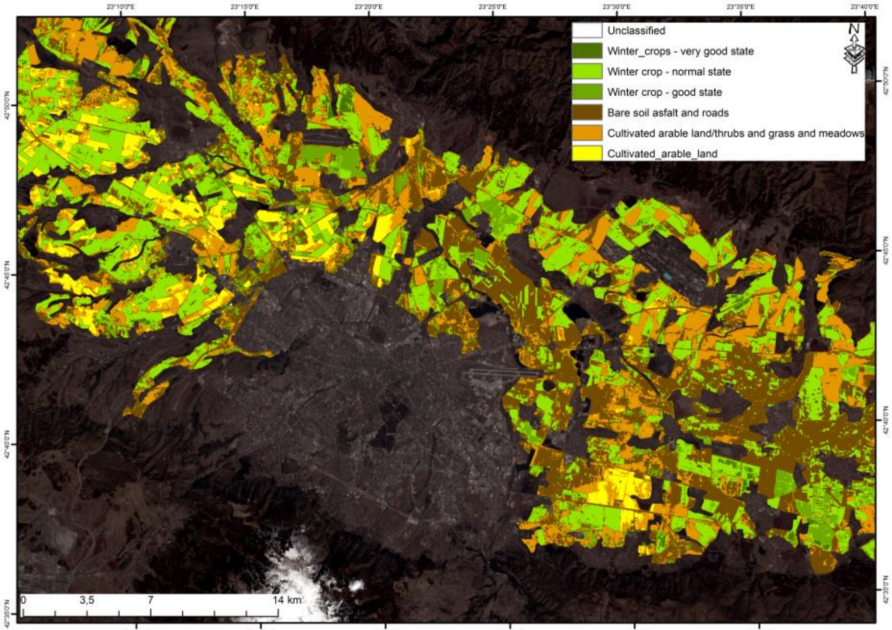

Fig. 6. Supervised MLC on satellite image from LANDSAT-8 OLI acquired on 23.03.2014

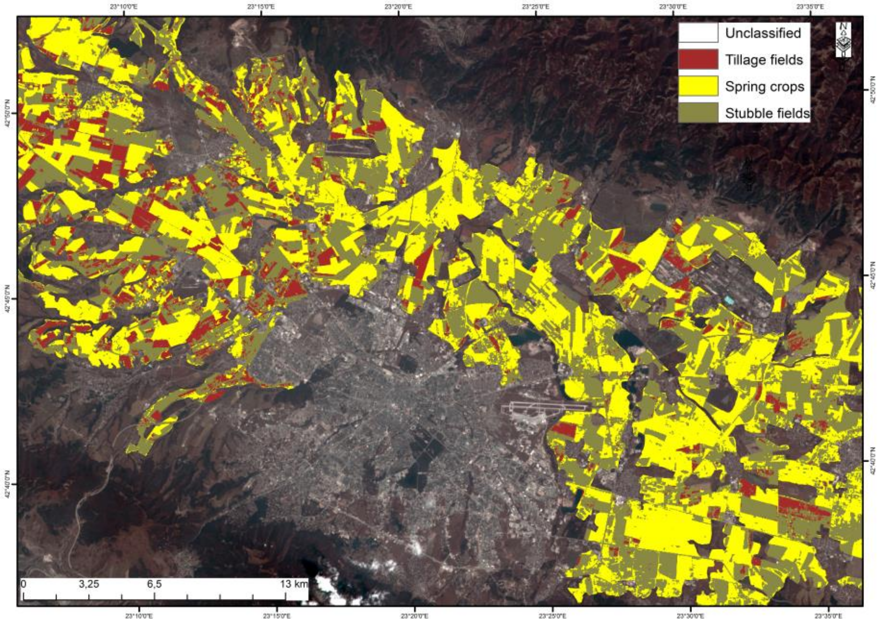

Fig. 7. Supervised MLC on LANDSAT-8 satellite image acquired on 14.08.2014

The distrubutuion of classes of each resulted classification derived from the LANDSAT-8 OLI images are presented in Fig. 8.

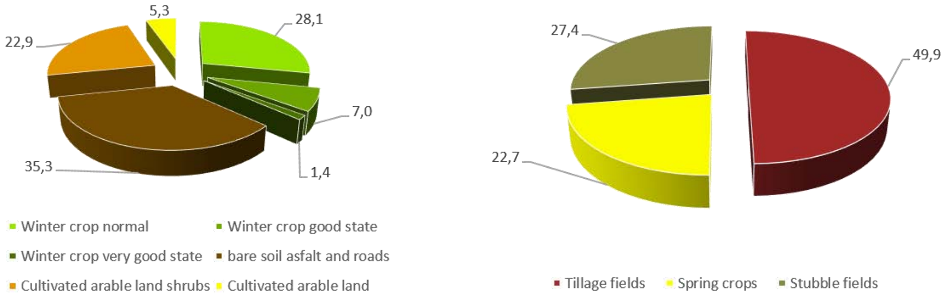

Fig. 8. Distribution of classes (%) for classification on 23.03.2014 (left) and 14.08.2014 (right)

4. Conclusions

The applied methodology emphazises on extracting valuable arable land dynamics information that can be directly utilized by the authorities. The arable land mask can increase the quality of the crop identification process, consequently on the accurate extraction of arable land dynamics information. The analysis on the LANDSAT-8 OLI satellite image acquired on 14.08.2014, shows that it can be used for controlling and monitoring the agricultural threathments accomplished by the farmers like harvest, for example. The presented research shows the big potencial using LANDSAT-8 OLI data for crop identification and mapping arable dynamics purposes at a relatively high accuracy.

Refferences

1. Meyer-Roux, J., Vossen P. (1994). The first phase of the MARS project, 1988–1993: overview, methods and results. In: Official Publications of the E.U., Luxembourg (Ed.), Report EUR 15599 EN. Conference on the MARS project: Overview and prospectives, Belgirade, 1994, 33–79.
2. De Winne, P. (2004). Les Besoins de la Direction Generale VI: Agriculture. In: Office for official publications of the E.U., Luxembourg (Ed.), Report EUR 15599 EN, 2004. Conference on the MARS project: Overview and prospectives, Villa Carlotta, Belgirate, Lake Maggiore, Italy, 17–22 (in French).
3. Cohen, Y., M. Shoshany. (2002). A national knowledge-based crop recognition in Mediterranean environment International Journal of Applied Earth Observation and Geoinformation, 4, 75–87.
4. MacDonald, R. (1984). IEEE Transaction on Geoscience & Remote Sensing, GE-22, 473–481.
5. Blaes, 2005. Efficiency of crop identification based on optical and SAR image time series. Remote Sensing of Environment, 96 352–365.
6. Townshend, J., Justice C., Li W., Gurney C., McManus J. (1991). Global land cover classification by remote sensing: present capabilities and future possibilities. Remote Sens Environ, 35, 243–255.
7. DeFries, R., Hansen M., Townshend J. (1995). Global discrimination of land cover types from metrics derived from AVHRR pathfinder data. Remote Sens Environ, 64 (3), 209–222.
8. Reed, B. C., Brown J. F., VanderZee D., Loveland T. R., Merchant J. W., Ohlen D. O. (1994). Measuring phenological variability from satellite imagery. Journal of Vegetation Science, 5, 703–714.
9. Brown, J. F., Loveland T. R., Merchant J. W., Reed B. C., Ohlen D. O. (1993). Using multisource data in global land-cover characterization: Concepts, requirements, and methods. Photogramm Eng Remote Sens, 59(6), 977–987.
10. Loveland, T. R., Merchant J. W., Brown J. F., Ohlen D. O., Reed B. C., Olson P., Hutchinson J. (1995). Seasonal land-cover regions of the United States. Annals of the Association of American Geographers, 85, 339–355.
11. Ryerson, R. A., Curran P. J., Stephens P. R. (1997). Agriculture. In: Philipson W.R. (Ed.) Manual of Photographic Interpretation. 2nd ed. Americal Society for Photogrammetry and Remote Sensing, Bethesda, MD, 365–397.

12. Rouse, J., Haas R., Schell J., Deering D. 1973. Monitoring vegetation systems in the Great Plains with ERTS. In: Third ERTS Symposium, 1973, NASA SP-351 I, 309–317.
13. Groom, B.G., Fuller R. M., Jones A. R. 1996. Contextual correction: techniques for improving land-cover from remotely sensed images. Int J Remote Sens, 17, 69-89.
14. Garcıa-Consuegra, J., Cisneros G. (1999). Establishing spatially continuous in a non-supervised way. In: Proceedings of the IEEE International Geoscience and Remote Sensing Symposium (IGARSS'99), 1999, Hamburg, Germany.
15. Yang, H., Khorram, S., Dai X.L. (1999). Applications of simulated annealing minimization technique to unsupervised classification of remotely sensed data. In: Proceedings of the IEEE International Geoscience and Remote Sensing Symposium (IGARSS'99), 1999, Hamburg, Germany.
16. Piper, J. (1992). Variability and bias in experimentally measured classifier error rates. Pattern Recognition Letters, 13, 685–692.
17. Foody, G. M., (2002). Status of land cover classification accuracy assessment. Remote Sens. Environ. 80, 185–201.

КАРТОГРАФИРАНЕ НА ДИНАМИКАТА НА ЗЕМЕДЕЛСКАТА ТЕРИТОРИЯ НА СОФИЙСКАТА КОТЛОВИНА ПО СПЪТНИКОВИ ИЗОБРАЖЕНИЯ ОТ LANDSAT-8 И НАЗЕМНА ИНФОРМАЦИЯ

В. Василев

Резюме

Целта на настоящето изследване е картографиране на динамиката на земеделска територия по спътникови и наземни данни. Методологията на изследването включва следните работни етапи: 1) Избор на спътникови изображения; 2) Прилагане на маска с обработваемите земи в района на изследването от базатаданни на CORINE 2006 земно покритие; 3) Създаване на NDVI изображение и прилагане на неконтролирана класификация върху избраните изображения; 4) Прилагане на пикселно-ориентирана класификация по принципа на максималното подобие; 5) Прилагане на инструмент за оценка на точността в програмния продукт ERDAS Imagine и извличане на общата точност и капа статистиката; 6) картографиране на динамиката на земеделската територия.

Резултатите от проведеното изследване показват добра точност на картографиране на динамиката на земеделската територия. Общата точност за изображението заснето на 23.03.2014 г. е 77.66% с Капа статистика от 0.6906, докато това заснето на 14.08.2014 г. има обща точност от 86.02% и Капа статистика от 0.7646. От анализа проведен върху изображението заснето на 14.08.2014 г. може да се контролира и следи кога земеделските собственици са извършили определена дейсност, като жътвата, например. Проведеното изследване показа големия потенциал на LANDSAT-8 OLI за разпознаване на земеделски култури и картографиране на динамиката на земелските култури с относително висока точност.

Bulgarian Academy of Sciences. Space Research and Technology Institute.
Aerospace Research in Bulgaria. 27, 2015, Sofia

MAPPING CROP CONDITION USING QUICKBIRD-2 AND WORLDVIEW-1 SATELLITE IMAGES AND DERIVED PRODUCTS. A PRECISION AGRICULTURE CASE STUDY FOR PART OF ZHITEN TEST SITE IN NORTHEAST BULGARIA

Vassil Vassilev, Eugenia Roumenina

Space Research and Technology Institute – Bulgarian Academy of Sciences
e-mail: vassilev_vas@space.bas.bg; roumenina@space.bas.bg

Abstract

The purpose of this article is to investigate the possibilities of mapping crop condition using high resolution (HR) satellite images for Zhiten test site situated in Northeast Bulgaria. The chosen satellite images are acquired from multispectral QuickBird-2 and panchromatic WorldView-1 sensors on 31/05/2009 and 30/11/2011, respectively. The methodology of this article includes the following working stages: 1) applying arable mask from CORINE 2006 land-cover database; 2) conducting per-pixel supervised classification using the Maximum Likelihood Classifier (MLC) algorithm for crop identification; 3) applying accuracy assessment tool in ERDAS Imagine and deriving accuracy totals and Kappa statistics; 4) mapping crop condition using Normalized Difference Vegetation Index (NDVI), Renormalized Difference Vegetation Index (RDVI) and Soil Adjusted Vegetation Index (SAVI) indices. The overall classification accuracy for the QuickBird-2 image is 90.86 % and overall Kappa statistics is 0.8538, while for the WorldView-1 image is 86.71 % and overall Kappa statistics is 0.7721. The SAVI shows better sensitivity for the spring crops cultivars with less than 40 % vegetation cover. Meanwhile, the NDVI gives good results for winter crops, but saturates at high vegetation dencity and gives generalized results for values less than 0.40. Overall RDVI gives better crop condition results for winter crops at flowering and grain filling phenophases and spring crops at vegetative phase compared to NDVI and SAVI.

1. Introduction[1]

Currently a major challenge in agricultural applications is forecasting crop production using low and coarse resolution satellite images, while for high

---

[1] Abreviations used:
MARS – Monitoring Agriculture with Remote Sensing
LACIE – Large Area Crop Inventory Experiment
CITARS – Crop Identification Technology Assessment for Remote Sensing
NDVI – Normalized Difference Vegetation Index
RDVI – Renormalized Difference Vegetation Index
SAVI – Soil Adjusted Vegetation Index

resolution (HR) satellite images one of the hottest topics is controlling area-based subsidies and applying precission agriculture practices amongst others. Satellite Remote Sensing (RS) provides synoptic, objective and relatively homogeneous data which can be geographically and temporally registered. Therefore, RS is an efficient tool for providing standard, high quality information on agriculture, evenly over broad-scale territories. The Monitoring Agriculture with Remote Sensing (MARS) project of the European Union was established in order to define and demonstrate how RS can be used operationally to supplement, interpret, and standardize agricultural statistical data provided by conventional techniques (Meyer-Roux and Vossen, 1994; De Winne, 2004). Satellite RS techniques have been proven to be effective and useful in broad-scale agricultural surveys such as: Large Area Crop Inventory Experiment (LACIE) project in the USA and MARS project in Europe (Cohen and Shoshany, 2002). Additonally, experiments from LACIE and Crop Identification Technology Assessment for Remote Sensing (CITARS) projects have also been conducted to demonstrate the capabilities of RS for crop inventory and forecasting (MacDonald, 1984; Blaes, 2005).

Vegetation types can be characterized using their seasonal variations in the Normalized Difference Vegetation Index (NDVI) time-series, which include a series of images, acquired on weekly or decadal basis and showing the crop development dynamics. For example, the winter wheat phenophases, such as tillering and flowering as well as harvest, can be successfully identified using sensors with different spatial resolution in various band combinations and severe ground surveys, including collecting information for defining training samples for the supervised classification (Townshend et al. 1991). A number of different methods have been developed during the last two decades to discriminate crop types using NDVI and data from the Advanced Very High-Resolution Radiometer (AVHRR). These methods employ a variety of different approaches including temporal profiles of crop phenology manifested in the NDVI (DeFries et al. 1995; Reed et al. 1994), and classification of multi-temporal data (Brown et al. 1993; Loveland et al. 1995), which can be applied on differently managed crop areas worldwide.

Crop identification during the growing season is a major challenge for forecasting crop production as well as for controlling area-based subsidies in the European Union member states (Blaes, 2005). The basis for separation one crop from another is the supposition that each crop species has a unique visual appearance and spectral signature on the image. However, separating these species may be difficult because of variations in soil properties, fertilization, pest conditions, irrigation practices, planting dates, as well as intercropping, and tillage practices (Ryerson et al. 1997), all of which can be adopted in precision farming using high quality satellite images. Thus, high-resolution satellite images are the key to the above mentioned difficulties.

The purpose of this case study is to investigate the possibilities of mapping crop condition using HR satellite images for a test site in North-East Bulgaria, and it includes the following tasks:

(1) Applying arable mask from CORINE 2006 land-cover database;

(2) Conducting per-pixel supervised classification using the maximum likelihood classifier (MLC) algorithm for crop identification;

(3) Applying accuracy assessment tool in ERDAS Imagine and deriving accuracy totals and Kappa statistics;

(4) Mapping crop condition using NDVI, RDVI and SAVI vegetation indices.

2. Materials and methods

The study area – part of Zhiten test site is situated in North-East Bulgaria. The area represents intensively cultivated area sowed mostly with cereals and sunflower. This territory is one of the main agricultural regions of the country. The area is part of the European-continental climatic province of the temperate climatic belt. Climate is moderately warm with no distinctive dry season. Mean annual air temperature is 10.2 °C. The main soil types are chernozems from the zonal ones and fluvisols from the azonal ones.

The major cultivated winter crops (wheat and oilseed rape) and spring crops (sunflower and maize) were investigated in the present case study.

During the 2010–2011 agricultural season and in particular in the period between March–July 2011 four exhaustive field surveys were carried out and ground data was collected and organized in a GIS geodatabase. Field data was collected in the framework of a project financed by the Belgian Federal Science Policy Office (BELSPO) under the PROBA-V Preparatory Programme, with acronym – PROAGROBURO (Roumenina et al. 2013). The ground-truth data consists of descriptions of the LU/LC types, phenological stages and vegetation cover of crops, GPS measurements, and photos. The collected ground data will contribute of selecting appropriate training samples for the supervised classification on the chosen satellite images. Two satellite images were used in this study: a WorldView-1 panchromatic satellite image with 0.50 m spatial resolution, acquired on 30/11/2011 and QuickBird-2 multispectral (2.4 m spatial resolution) and panchromatic image (with 0.60 m spatial resolution), acquired on 31/05/2009.

The most commonly used RS vegetation index for agricultural applications is the NDVI, expressed by the following formula: $NDVI = (NIR-VIS)/(NIR+VIS)$, where VIS and NIR stands for the spectral reflectance measurements acquired in the visible red and near-infrared regions, respectively (Rouse et al. 1973). NDVI is commonly used measure for the amount of green vegetation. It ranges typically from 0.15 (bare soils) to 0.80 (dense vegetation). Additionally, the Renormalized Difference Vegetation Index (RDVI), expressed by the following formula: $RDVI = (NIR-RED)/\sqrt{(NIR+RED)}$ (Rougean and Breon, 1995) and Soil Adjusted

Vegetation Index (SAVI), expressed by the following formula: $SAVI = NIR-RED/NIR+RED+L * (1+L)$, where L is a constant value equal to 0.5 (Huete, 1988).

An arable land mask using CORINE data was applied on the QuickBird-2 and the WorldView-1 images in order to classify only the arable land and reduce the occurrence of mixed pixels with other non-arable classes.

The *k*-mean and Iterative Self-Organizing Data Analysis (ISODATA) clustering algorithms are the most frequently used ones in RS. The ISODATA algorithm was selected in this study because it allows different number of clusters, while the *k*-mean algorithm assumes that the number of clusters is known a priori (Groom et al. 1996; Garcia-Consuerga and Cisneros, 1999; Yang et al. 1999). Unsupervised ISODATA classification with five classes was applied to spectraly discriminate the crops and to collect the necessary information in order to delineate the training samples for the supervised per-pixel classification. Per-pixel supervised classification using the Maximum Likelihood Classifier (MLC) algorithm was applied on the arable territories of the test site for both images for crop identification purposes. In the MLC procedure, at least 10–15 independent training cases per class were used, so that its mean and variance can be estimated. Around 160–170 randomly distributed points were used for accuracy assessment for both classified images. The multispectral QuickBird-2 satellite image and the derived NDVI, RDVI, and SAVI vegetation indices were used to map crop condition.

3. Results and discussions

3.1. Applying arable mask from CORINE 2006 land-cover database

An arable land mask using CORINE 2006 land-cover data was applied on the QuickBird-2 and the WorldView-1 images in order to classify only the arable land and reduce the occurrence of mixed pixels. In Fig. 1 all the land cover classes present in the test area are shown and ‘2.1.1. Non-irrigated arable land’ class was used to build the mask layer.

3.2 Conducting per-pixel supervised classification using the maximum likelihood classifier algorithm for crop identification

The crop identification process was accomplished firstly by conducting unsupervised classification (using ISODATA algorithm) with 4-5 classes/clusters for both the multispectral QuickBird-2 and panchromatic WorldView-1 images. This spectral information was used together with the ground data as an indicator where to draw training samples for the supervised classification.

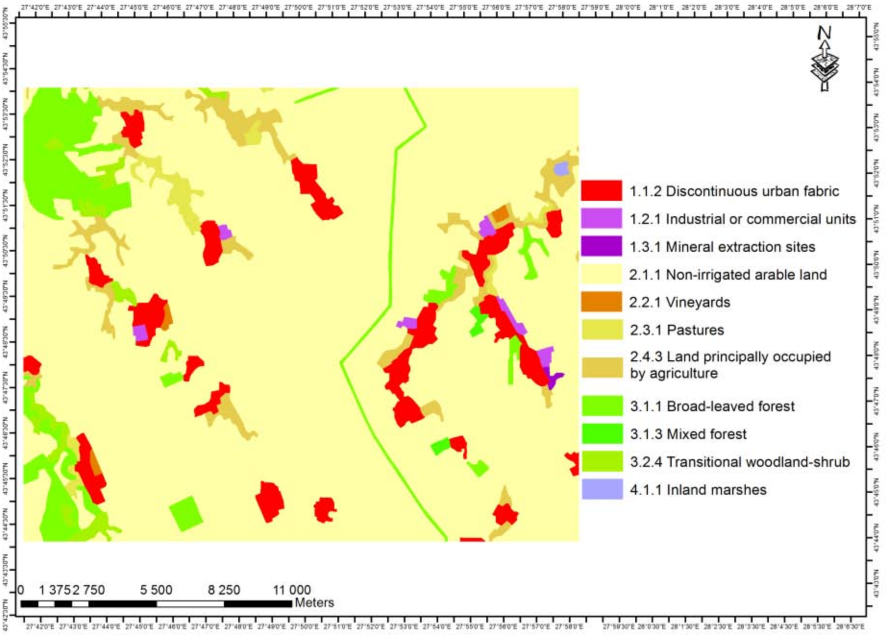

Fig. 1. CORINE 2006 land cover classes

The unsupervised classification is traditionally the first step and is accommodating the interpretation of the images. Supervised classification using the Maximum Likelihood Classifier (MLC) algorithm was applied to the arable land images. In the MLC procedure, a key concern is to collect a training set comprising of at least 10–30 independent training cases per class per discriminatory variable (e.g. band) to allow the formation of a representative description of the class, so that its mean and variance can be reasonably estimated (Piper, 1992). For example, the spectral response of an agricultural crop class in an image might vary as a function of variables such as: the crops growth stage, topographic position, density of vegetation cover and health, impact of management activities, substrate conditions, and instrument view angle (Foody, 2002). The gathered training set from the field data was good enough to make representative training samples for the arable land classes. The unsupervised classification in combination with the ground information and the derived NDVI image helped to choose and delineate appropriate training samples for the supervised classification of the QuickBird-2 image. The investigated phenological stages based on the image acquisition dates are: flowering and grain filling phenophases for winter crops and vegetative phase for spring crops for the QuickBird-2 image and emergence phenophase for winter crops for the Worldview-1 image.

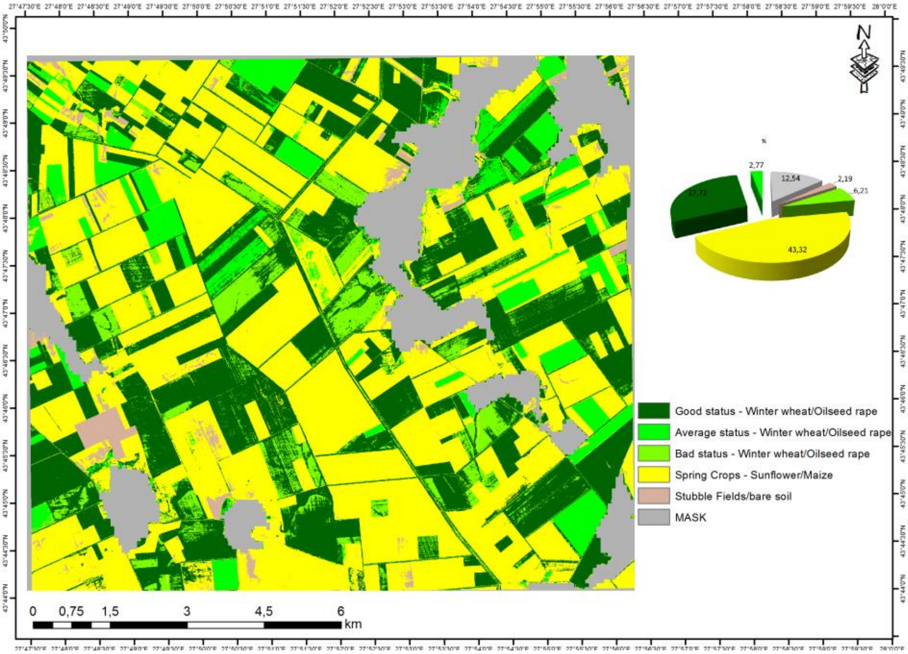

Fig. 2. Per-pixel supervised classification of QuickBird-2 satellite image

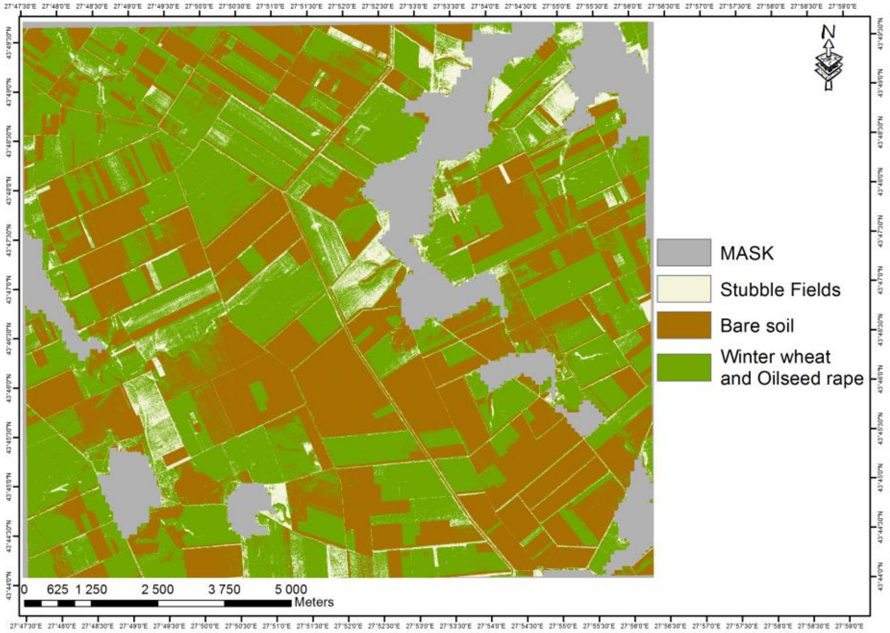

Fig. 3. Per-pixel supervised classification of WorldView-1 satellite image

The identified classes and their distribution in percentage for the QuickBird-2 satellite image are: good status - winter crops (wheat and oilseed rape – 27.72 %),) average status - winter crops (wheat and oilseed rape – 2.77 %); bad status - winter crops (wheat and oilseed rape – 6.21 %); stubble fields/bare soil – 2.19 % and spring crops – sunflower and maize – 43.32 % (Fig. 2), while for the Worldview-1 satellite image are: winter crops (wheat and oilseed rape) class; bare soil and stubble fields classes (Fig. 3).

3.3. Applying accuracy assessment tool in ERDAS Imagine and deriving accuracy totals and Kappa statistics

Accuracy assessment tool in ERDAS Imagine software was utilized for assessing the accuracy of the per-pixel classified images of QuickBird-2 (Fig. 4) and WorldView-1 (Fig. 5.). Around 160–170 randomly distributed points were assessed for both classified images. Accuracy assessment was applied on the WorldView-1 classified image for crop identification using its high spatial resolution by applying visual interpretation on the panchromatic and both on the unsupervised and supervised classifications in combination with the ground data.

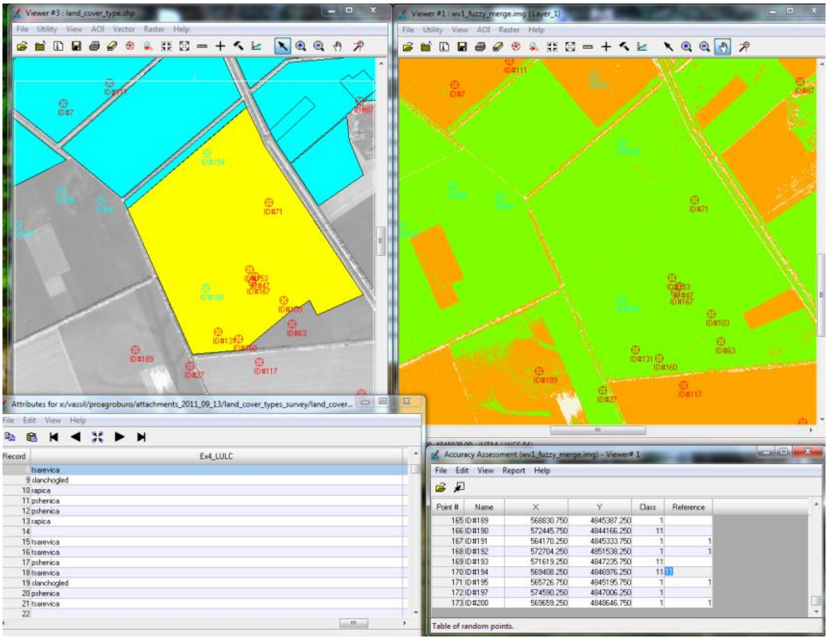

Record	Ex4_LULC
	tsarevica
9	slanchogled
10	rapica
11	pshenica
12	pshenica
13	rapica
14	
15	tsarevica
16	tsarevica
17	pshenica
18	tsarevica
19	slanchogled
20	pshenica
21	tsarevica
22	

Point #	Name	X	Y	Class	Reference
165	ID#189	568830.750	4845387.250	1	
166	ID#190	572445.750	4844166.250	11	
167	ID#191	564170.250	4845333.750	1	1
168	ID#192	572704.250	4851538.250	1	1
169	ID#193	571619.250	4847235.750	11	
170	ID#194	569408.250	4846976.250	11	11
171	ID#195	565726.750	4845195.750	1	1
172	ID#197	574590.250	4847006.250	1	
173	ID#200	569659.250	4848646.750	1	1

Table of random points.

Fig. 4. Accuracy assessment on WorldView-1 image

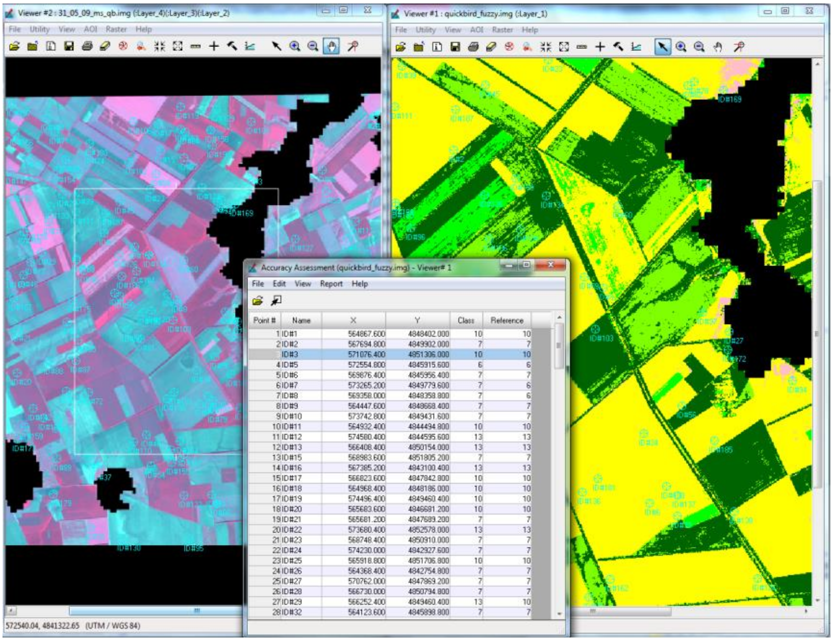

Point #	Name	X	Y	Class	Reference
1	ID#1	564867.600	4848402.000	10	10
2	ID#2	567694.800	4849902.000	7	7
	ID#3	571076.400	4851306.000	10	10
4	ID#5	572554.800	4845915.600	6	6
5	ID#6	569876.400	4845956.400	7	7
6	ID#7	573265.200	4849779.600	7	6
7	ID#8	569358.000	4848358.800	7	6
8	ID#9	564447.600	4848668.400	7	7
9	ID#10	573742.800	4849431.600	7	7
10	ID#11	564932.400	4844494.800	10	10
11	ID#12	574580.400	4844595.600	13	13
12	ID#13	566408.400	4850154.000	13	13
13	ID#15	568983.600	4851805.200	7	7
14	ID#16	567385.200	4843100.400	13	13
15	ID#17	566823.600	4847842.800	10	10
16	ID#18	564968.400	4848186.000	10	10
17	ID#19	574496.400	4849460.400	10	10
18	ID#20	565683.600	4846681.200	10	10
19	ID#21	565681.200	4847689.200	7	7
20	ID#22	573680.400	4852578.000	13	13
21	ID#23	568748.400	4850910.000	7	7
22	ID#24	574230.000	4842927.600	7	7
23	ID#25	565918.800	4851706.800	10	10
24	ID#26	564368.400	4842754.800	7	7
25	ID#27	570762.000	4847969.200	7	7
26	ID#28	566730.000	4850794.800	7	7
27	ID#29	566252.400	4849460.400	13	10
28	ID#32	564123.600	4845898.800	7	7

Fig. 5. Accuracy assessment on QuickBird-2 image

The achieved results on the overall classification accuracy for the QuickBird-2 image is 90.86 % and overall Kappa statistics is 0.8538 (Table 1), while for the WorldView-1 image is 86.71 % and overall Kappa statistics is 0.7721 (Table 2).

Table 1. Accuracy totals for QuickBird-2

Class Name	**Reference Totals**	**Classified Totals**	**Number Correct**	**Producers Accuracy (%)**	**User Accuracy (%)**
Stubble fields	6	5	5	83.33	100.00
Bad status – WC	14	8	8	57.14	100.00
Average status – WC	21	15	14	66.67	93.33
Good status - WC	44	48	42	95.45	87.50
Spring crops	90	99	90	100.00	90.91
			Overall Accuracy – 90.86%		**Kappa – 0.8538**

Table 2. Accuracy totals for WorldView-1

Class Name	**Reference Totals**	**Classified Totals**	**Number Correct**	**Producers Accuracy (%)**	**User Accuracy (%)**
Stubble fields	19	15	14	73.68	93.33
Winter crops	73	77	64	87.67	83.12
Bare soil	81	81	72	88.89	88.89
			Overall Accuracy – 86.71%		**Kappa – 0.7721**

The QuickBird-2 accuracy assessment shows that the class ‘stubble fields’ is with high accuracy, the reasons are that the class is easily identified using the multispectral data and the precise delineation of the training samples in ERDAS Imagine. The class ‘spring crops’, represented by sunflower and maize are with high users accuracy 100 %, with 90 reference points used for the accuracy assessment. The high user’s accuracy is due to the different crop development stage between winter crops and spring crops at the date of image acquisition. The accuracy assessment of the winter crops’ classes show that the ‘bad status’ class is with 100 % user’s accuracy, while average status and good status classes are with 93.33 % and 87.50 %, user’s accuracy, respectively. The accuracy assessment of the WorldView-1 satellite image shows that the ‘bare soil’ class is representing territories which are being prepared to be sown with spring crops in the agricultural year 2011-2012 or left for fallow land. The ‘winter crops’ class represents areas which have already been sown with winter crops (wheat and rapeseed) and are at emergence phenophase.

3.4. Mapping crop condition using NDVI, RDVI and SAVI indices

Mapping crop condition was accommodated using the multispectral QuickBird-2 image and the derived Normalized Difference Vegetation Index (NDVI), Renormalized Difference Vegetation Index (RDVI), and Soil Adjusted Vegetation Index (SAVI).

The raw NDVI, RDVI and SAVI indices, respectively (Fig. 6, Fig. 7, and Fig. 8) are presented by color ramp (‘no vegetation’ to ‘dense vegetation’). The highest values of the indices are for winter wheat followed by oilseed rape, sunflower, and maize cultivars. Additionally, the crop condition was mapped using the derived NDVI image and applying histogram reclassification. The crop condition status classes are the following: (1) ‘bad condition’ and (2) ‘good condition’ for winter crops and (3) ‘low NDVI values’ for the other fields, since they are already sown with early spring cultivars or left for fallow land (Fig. 9). The crop condition was analyzed using interpretation between all the indices and comparing them with the collected farmers inquires on applied agricultural practices and observed crop development stages for the agricultural fields in the test area. The SAVI shows better sensitivity for the spring crops cultivars with less than 40 % vegetation cover whereas, the NDVI gives good results for winter crops, but saturates at high vegetation densities and gives generalized results for values less than 0.40. Overall, the utilized vegetation indices show that RDVI gives crop condition assessment results for winter crops at flowering and grain filling phenophases and spring crops at vegetative phase compared to NDVI and SAVI.

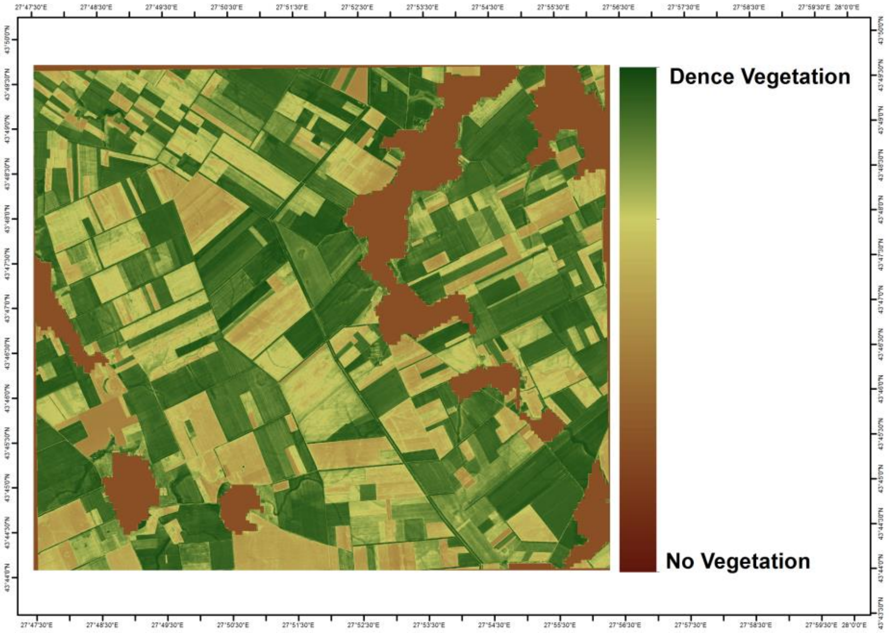

Fig. 6. NDVI image

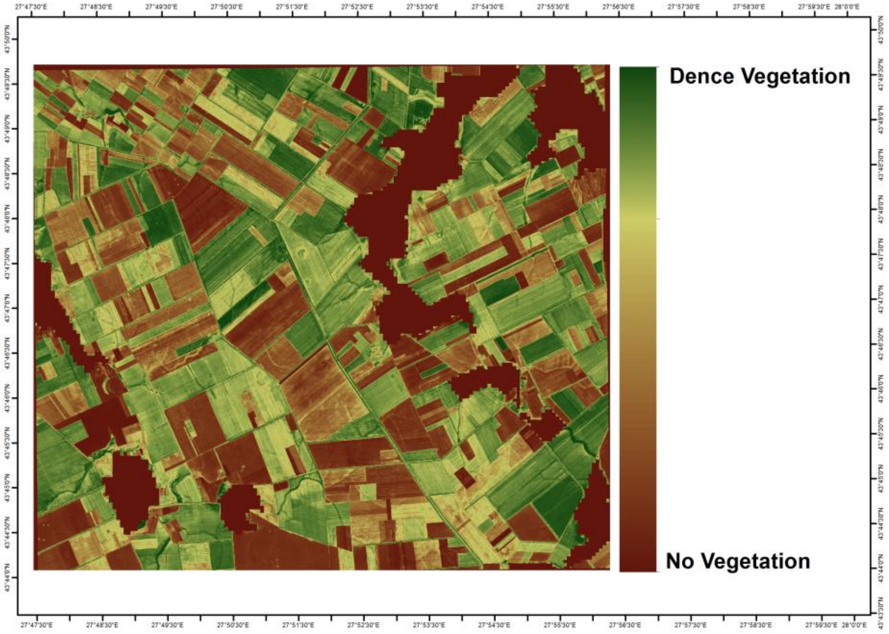

Fig. 7. RDVI image of Zhiten test area, Bulgaria

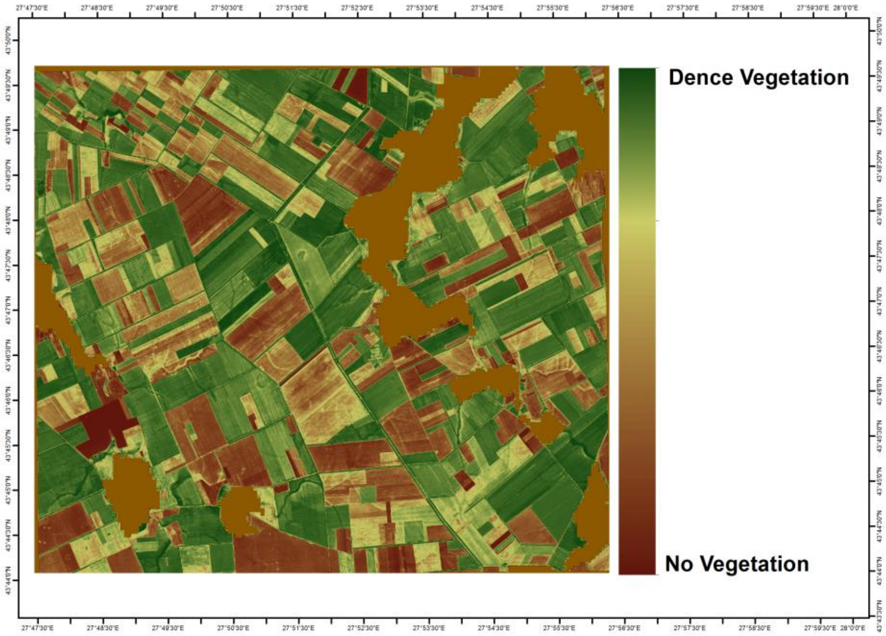

Fig. 8. SAVI image

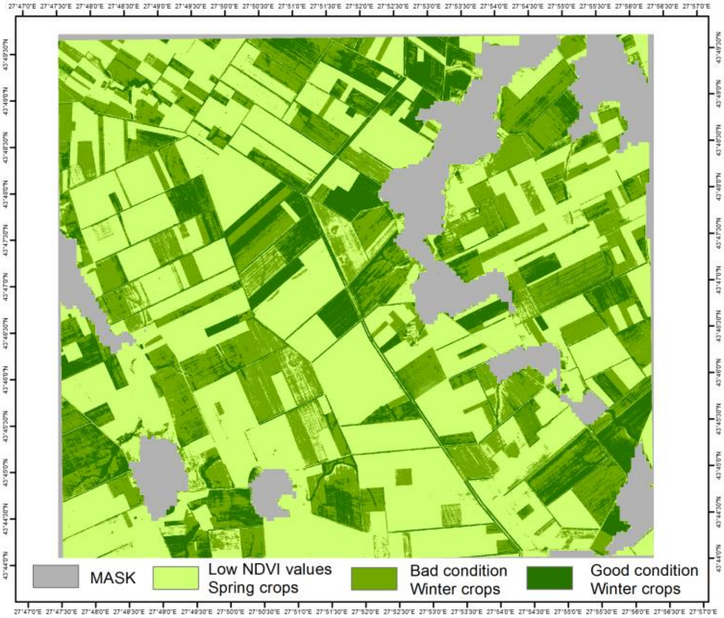

Fig. 9. Reclassified NDVI image

4. Conclusions

The presented methodology using per-pixel supervised classification for crop identification and consequently followed by utilizing the NDVI, RDVI, and SAVI indices provides a rapid tool for accurate and valuable crop condition information for a better crop management and for immediate adoption in precision farming practices. The results show that RDVI vegetation index can better be utilized for crop condition assessment at flowering and grain filling phenophases for winter cultivars and vegetative phase for spring crops compared to both NDVI and SAVI. Furthermore, in near future within the framework of the Copernicus Programme and the launch of *Sentinel-2* mission, with its more sufficient spectral capabilities, will add more possibilities for agriculture related investigations and will allow applying new spectral indices for improved retrieval of vegetation biophysical parameters.

Acknowlegments

This work would not be possible without the support of ERDAS Geospatial Challenge contest, together with DigitalGlobe and Intergraph, which granted the satellite images after accepting a paper proposal.

Refferences

1. Meyer-Roux, J., Vossen P. (1994). The first phase of the MARS project, 1988–1993: overview, methods and results. In: Official Publications of the E.U., Luxembourg (Ed.), Report EUR 15599 EN. Conference on the MARS project: Overview and prospectives, Belgirade, 1994, 33–79.
2. De Winne, P. (2004). Les Besoins de la Direction Generale VI: Agriculture. In: Office for official publications of the E.U., Luxembourg (Ed.), Report EUR 15599 EN, 2004. Conference on the MARS project: Overview and prospectives, Villa Carlotta, Belgirate, Lake Maggiore, Italy, 17–22 (in French).
3. Cohen, Y., M. Shoshany. (2002). A national knowledge-based crop recognition in Mediterranean environment International Journal of Applied Earth Observation and Geoinformation, 4, 75–87.
4. MacDonald, R. (1984). IEEE Transaction on Geoscience & Remote Sensing, GE-22, 473–481.
5. Blaes, 2005. Efficiency of crop identification based on optical and SAR image time series. Remote Sensing of Environment, 96 352–365.
6. Townshend, J., Justice C., Li W., Gurney C., McManus J. (1991). Global land cover classification by remote sensing: present capabilities and future possibilities. Remote Sens Environ, 35, 243–255.
7. DeFries, R., Hansen M., Townshend J. (1995). Global discrimination of land cover types from metrics derived from AVHRR pathfinder data. Remote Sens Environ, 64 (3), 209–222.

8. Reed, B. C., Brown J. F., VanderZee D., Loveland T. R., Merchant J. W., Ohlen D. O. (1994). Measuring phenological variability from satellite imagery. Journal of Vegetation Science, 5, 703–714.
9. Brown, J. F., Loveland T. R., Merchant J. W., Reed B. C., Ohlen D. O. (1993). Using multisource data in global land-cover characterization: Concepts, requirements, and methods. Photogramm Eng Remote Sens, 59(6), 977–987.
10. Loveland, T. R., Merchant J. W., Brown J. F., Ohlen D. O., Reed B. C., Olson P., Hutchinson J. (1995). Seasonal land-cover regions of the United States. Annals of the Association of American Geographers, 85, 339–355.
11. Ryerson, R. A., Curran P. J., Stephens P. R. (1997). Agriculture. In: Philipson W.R. (Ed.) Manual of Photographic Interpretation. 2nd ed. Americal Society for Photogrammetry and Remote Sensing, Bethesda, MD, 365–397.
12. Roumenina, E., Kazandjiev V., Dimitrov P., Filchev L., Vassilev V., Jelev G., Georgieva V., Lukarski H. (2013). Validation of LAI and assessment of winter wheat status using spectral data and vegetation indices from SPOT VEGETATION and simulated PROBA-V images. Int J Remote Sens, 34(8), 2888–2904.
13. Rouse, J., Haas R., Schell J., Deering D. (1973). Monitoring vegetation systems in the Great Plains with ERTS. In: Third ERTS Symposium, 1973, NASA SP-351 I, 309–317.
14. Rougean, J. L., and Breon, F. M. (1995). Estimating PAR absorbed by vegetation from bidirectional reflectance measurements. Remote Sens. Environ., 51, 375–384.
15. Huete, A. R. (1988). A soil vegetation adjusted index (SAVI). Remote Sens. Environ., 25, 295–309.
16. Groom, B. G., Fuller R. M., Jones A. R. (1996). Contextual correction: techniques for improving land-cover from remotely sensed images. Int J Remote Sens, 17, 69–89.
17. Garcıa-Consuegra, J., Cisneros G. (1999). Establishing spatially continuous in a non-supervised way. In: Proceedings of the IEEE International Geoscience and Remote Sensing Symposium (IGARSS’99), 1999, Hamburg, Germany.
18. Yang, H., Khorram, S., Dai X.L. (1999). Applications of simulated annealing minimization technique to unsupervised classification of remotely sensed data. In: Proceedings of the IEEE International Geoscience and Remote Sensing Symposium (IGARSS’99), 1999, Hamburg, Germany.
19. Piper, J. (1992). Variability and bias in experimentally measured classifier error rates. Pattern Recognition Letters, 13, 685–692.
20. Foody, G. M., (2002). Status of land cover classification accuracy assessment. Remote Sens. Environ. 80, 185–201.

КАРТОГРАФИРАНЕ НА СЪСТОЯНИЕТО НА ЗЕМЕДЕЛСКИ КУЛТУРИ ПО СПЪТНИКОВИ ИЗОБРАЖЕНИЯ И ПРОДУКТИ ОТ QUICKBIRD-2 И WORLDVIEW-1. ТОЧНО ЗЕМЕДЕЛИЕ ВЪРХУ ЧАСТ ОТ ТЕСТОВИ УЧАСТЪК ЖИТЕН, РАЗПОЛОЖЕН В СЕВЕРОИЗТОЧНА БЪЛГАРИЯ

В. Василев, Е. Руменина

Резюме

Целта на настоящата статия е да изследва потенциала и възможностите на картографирането на състоянието на земеделски култури по спътникови изображения с висока пространствена разделителна способност върху тестови участък Житен, разположен в Североизточна България. Избрани са спътникови изображения от QuickBird-2 и WorldView-1, заснети съответно на 31.05.2009 г. и 30.11.2011 г. Методологията включва следните работни етапи: 1) Прилагане на маска от CORINE 2006 земно покритие; 2) Извършване на пикселно-ориентирана контролирана класификация по метода на максимално подобие за разпознаване на земеделски култури; 3) Прилагане на инструмент за оценка на точността на класификациите и извличане на обща точност и Капа статистика; 4) Картографиране на състоянието на земеделските култури по генерирани индексни изображения Normalized Difference Vegetation index (NDVI), Renormalized Difference Vegetation Index (RDVI) и Soil Adjusted Vegetation Index (SAVI). Общата точност на изображението от QuickBird-2 е 90.86% и с Капа статистика от 0.8538, докато това на WorldView-1 има обща точност от 86.71% и с Капа статистика от 0.7721. SAVI индекса показва по-добра чувствителност към пролетните култури с общо площно покритие от под 40%. От друга страна NDVI индекса дава по-добри резултати при картографиране на зимните култури, но индекса се насища при високи стойности и гъста растителна покривка. Освен това NDVI индекса дава ниска информативност при стойности по-ниски от 0.40. RDVI индекса дава добри резултати при картографиране на зимните култури при изкласяване и наливане на зърно фенофазите, както и при фазата образуване на съцветия при пролетните култури сравнено с индексите NDVI и SAVI.

Bulgarian Academy of Sciences. Space Research and Technology Institute.
Aerospace Research in Bulgaria. 27, 2015, Sofia

METAL DETECTORS AND PHYSICS EDUCATION

Georgi Golemshinski

Sofia University
e-mail: gngolem6@abv.bg

Abstract

Metal detector equipment has become a profound and ubiquitous geophysical device class widely available not only to scientists, but to general public, hobbyists, recreational enthusiasts and sport addicts alike. Handheld metal detectors are by no doubt the most widespread geophysical apparatus existing. Models range from simple toy-like inexpensive models to extremely sophisticated computerized systems with plenty of features and modes of operation.

The use of metal detectors during the years has found applications such as military demining operations, archaeology, treasure hunting, mineral analysis, ground infrastructure surveying, etc. But being such an elaborate instrument, the metal detector has ever been neglected for its potential as a mobile handheld physics educational laboratory that is capable of showing to students at schools and universities many physical phenomena concerning electricity and electromagnetism, radio-electronics, soil and rock properties, water and mineral properties, microprocessors and computer technologies and even astronomy.

The present publication strives to disclose those hidden capabilities of metal detectors to the reader and concentrate the physics teacher attention to the metal detector avenue as being a fruitful laboratory for tutoring many branches of physics in a pleasant and involving way to the young and not only the young generation.

1. Introduction

Metal detectors are geophysical devices and as such exhibit a number of physical phenomena to the observer. With this regard, they incorporate systems that utilize physical properties of the ground substances and construction materials in order to extract information about the objects that are underneath or to study the ground, soil, rock, water, concrete, or other material properties.

Metal detectors utilize various physics laws and areas such as electromagnetism, acoustics, ionizing radiation, etc. However, ubiquitous are those instruments that use electromagnetic properties of objects. These metal detectors are the ground penetrating radar, the pulse induction detectors and the induction balance detectors. Of the most widespread kind are the latter, due to their moderate cost, moderate weight and lowest power consumption. Being handheld devices low power consumption directly translates into cheaper and lightweight batteries.

The affordability of the induction balance metal detectors accompanied with their discrimination properties between ferrous and non-ferrous metals make them most suitable to use for teaching physics to students and pupils at schools and universities.

However, before we continue with the concrete implementation of the metal detectors in teaching physics we should make a brief retrospection of the metal detector development milestones and reveal to the reader its invention and refinement history.

2. Brief history of metal detectors

The first metal detector is assumed to be the Alpha (see Fig. 1). It was used for finding unexploded bombs right after World War I (WWI). M. Guitton who was a professor of physics at Nancy invented it in France. It used the principle of inductive balance – a method and circuit invented in 1879 by British scientist David Hughes (Honoré, 1919).

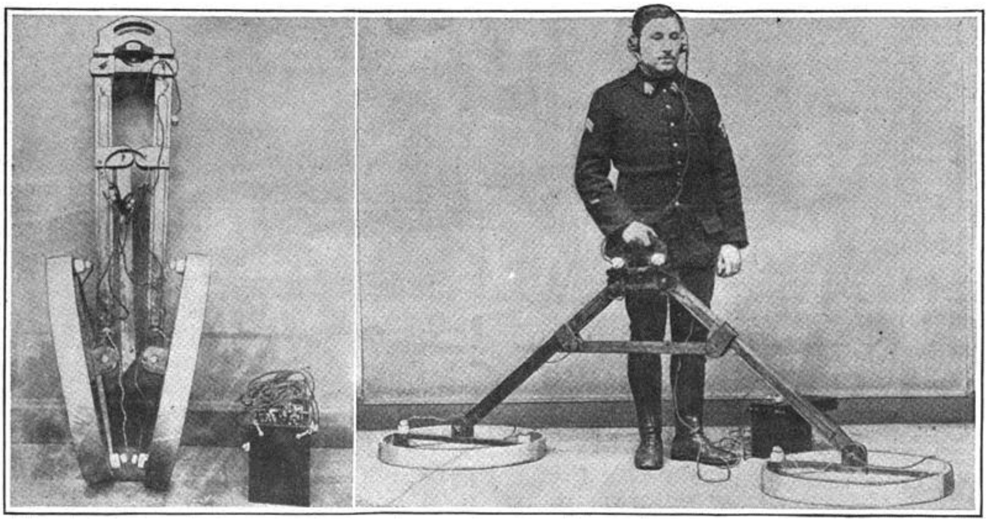

Fig. 1. "Alpha" metal detector. Invented immediately after WWI in France by M. Guitton

First metal detectors were used for discovering artillery shells, mines and other military ammunition that was buried underground and was dangerous for the trespassers. Thus, during the years between the World Wars work continued on refining the designs and making them more sensitive and lightweight. One of the first models to resemble modern handheld metal detectors and to be comparable with them, in terms of sensitivity and functionality, is the Polish mine detector 'Mark I' (see Fig. 2). It was a metal detector for searching of landmines and was developed during the Second World War (WWII). After Germany invaded Poland in 1939 and occupied France in 1940, work on the detector was interrupted and was restarted in the winter of 1941–1942. The inventor of this modern detector was Polish lieutenant Józef Kosacki.

Fig. 2. Mine detector Mark I used by sappers of the Royal Engineers corps, North Africa, 28 August 1942

The Polish detector was of the induction balance type. It had two coils in balance – one transmitting and one receiving. Once an object was in vicinity, it disturbed the induction balance and induced alternating acoustic magnetic field in the receiving coil. The latter was connected to headphones and sound was heard.

The stronger the sound, the larger or the closer the object was. The whole apparatus weighted around 30 pounds (14 kg) (Croll, 1998). During the Second World War several hundred thousand of detectors were produced. The British Army used this type of detector until 1995 (Modelski, 1986).

3. Modern metal detectors

One of the early inventors of modern metal detectors is Shirl Herr. In August 1929 Benito Mussolini used his devices in an expedition for finding remaining structures and archaeological artefacts from the Emperor Caligula's galleys at the bottom of Lake Nemi, Italy.

Another early inventor is Gerhard Fisher. He developed a radio direction-finding system for accurate navigation. During testing of the system, which was very successful, Fisher observed that there were errors in navigation in areas where ore-bearing rocks were present. He continued developments in this regard by the clue that metallic objects or substances containing metals distort radio beams. In 1925 Fisher became the first person to be granted a patent for metal detector. Today there are a large number of companies that offer sophisticated metal detectors to the market.

Fig. 3. Modern handheld metal detectors implement microprocessors and LCD display

With the invention of the bipolar transistor in the fifties, metal detectors became much smaller, lighter and cheaper. Modern high-end models are microprocessor controlled (Fig 3). In addition, a non-sinusoidal transmitting frequency is often used. This method is called multi-frequency mode of operation. It enhances the identification and discrimination properties of the detector allowing the discovery of landmines that contain small amounts of metal (Fig. 4).

Fig. 4. US military are using modern metal detectors to discover landmines

4. Physics education using metal detectors

It has been proven, through many experiments and inventions, that physics education strongly benefits from e-learning methods such as utilizing computer aided simulations (Zabunov et al., 2013, Zabunov, 2010, Zabunov, 2004). It is a fact that modern and attractive technologies such as computers always do draw the young people to the tutoring process. Another fruitful approach, for raising interest in physics among students, is demonstrating physical phenomena by the means of metal detectors. The latter are popular and attractive electronic devices that are thrilling to use and handle due to their inherent area of application – the treasure hunting.

Physics education using metal detectors may be performed either in the laboratory or in the field. Using a metal detector in a laboratory setting will enable the teacher to show how a metal detector finds a metal object hidden under the clothes or in the hand. Using discrimination mode the tutor is able to demonstrate to students the ability of the induction balance metal detector to discriminate between metal types, i.e. to find out if a metal object is ferromagnetic or non-ferromagnetic. Furthermore, using the discrimination mode, the nature of ferromagnetic and non-ferromagnetic metal detection may be demonstrated. For example the teacher may hide a ferromagnetic object (a nail) inside a non-ferromagnetic box (aluminium box). The box will shield the ferromagnetic properties of the objects inside. Due to the eddy currents induced in the box walls and the skin effect that prevents the currents to penetrate inside the box the metal detector will recognize a non-ferromagnetic object.

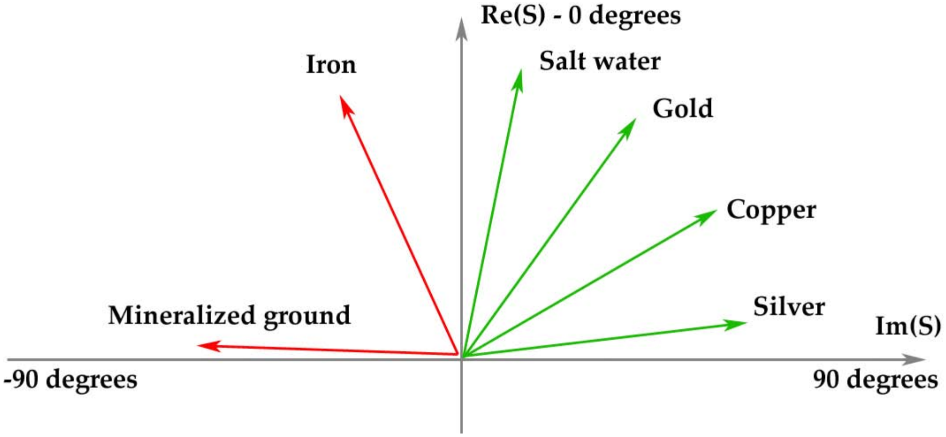

Fig. 5. Resultant magnetic field phase shift for different metals and substances

Discrimination with induction balance technology is possible due to two physical phenomena – ferromagnetic metal magnetization and non-ferromagnetic metal eddy current development. These two phenomena are observed under alternating magnetic field. The field magnetizes the metal on each alternation if the metal is ferromagnetic. Thus the resulting magnetic field has a lag in its phase. On the other hand a non-ferromagnetic metal will not magnetize and will not produce a lag in the resulting magnetic field but due to its conductance it will develop eddy currents on its surface. These eddy currents on their own will develop magnetic field but this time with the opposite phase shift. Thus, the resulting magnetic field will have positive phase compared to the transmitted signal (Fig. 5).

The detection of ferromagnetic metals is not determined by metal electrical conduction thus non-conducting metal materials such as ferrite are easily detected.

If the teaching process is to be performed in the open for field demonstrations, a large number of exercises are possible. One physical phenomenon, that is interesting to students, is the ferromagnetic properties of soils – a mineralized soil will register with a very strong signal as iron or rather as ferrite on the metal detector. This phenomenon prevents metal detectors to work in discrimination mode over ferrous soils and the so-called ground balance procedure should be carried out either automatically or manually depending on the metal detector type.

If the soil is non-ferromagnetic, for example most sandy soils, discrimination mode will be permitted. Furthermore, if the soil is soaked with salt water another phenomenon will appear. The metal detector will register a strong signal on the discrimination mode as if the object were neutral metal with properties in between ferrous and non-ferrous metals (Fig. 5). Such ground conditions allow working in discrimination mode. One could encounter salt water in the ground on sea shores and beaches.

A large number of different objects may be buried in the ground at shallow depths in order to demonstrate how their physical properties allow the metal detector to discover them and discriminate one object from another. The orientation of the buried object also matters. For example, a coin placed horizontally will reflect stronger signal than if it were placed vertically due to the eddy currents which tend to flow in the horizontal plane. Another example is a large ferromagnetic object with wide surface. These objects react as if they were non-ferromagnetic, because the eddy currents, in the surface of the object, prevail over their ferromagnetic properties and effectively shield the inner-part of the object to the alternating magnetic field. On the other hand, if we try to locate a large object of non-ferromagnetic material consisting of a large number of small pieces such as many 100 small coins, we would be surprised to discover that the signal is not as strong as anticipated. The eddy currents will be blocked by the fragmentation of the material under examination and the signal will be diminished. This principle of fragmentation is used in transformers and ferrite coil cores were the magnetic core is fragmented either to small pieces like grit (ferrite) or to thin plates.

Lastly, the metal detector may be used as an astronomical tool. One could discover meteorites in the soil using a metal detector. Most meteorites contain metals of which iron is prevalent. Thus, meteorites register as iron objects with a discriminating metal detector.

6. Conclusions

The utilization of metal detectors as an attractive tool for teaching physics at schools and universities is yet to be implemented. A team at Sofia University, Bulgaria, is planning to utilize metal detectors in tutoring courses both to raise interest in physics among pupils and to increase students understanding of complex electromagnetic processes, which would help their successful graduation in physics and engineering subjects.

References

1. Honoré, F. (1919). Locating unexploded shells on the battlefields of France, Scientific American Publishing Co., New York, Vol. 120, No. 16, 395.
2. Croll, M. The History of Landmines, Leo Cooper, Pen & Sword Books Ltd., Great Britain, 1998, ISBN 0-85052-628-0
3. Modelski, T. The Polish contribution to the ultimate allied victory in the Second World War, Worthing, England, 1986, p. 221.
4. Zabunov, S. and Gaydarova, M., Rotating the flying disc in a stereo 3D simulation, Latin American Journal of Physics Education 7, pp. 192–195 (2013).
5. Zabunov, S. (2010). Rigid body motion in stereo 3D simulation, European Journal of Physics 31 (6), 1345–1352.
6. Zabunov, S., (2004). A Language for Describing the Generating Structure of the Educational Material in the Individually Adaptive Learning Management System, In: International Conference on Computer Systems and Technologies - CompSysTech’2004, Rousse, Bulgaria, 17-18 June, 2004.

МЕТАЛОТЪРСАЧИТЕ В ОБУЧЕНИЕТО ПО ФИЗИКА

Г. Големшински

Резюме

Метал-детекторите се превърнаха в ефективен и широко разпространен геофизически уред, достъпен не само за учените, но и за любителите, ентусиастите и други групи от обществото. Преносимите металотърсачи са несъмнено най-често срещаните геофизически инструменти. Моделите са разнообразни – от прости уреди, подобни на играчки, до особено сложни компютъризирани системи с много функции и режими на работа.

Металотърсачите през годините са използвани в отбранителната дейност при търсене на мини, в археологията при откриването на съкровища, в геологията при анализ на минерали, проучване на подземни инфраструктури и др., но въпреки своята широка гама от възможности, металотърсачът е неглижиран по отношение на функцията си, като мобилна лаборатория за изучаване на физични явления. Метал-детекторите са способни да демонстрират на учениците и студентите множество явления, свързани с електромагнетизма, радио-електрониката, свойствата на скалите и почвите, водата, минералите т.н. Металотърсачите са също подходящи за изучаване на микропроцесорни системи и даже астрономия – с помощта на металотърсачи могат да се откриват метеорити.

Настоящата публикация се опитва да разкрие тези непознати възможности на метал-детекторите и да привлече вниманието на учителите по физика към областта на преносимите геофизични инструменти, като ефективна лаборатория за изучаване на физиката по приятен и завладяващ начин.

Bulgarian Academy of Sciences. Space Research and Technology Institute.
Aerospace Research in Bulgaria. 27, 2015, Sofia

Hypotheses

ON FUNDAMENTAL CONSTANTS OF THE UNIVERSE

Velko Velkov

e- mail: velvel@mail.bg

Abstract

The report includes analysis about constancy of the fundamental physical constants – gravity, relativity and quantum. It presents the reason about the change of their values during the evolution of the Universe.

One of the possible development directions of modern physical science is associated with the creation of a quantum theory of gravity by which to achieve the unification of the gravitational interaction with the other three types of interaction - strong and weak nuclear forces and the electromagnetic interaction, united in the so-called "Standard Model". According to the author of one of the most serious books on Cosmology [1], there is no more universal theory than the General Theory of Relativity. However, if such a theory would be built in future, stated he, three known cosmic constants should be set at its foundation: the gravitational or Newton's constant, marked in most sources through **G**, the relativistic or Einstein's constant (**c)** and the quantum or Planck's constant (**h**). Unfortunately, such a general theory has not yet been created, despite the efforts of modern physical science and a number of leading scientists in the creation of "Theory of Everything", "Grand Unification", "Superstring theory" and other ambitious exertions.

The values of the specified constants, determined as “fundamental” in the measurement system CGS have the following meanings:

- $2{,}97.10^{10}$ cm/s – for the speed of electromagnetic interaction, in particular of the light, **c;**
- $6{,}68.10^{-8}$ $cm^3/g.s^2$ – for the gravitational constant of Newton **G;**
- $6{,}67.10^{-27}$ erg.s – for the Planck's constant (**h**).

From the combination of these three constants in physics other fundamental basic physical values and parameters are derived, such as **density**, elementary or Planck **length**, the characteristic **time** and elementary **mass**, assuming that accordingly they are unchangeable and of constant values. Using the formulas, presented in [1], p. 170 to calculate them, the following meanings are obtained of the specified physical values:

- 5.10^{-93} g/cm^3 – for the density;
- $1{,}6.10^{-33}$ cm – for the elementary or Planck length;
- $0{,}5.10^{-43}$ s – for the characteristic or Planck time;
- 2.10^{-5} g – for the “graviton” mass.

It should be noted that two of these parameters and values, namely, the density and the time associated with the supposed Big Bang, laid by one of the directions in modern science the beginning of the Universe. This study and publication is not intended, but through their formulations wavered in a sense, the foundations of the theory and everything related to the Big Bang.

The values obtained for the specified physical quantities seem to be paradoxical - enormous or too small, but there can be no doubt that they reflect deeply embedded in the structure of the Universe ratios and proportions of the structuring and interaction. It is indicative for example, the connection or rather the ratio between the masses and dimensions of elementary particles, in particular protons and electrons and the average masses and sizes of large configurations, the Sun and the planets [2], p. 41-42, and many others ratios and proportions, shown for example in [3], [4]. In these ratios and proportions, and the analytical expressions for the calculation of almost all physical quantities, invariably present the fundamental or cosmic constants. That is why the question of their consistency over time, or during the process of the Universe evolution is interesting from a scientific and philosophical point of view because there is decisive importance for building a complete and comprehensive picture and outlook for the structure and processes in it.

Once it is obvious in view of the processes of the world around and the completed knowledge that everything in there changes over time, due to some, generally speaking, development, the question logically arises concerning the possibility of the of physical quantities and parameters availability of specified over the time values, as these considered as fundamental constants. In this respect, two publications [5] and [6] develop the idea and propose the hypothesis of the existence in the Universal space of fundamental physical Essence, as a basis and source of all structures and processes. In the first article the basic physical parameters of this Essence have been defined and their values have been calculated. Furthermore, the ability of changing their values over time was grounded, as a result of the objective development of the basic cosmological cycle of the Universe.

Consistent analysis on the question of the constancy of the three basic constants in the merger of the information from the known works into a single information massif leads to the following conclusions and findings. The gravitational constant of Newton **G,** as shown in [5] by its dimensions, it reflects a specific volume, or volume assigned to the unit of mass, filling this volume, i.e. the reciprocal of density. On this basis, it was calculated the density of the occupying the universal space physical content, termed “Essence”. The resulting value is in the range of $1{,}49.10^7$ g/cm^3. According to the hypothesis of [5], the density of this Essence is variable over time, due to the fact that it is given rise to the structures of substance as we know about, the particles, through a process of "condensing" or compacting the masses from the Essence into discrete volumes.

In [6] it is determined analytically the range of variation or dispersion of the values of the fundamental Essence's density and the average density of the substance in the course of the Universe's evolution, due to overflow of masses (energy) from the Essence to the substance and vice versa. The periodicity of this process is defined as a major cosmological cycle. Once the value of the well known and confirmed experimentally gravitational constant (**G**) in the present stage of the Universe 's evolution, then based on the determined density values during the cycle, it could be calculated also the value of the gravitational constant. It is obtained the following variation range of the gravitational constant value in the course of the Universe evolution: 10^{-5}–10^{-8} cm^3/g.s^{2,}, i.e. according to the proposed hypothesis the gravitational constant is not a steady one during the evolution, but changes slowly over time value and only for relatively short periods of time may conditionally be considered constant.

As a consequence of the change of the Essence density, i.e. the transmission medium of the different known interactions, it should be changed as well as and the value of the speed of propagation of electromagnetic oscillations or i.e. the light. If the actual values of the density of Essence as defined according to [5] are adequate, and the actual (current) velocity of the electromagnetic oscillations, denoted by the symbol **c**, as is well known is in the range 3.10^{10} cm /s, then the velocity of electromagnetic interactions in the range of possible values for the density of the Essence over time can be calculated by simple mathematical rule and should have values as follows:

- 2.10^8 cm/s- at the Essence density 10^5g/cm^3
- 2.10^9 cm/s- at the Essence density 10^6g/cm^3
- 2.10^{11} cm/s-at the Essence density 10^8g/cm^3

It turns out that in the early stages of the current cycle of the Universe circle, the speed of electromagnetic oscillations was two orders of magnitude less than the current one, and the future value will reach magnitude of an order higher. This explains or rather discourages one of the main phenomena, supporting the idea of an expanding Universe, namely infrared displacement (redshift) of the spectrum of the electromagnetic radiation. No moving apart and dispersion of the cosmic objects, but the propagation of electromagnetic oscillations in an environment with less density back in time and a correspondingly lower speed of spread is the reason for the spectrum of electromagnetic oscillations shift from distant sources to infrared area, reaching us in this era. The tendency also shows an increase in the speed of light in one order of magnitude in the future with all the consequences from this.

Since there are serious arguments and reasons to believe that at least two of the three main cosmic constants, namely (**G**) and (**c**) are time-varying values, and hence as a consequence, the above mentioned derivatives should be of variable in time values.

Proceeding also to the issue of consistency of the third fundamental constant - Planck's constant **h** should be noted here that things appear different. The studies show that one could not reveal compelling reasons or grounds for it to be considered a value of a variable meaning.

According to science, **h** appears distinctive, responsible and determining in structuring and in the processes, arising at the micro level of organization of the matter - substance and radiation, and as noted at the beginning, also indirect at macro level. Its importance in the physics of elementary particles and quantum mechanics is essential and therefore its value is determined strictly and accurately, and also the physical meaning and dimension it as a quantum of action. What can the value of **h** depend on, what other values and parameters can be connected with, can it be to such an extent independent and is really its value unchangeable. In a first approximation, it is not directly related and not associated with the physical parameters of the Essence and therefore is not subjected to the influence of other factors in the formation of its value. This conclusion may not be fair and may not yet have established a relationship of h with other physical values. Now seem to accept **h** for immutable constant value i.e. fundamental. In the absence of theoretical and experimental results on the matter, should be satisfied with the expression of some assumptions that can be used in our efforts and work on the problems of cosmology and particle physics.

In the context of the proposed hypothesis for the transformation of the fundamental Essence in substance, **h** is probably linked and influences the process of formation and synthesis of primary structures of substance by the process of condensation, leading to sampling, quantization and separation of the structures of the substance in the middle of the Essence. One of the guiding points on the way to clarify the question of the influence of **h** on the processes of the Universe is connected with the specifying whether each new cycle of universal circulation, quantization of the Essence and the structuring of the substance's component is performed at the same space (and perhaps energetic) level, or there is a difference in the space and energetic parameters of quantization from cycle to cycle.

There are only two possibilities: if **h** is actually constant, the Universe has evolved and will always develop by the same way in its cycle. While if **h** due to reasons, which are a subject to future studies, takes different values in each new cycle, then there are many possibilities for its structure and development.

References

1. Левитан, Е. П. Физика Вселенной. Изд. „Наука”, Москва, 1976.
2. Философские проблемы физики элементарных частиц. Под ред. И.В. Кузнецова и М. Э. Омельяновского. Изд. „Наука”, Москва, 1964.
3. Victor J. Stenger. A Case Against the Fine Tuning of the Cosmos. University of Colorado 500 N Bermont St Lafayette, CO 80026 USA.
4. John C. Baez. Higher-Dimensional Algebra and Planck-Scale Physics. Department of Mathematics, University of California Riverside, California 92521, USA January 28, 1999.
5. Velkov, V. Hypothesis of a Cosmological Model of the Universe without Gravitation. Aerospace Research in Bulgaria № 26, Bulgarian Academy of Sciences, Sofia, 2014.
6. Velkov, V. Basic cosmological cycle of the Universe. Aerospace Research in Bulgaria № 27. Bulgarian Academy of Sciences, Sofia, 2015.

ОТНОСНО ПОСТОЯНСТВОТО НА МИРОВИТЕ КОНСТАНТИ

В. Велков

Резюме

Докладът представя анализ относно постоянството на фундаменталните мирови константи – гравитационната, релативистката и квантовата. Представени са доводи, подкрепени с числови изрази, за промяна на стойностите на поне две от тях в процеса на еволюцията на Всемира, а именно гравитационната константа на Нютон и скоростта на електромагнитните колебания, в частност светлината. За гравитационната константа е коментиран и обоснован физическият смисъл, не като величина свързана с гравитацията, а свързано със спицифичния обем, реципрочно плътността, на основополагаща физическа същност, от която се допуска и като хипотеза е заложено, че произхожда и се формира всичко във всемирното пространство. Интерпретирана е възможността и вероятността за постоянство във времето и на третата фундаментална физическа константа – квантовата или константата на Планк.

Bulgarian Academy of Sciences. Space Research and Technology Institute.
Aerospace Research in Bulgaria. 27, 2015, Sofia

Hypotheses

BASIC COSMOLOGICAL CYCLE OF THE UNIVERSE

Velko Velkov

e- mail: velvel@mail.bg

Abstract

In the report it is presented the idea of the transformation of the fundamental physical Essence, with exactly definite parameters, in the matter and reverse.

The contemporary science determines the average density of the substance in the observed part of our Universe to a value between 10^{-29} - 10^{-30} g/cm^3 [1-3], and specifies as a "critical" the value of 10^{-28} g/cm^3. On the other hand, according to a new hypothesis, in [4] it has been presented the idea about the absence of vacuum and the gravity, and the bodies' attraction is explained, through pushing the bodies to one another as a result of the pressure exerted by a real physical Essence, filling the cosmological space. It is shown that namely this particular physical Essence, of specified physical parameters, is at the foundation, the prime cause and the source of all structures and processes in the Universe, is a prerequisite and determines them. One of the fundamental parameters of this Essence, namely the density, has been determined to the value of $1{,}5.10^7$ g/cm^3. In (4) it is also scientifically substantiated, that the substance and as a result all physical bodies are originated and structured from and under the impact of this fundamental Essence by “condensing” of the masses from the Essence into masses of the substance, from the known particles to the giant physical structures, planets, suns, galaxies. Namely, the substance's structural particles do not differ from the compacted Essence, but of a significantly greater density compared to that of the Essence, and as a result obtaining new physical properties.

The proportion between the two specified values of the density is of the order of 10^{37} or the average density of the substance in the Universe space is 10^{37} times less than the density of the Essence. Just so times, according to science, is less effective the alleged gravitational interaction compared to the electromagnetic. Is this an accidental coincidence or it is a deeply premised regularity?

If a value of the order of 10^{37} presents actually some fundamental proportion and the “critical“ or the marginal average density of the substance in the Universe, which has been determined by the contemporary science to a value of 10^{-28} g/cm^3, then the following processes' chain emerges as the most probable. From the hypothesis, presented and justified in [4] follows, that the density of the Essence and the average density of the originated substance from it, are in inverse proportional dependence i.e. the more dense is the Essence, the less is the average density of the substance and vice versa, because they are to each other a function and a consequence. This dependency and the known values for both parameters allow them to be in the first approximate analytically estimated the possible range of variation or dispersion of their values and their ratio in the process of the Universe evolution, as shown in the following table:

The Essence density, ρ_E [g/cm^3]	**The substance average density, ρ_M** [g/cm^3]	**The densities ratio**
10^8	10^{-31}	10^{39}
$1,5.10^7$	~ 10^{-30}	~ 10^{37}
10^6	10^{-29}	10^{35}
10^5	10^{-28}	10^{33}

The data at the second row refer to the values of the corresponding density and their ratio to the current period of the Universe evolution.

What hints are obtained from the table data? As far as the Essence is obviously fundamental, and the matter in all its forms of substance and radiation, a consequence and a product of the evolution of its parameters, there is a reason for admission the following chain of processes. Let assume as initial the one of the two marginal conditions, according to the table, for example the top one, at the Essence density of 10^8 g/cm^3 and the average density of the substance of 10^{-31} g/cm^3, then in this condition there is almost no substance. Whole energy, correspondingly the mass of the substance, through radiation has gone into the Essence, and its density has reached the specified value. It is probably a marginal or “critical” density of the Essence, and if so, then in this state the Essence should experience a need of a phase transition in order to “rid” of this critical density and to reduce it. Most likely the Essence gets out from this state “explosively” and passes to another.

According to the theory of "Hot big bang" this is the beginning and the birth of the Universe and the point of singularity, i.e. of invalidity of the known laws of physics. In accordance with the hypothesis of [4] this is not a point of singularity, but it is equivalent to all other points and periods in the evolution of the fundamental Essence and the substance, with specific values of physical parameters, when through a jump or by a slower process from the Essence primary formations “condense” or the known elementary particles, having a density in the range of 10^{13} - 10^{14} g/cm^3, i.e. significantly higher than that of the Essence, from which they originate.

It should be noted that in such an approach and explanation of the origin and the structuring of elementary particles, there is no question about what gives them mass. As well as the searching for the alleged X-boson, which the modern science insistently looks for as a reason and beginning of their genesis. Is not it logical the idea that no one gives a mass of particles, they just retrieve it from the Essence by condensing and concentrating thereof and in its environment? More likely X-boson as physical attributes and parameters could be a long gone phase at the structuring of the elementary particles, could be a form of the early stages of their formation, intermediate unit between the Essence and the substance in its next phase of evolution and now its search and finding is meaningless. Figuratively speaking, this event or process can be considered like a start and emergence of the known matter or substance, conditionally named "bright” matter in which, naturally, the density of the Essence or conditionally again “dark” matter has fallen to a value of 10^5 g/cm^3 and the average density of the substance occurs increased and accepted the value of 10^{-28} g/cm^3. This particular value the contemporary science considered “critical”, without a clear reason for this. Because it is difficult to find an obvious and convincing reason of transferring the majority of the Essence into substance, but becomes exactly and only that. Therefore, it is more objective, the Essence value of 10^8 g/cm^3 to be considered as a 'critical', since at this value there is a need for a phase transition and change the values of the density and also switching to another extreme state, corresponding to the bottom row in the table.

What should be the chain farther? Natural process, based on experience and knowledge of physics, chemistry, astronomy and other sciences, hereinafter the new final state must follow the evolution towards baseline condition. Reducing the average density of the substance due to radiation of energy, respectively mass, and the overflow back to the primary Essence resulting in increased density of Essence again to reach the marked above marginal or “critical” value.

This sequence is a possible chain in the main eternal and unending circle in the Universe, cycle of transformation of Essence into matter and vice versa.

What consequences can have the alleged circle or the cosmological cycle?

The last column of the table indicates that the ratio of the densities of the essence and the average density of the substance also vary within certain limits, i.e. the state of the Essence and the substance, albeit very slowly with respect to the time scale, change within specified limits. Since the density of the Essence and the substance is variable in time, then it seems logically another parameters and also the parameters of the processes developing in them must be as well as of variable values. For example, the speed of electromagnetic oscillations, which are the product of the Essence and the substance should be a variable, i.e., not a constant. The speed of electromagnetic oscillations can be regarded as constant only in a very large time scale.

Of interest is the question concerning duration of this universal cycle. On the base of the ratios and proportions in the table and the known age of the Universe, according to the science is of the order of 13-15 (13.7) billion years, it may be concluded, that the current stage of the Universe evolution is somewhere around the late third and the beginning of the final quarter of the cycle. Therefore, the total duration of the alleged cosmic cycle must be of the order of 17-20 billion years. On the other hand, according to the theoretical justifications and calculations, relating to the on the duration and the balance of the two main types of reactions in suns, shown in one of the fundamental works of the famous astrophysicist Schwarzschild [5], the residual resource of the suns and the solar systems from their main continuity to the attenuation, fading and the energy respectively the mass releasing into the Essence, could be determined to a value of the order of 50-60 billion years. Namely, the duration of the cosmological cycle is going to be of the order of 70-80 billion years.

As can be seen, the difference in the two estimates made by two independent approaches is essential, which requires serious research to establish a more reliable value for the duration of the basic universal cycle. One of the emerging opportunities in this regard is the detection and identification of the cause or factor determining accelerated, inflation transition from substance to Essence, which could bring the two values to acceptable differences. Another option is to precise and clarify the current age of our Universe. Which of the two options is more worthwhile in trying to establish with greater precision the length of the universal cycle is a matter of further research.

Finally, it should again be paid attention to relationship 10^{37}, since it was set and used as a defining in the analyses, calculations and conclusions in the report. Already specified, that besides the ratio between the densities of the Essence and the substance, it also expresses the proportion of the forces or the intensity of the gravitational and the electromagnetic interactions. In [4] is justified and shown that gravity and gravitational interactions respectively and waves are not real physical phenomena or processes and their effect is due to the pressure of the physical Essence on the material bodies formed from it in its environment. So that the ratio of 10^{37} should reflect the proportions and dimensions, responsible and consistent with the mutual influence of the Essence and substance in the process of their transformation and evolution, including electromagnetic interactions, which is their product.

As a result of the implemented studies, presented in the report, are created prerequisites for clarification of a number of not yet sufficiently well understood by the modern science questions about the structure and the processes developing in the world around us. Summarized and briefly expressed, the new information consists in the fact that all structures and processes in the Universe arise from real physical Essence, with certain physical parameters and develop cyclically in unending cycle.

References

1. Шмутцер, Э. Теория относительности. Современное представление. Изд. „Мир”, Москва, 1981.
2. Эйнщейновский сборник, Москва, 1966.
3. Valev, D. Consequences from conservation of the total density of the Universe during the expansion” and “Estimations of total mass and density of the observable Universe by dimensional analysis, Aerospace Research in Bulgaria № 24, Bulgarian Academy of Sciences. Sofia, 2012.
4. Velkov, V. Hypothesis of a Cosmological Model of the Universe without Gravitation. Aerospace Research in Bulgaria № 26. Bulgarian Academy of Sciences, Sofia, 2014.
5. Martin Schwarzschild. Structure and evolution of the stars. Princeton, New Jersey, 1958. В превод на руски: М. Шварцшильд. Строение и еволюция звезд, Изд. „Иностранная литература”, Москва, 1961.

ОСНОВЕН ВСЕМИРЕН КРЪГОВРАТ

В. Велков

Резюме

Докладът представя идея за кръговрат на преобразуване на основополагаща физическа същност, изпълваща всемирното пространство, във вещество и обратно. Определени са вероятните числени стойности на плътността на същността и средната плътност на веществото във Всемира при това преобразуване, границите на тяхната промяна и съотношението им. На тази база е показано, че за „критична” би следвало да се приема не сега приетата средна плътност на веществото 10^{-28} g/cm^3 във всемирното пространство, а нова стойност, характерна за плътността на основополагащата същност. Предложени са също така два подхода за определяне на периодичността на предполагаемия всемирен кръговрат.

Bulgarian Academy of Sciences. Space Research and Technology Institute.
Aerospace Research in Bulgaria. 27, 2015, Sofia

Hypotheses

A NEW EXPERIMENT TO DETERMINE THE GALAXY SPEED OF EARTH IN SPACE

Dimiter Stoinov

e-mail: dgstoinov@yahoo.com

Abstract

In this article is discussed the question of the speed at which the Earth moves in space. Until now, this speed has not been determined with sufficient accuracy. Many astronomers believe that Earth with the Sun moves, relative to the observed galaxies, near a rate of 600 km/s, but the opinions of scientists fluctuate widely, between 130 km/s and 1000 km/s. This is because until now conducted experiments primarily with satellites Prognoz-9 (USSR) and COBE (USA), besides being expensive are also inaccurate. Discussed is also the possibility to conduct an experiment, on Earth's surface, through which the speed as well as and direction of Earth's movement in space could be more accurately determined. It is noted that this experiment will be thousands times cheaper than experiments with artificial satellites.

Introduction

Along with the annual movement the Earth is involved in the galactic motion of the Solar system. It is therefore pertinent to ask the question: What are the speed and the direction of Earth's movement in space? To give a straightforward answer is difficult. Existing data are contradictory. In 1933 Dayton Miller [1] stated that, their research with Michelson-Morley interferometer yielded the result that the Earth is moving towards constellation Dorado with a speed of 208 km/s. In 1983 the Soviet Union launched satellite "Prognoz-9" to study the so-called "relict radiation". As a result of the observations made, and based on the basic model of the Solar system movement into space, it was reported that it moves at a speed of around 515 km/s in the direction of the constellation Virgo. With the same purpose in 1989 the US launched its satellite COBE. Within the accuracy of monitoring tools it is assumed that the speed of the Earth and the Solar System is about 600 km/s. Although many astronomers now accept that the Earth and the Sun move relatively to the observed galaxies in the vicinity of approximately 600 km/s; the values of this speed vary enormously between 130 km/s and 1000 km/s.

The Fresnel-Einstein Dilemma

In 1818 Fresnel [2] derived the following formula for speed of light propagating in an optical (transparent) medium

$$u = u_0 \pm V\left(1 - \frac{1}{n^2}\right), \tag{1}$$

where $u_0 = c/n$ is the speed of light in an optical medium (presumed to be at rest), c is the speed of light in vacuum, V is the speed of the Earth in space, and n is the refractive index.

The point of view of Fresnel is that formula (1) reflects a real change in the speed of propagation of light in a given optical medium. Contrarily, the point of view of relativists is that formula (1) is wrong because there is no change in the speed of light, based on Einstein postulate that the speed of light is independent of the state of motion, i.e. the speed of light in an optical medium at constant rectilinear motion must equal the speed of light at rest.

The question of the physical meaning of Fresnel formula

To substantiate formula (1) Fresnel assumes that the change in the speed of light is due to change in the ether density. However, this hypothesis is unacceptable and this wrong hypothesis is the reason that the Fresnel formula was rejected and misunderstood by the scientists. But the meaning of formula (1) is quite simple to understand; if for example, one holds a piece of glass or a magnifying glass in his/her hand and move it around, than the speed of light inside the glass medium will change because we are dragging the light by the hand movement. The same argument goes for the Earth and all celestial bodies. As Earth moves across the space, the speed of light propagating in any optical medium residing on Earth (air, water, etc.) should change because of that movement.

There is a way to justify the Fresnel formula if we consider two very important starting points [6]: 1) the principle of Huygens-Fresnel in Optics, and 2) the fact that only atoms and molecules of chemical elements emit light waves.

The principle of Huygens-Fresnel states that when a luminous disturbance reaches a point, each point becomes a source of secondary waves. However, a “point” is nothing more than an abstraction. It is therefore reasonable to ask ourselves: What is the real physical object able to replace the point so that the object can radiate real light waves? The answer to this question is easy. Where Huygens and Fresnel put points we should consider atoms or molecules of the relevant optical medium.

In an earlier article [6] we compared the way of propagation of light to the propagation of radio and television broadcasts by a chain of relay stations. This is one way to reduce energy losses in retransmission. Apparently, nature chose the same more effective way to propagate light waves. Thus, according to the principle of Huygens-Fresnel, the energy of the excited atoms is transmitted first to the closest atoms-repeaters, which in turn transmit it to the next ones, etc. i.e. from one repeater to another until it reaches the recipient atoms. Every atom emitting a light wave with certain frequency must find atoms repeaters tuned to that frequency, so that a large number of spectral lines can be transported simultaneously. Thus, each atom repeater becomes a source of secondary spherical waves, as follows from the principle of Huygens-Fresnel.

The efficient transfer of energy is only one side of the problem. It is not gratuitous as there is some sacrifice in terms of the speed. It is because energy transfer between atoms repeaters is not instantaneous but takes some time. Time losses are of two different kinds: 1) the time taken by the atom repeater to accept and send optical signals; 2) the time it takes for the light signal to reach the next atom repeater. Therefore, the average speed of light depends on the distance between the atoms repeaters and their number in the optical medium. When the mass density of the medium is less, there will be greater average distance between the atoms repeaters and greater speed of propagation of light and vice versa, an optical medium with greater mass density will have less average distance between the atoms repeaters and therefore smaller speed of propagation of light. This is in line with the fact that the greater the number of atoms repeaters, the more time is lost to retransmit signals. The different refractive indices of different optical media can be explained in this way.

Now regarding to the most important question: “How to explain the relation between the movement of the optical medium through the ether and the average distance between atoms repeaters?”. When waves travel in a continuous medium, such as air, water, ether, etc., we introduced a particular feature we call [6] delayed/overtaking position, respectively lagging/outpacing potential. It reflects the fact that when the oscillator and the receiver are moving the path of the waves travelling to the moving receiver changes. The conclusion is apparent: If we consider light propagation in a moving optical medium (with reference to the static ether) then the distance the waves travel, between atoms-retranslators, will change. Therefore, the number of intermediate repeaters will change. In addition, that means that the time for signal retransmission will change and in result, so will the speed of propagation of light. In this way, we reach to an explanation of the physical meaning of Fresnel formula.

Proposed experiment

In essence, the proposed experiment is similar to the classical experiments to determine the speed of light. However, while the objective of classic experiments was to determine it quantitatively, here the objective is different, to determine whether this speed undergoes changes, i.e. whether it depends on the movement of the Earth in space. In [4] a test setting, similar to that used in Fizeau experiment in 1849, was described. Here we offer experimental setup similar to the one used by Karolus-Mittstaedt in 1928 [7].

The schematic diagram of the experimental setup is shown in Fig. 1. Light from a laser 1 passes through the optical shutter (modulator) 3 located between two crossed polarizers 2 and 4 and then passes through the elongated optical fiber coil 6 (entry point 5 and exit point 7), then it falls and is reflected by a moving mirror 8. The reflected light returns after passing through a second elongated coil of optical fiber 10 (entry point 9 and exit point 11) and reaches a second optical shutter (modulator) 12, thereafter via polarizer 13 falls on a photo element 14. The resulting output electric signal is amplified by the amplifier 15 and is fed to an oscilloscope or recorder 16.

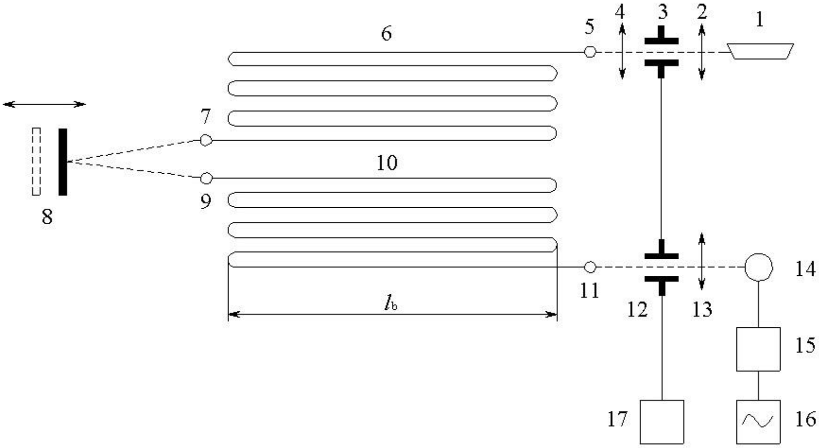

Fig. 1. Scheme of the experimental set-up: 1 - lasers; 2, 4 and 13 - crossed polarizers; 3 and 12 - optical shutter (modulator) of crystal KDP; 6 and 10 - oblong coils (antennas) of the optical fiber; 5 and 7 - inputs and 9 and 11- outputs of the light into the optical fiber; 8 - mobile mirror; 14 - photocell; 15 - amplifyer; 16 - oscilloscope or recorder; 17 - generator. l_b *- length of the double coil of optical fiber*

The experiment runs as follows. The entry optical shutter 3 modulates the light signal and produces a wave sequence (Zug) of duration (opening time)

$$t_{\otimes} = \frac{1}{2f}, \tag{2}$$

where *f* is the operating frequency of the generator 17.

Since the two optical shutters 3 and 12 operate synchronously, the amount of light reaching the photo element 14 is determined by the ratio

(3) $$\frac{t_\mathrm{P}}{t_\otimes},$$

where t_P is the travel time for which the light beam travels the path between optical shutters 3 and 12.

If the ratio (3) between the travel time t_P and the opening time $t_\otimes$ of (2) is an integer number,

(4) $$\frac{t_\mathrm{P}}{t_\otimes} = m,$$

where *m* is an integer, then maximum light will reach the photoelement 14 and maximum electric signal will be registered. In this case, the light signal transmitted by the entry optical shutter 3 will arrive to the exit optical shutter 12 precisely when it is open, so a maximum light will pass. Vice versa, if the ratio (3) is of the kind

(5) $$\frac{t_\mathrm{P}}{t_\otimes} = m + \frac{1}{2},$$

then the output electric signal from the photoelement 14 will have a minimum value. In this case, the light signal transmitted by the entry optical shutter 3 will arrive to the exit optical shutter 12 when it is closed and therefore a minimum amount of light will pass.

The time needed for the optical signal to travel between the two optical shutters 3 and 12 is determined as (Appendix A equation (A17))

(6) $$t_\mathrm{P} = \frac{2l}{c}n + \frac{2l}{c}n^3\left(\alpha^2 - 2\alpha\right)\frac{V^2}{c^2},$$

where *2l* is the light path through the elongated optical fiber coils (antennas) 6 and 10, and

(7) $$\alpha = 1 - \frac{1}{n^2}$$

is the so called Fresnel coefficient of ether drag.

Obviously, the travel time (6) depends on the velocity *V* of the elongated optical fiber coils (antennas) movement through space. When this velocity changes, the speed of propagation of light inside them will change as well. This will affect also the travel time t_P. Therefore, the output electric signal from the photo element 14 will change and the oscilloscope or recorder 16 can register this.

The two points of view

There are two viewpoints as to whether in the above experiment the speed of light will change or not, and whether the output signal from the photo element 14 will change.

a) The point of view of the relativists - According to the principle of relativity of Einstein the speed of light in an optical medium must be constant and does not depend on whether the optical medium is in motion or not. Therefore, the travel time t_{P}, needed for the light to travel the path between the two optical shutters 3 and 12, will be constant ($t_{\text{P}} = const$). In this case the relationship (3) should not change with the time, i.e. under the special theory of relativity we will have

$$\frac{t_{\text{P}}}{t_{\otimes}} = const\,. \tag{8}$$

Therefore, the output signal from the photo element 14 should not change.

It must be underlined that in the special theory of relativity no object in space can have an absolute speed as there is no absolute inertial system providing a frame of reference to determine the movement of celestial bodies absolutely, i.e. every movement must be determined with reference (in relation) to another object.

b) The point of view of Fresnel - In Fresnel's formula the speed of light in a given optical medium depends on the speed V of movement of this optical medium with reference to the ether. Therefore, the travel time t_{P}, for the light to travel the path between the two optical shutters 3 and 12, will depend on that speed because equation (6) is a function of it.

Obviously in this case the relationship (3) between the travel time t_{P} and the opening time of the optical shutter $t_{\otimes}$ will be

$$\frac{t_{\text{P}}}{t_{\otimes}} = \frac{2l}{t_{\otimes}c}n + \frac{2l}{t_{\otimes}c}n^3\left(\alpha^2 - 2\alpha\right)\frac{V^2}{c^2}\,. \tag{9}$$

It is obvious that (9) is a function of the speed V and if this speed changes then the amount of light that passes through the two optical shutters should change. Therefore, the observed output signal from the photoelement 14 should also change.

Calculating the necessary optical path

We need to calculate the necessary length of the optical path in order to fulfill the condition to observe maximum and minimum output signals. To this end, it is necessary that the ratio (9) has values of 1/2, i.e.

(10) $$\frac{\Delta t_{\mathrm{p}}}{t_{\otimes}} = \frac{2l\,n^3}{t_{\otimes}c^3}\left(\alpha^2 - 2\alpha\right)V^2 = \frac{1}{2},$$

where *V* is the speed of movement of the optical fiber coils 6 and 10. We will take into account only the variable portion, i.e. the second term of equation (9)

If we resolve equation (10) with regard to the optical path *l* we get

(11) $$l = \frac{c^3}{4n^3(\alpha^2 - 2\alpha)}\frac{t_{\otimes}}{V^2} .$$

Now provided that the constants in (11) are as follows:

$c = 3\text{x}10^8\left[\frac{\mathrm{m}}{s}\right]$ is the speed of light;

$n = 1,46$ is refractive index of the optical fiber;

$\alpha = 1 - \frac{1}{n^2} = 0,53$

and we substitute in (11) then the result for the optical path will be the following formula

(12) $$l \approx 2,78\text{x}10^{24}\frac{t_{\otimes}}{V^2}\left[\mathrm{m}\right].$$

Now, if instead of the opening time $t_{\otimes}$ we substitute its equal from (2), we will get

(13) $$l \approx 1,39\text{x}10^{24}\frac{1}{f\,V^2}\left[\mathrm{m}\right].$$

Application of experimental setup (Fig. 1) to determine the speed of Earth in space

It must be said that our original idea was to use this experimental setup for verification of the principle of relativity of Einstein [4, 5]. It was planned to place the optical fiber coils 6 and 10 parallel to the Earth parallel, and to relate the change of speed *V* to the daily and annual movements of the Earth. However, there is a problem connected with the excessive length of the optical path. For example, if we use an optical shutter with an operating frequency f = 0,6 GHz as used in [8] and assumed speed of the setup and the daily motion on the Earth with speed in range between 0 and 200 km/s, then the length of the optical path gets about $l \approx 60\ \text{km}$, i.e. the total optical path that optical signals must travel in both coils must be $2l \approx 120\ \text{km}$.

One possibility to put this result into practice (with significantly reduced optical path length) is to create a cosmic compass [9]. Figure 2 shows a schematic diagram of a hand-operated cosmic compass. It consists of a mast antenna with counterweight 1, rotating platform 2, and base 3. Coils 6 and 10 are wound on the mast antenna 1. In this way it will be possible to establish the direction of Earth motion by detecting the maximum signal on the recording device.

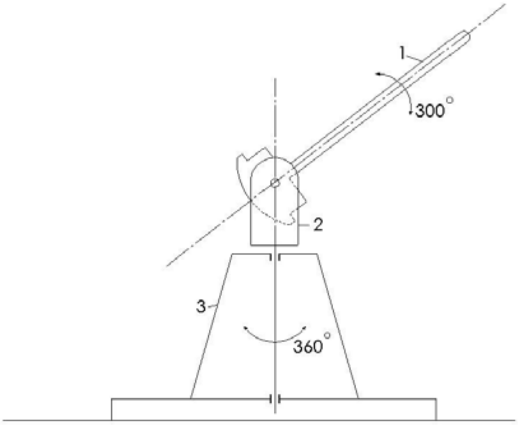

Fig. 2. Scheme of terrestrial cosmic compass

The advantage of this setup is that the full galactic speed of the Earth may be derived from formula (13) instead of its projection with reference to the location of the experimental setup. For example, if we assume that this speed is within the range 400 ÷ 600 km/s, then for the necessary optical path length we receive:

- in optical shutter f = 0,6 GHz and V = 400 km/s

$l \approx 14480$ m and $2l \approx 28960$ m

- in optical shutter f = 0,6 GHz and V = 600 km/s

$l \approx 6435$ m and $2l \approx 12870$ m.

Different options are possible, keeping in mind the varying data for Earth galactic speed.

Experimental method

It is important in the beginning to establish whether the rotation of the antenna affects the output signal or not. If it turns out that the signal does not change, this will mean that the special theory of relativity is correct. In this case, the experiment shall be terminated. Conversely, if the output signal is changed, this will mean that Fresnel is right and the experiment shall continue.

The following important notes have to be made:

1. The cosmic compass should be positioned so that the mast antenna rotates in the plane of earthly meridian.

2. The moving mirror 8 is used for calibration. By moving the mirror we may find respective positions corresponding to maximum or minimum output signal. The distance between two positions with observed maxima of the output signal is:

(14) $$\Delta l = \frac{c}{4f} .$$

For the chosen operating frequency $f = 0,6$ GHz of the optical shutters this distance is $\Delta l = 12,5$ cm. In this case, the movable mirror should be able to be shifted to at least 15 ÷25 cm.

At the beginning of the experiment, by rotating the antenna, two positions with observable maximum and minimum in the output signal, must be found. One of these positions corresponds to a case where the mast-antenna is directed along the direction of motion of the Earth, and in the other position, the mast antenna is perpendicular to that direction. This is the "zero" position of the antenna.

Having established the zero position of the antenna, using the movable mirror two positions with maximum signal should be found and then the mirror should be positioned in the middle. The difference between the maximum and minimum output signal should also be determined. This is actually the calibration of the setup.

Now we can begin the main experiment. In the course of 24 hours periodically, for example once every 15-20 minutes, we must seek the two positions of the antenna showing a maximum and minimum signal and calculate the difference between the maximum and minimum signal $(\Delta \mathrm{I})$. We must seek positions of the antenna where this difference is greatest. It is in this case that there will be complete coincidence of the direction of the antenna with the direction of the Earth. We should take a record of the antenna coordinates in this position and then we will be able to determine the speed of the Earth.

(15) $$V = V_{cb} \frac{\Delta \mathrm{I}}{\Delta \mathrm{I}_{cb}} .$$

It should be noted that in each measurement we determine the summary movement of the Earth, i.e., its orbital speed plus the galactic speed. To determine more precisely the direction of the galactic motion it will be necessary to take measurements for a full year. In this case, the tip of the vector sum of the Earth velocities will delineate an oval curve on the celestial sphere. The center of this oval curve will determine the direction of the galactic speed.

The proposed experiment and contemporary optical technologies

The optical path length depends largely on the operating frequency *f* of the optical shutters (modulators). Research established that there are commercially available electro-optical shutters (modulators) based on $LiNbO_3$ crystal with an operating frequency ≥ 40 GHz [10, 11]. Very suitable for the purpose are the modulators of the company Optilab [11], which have built-in polarizers. When using electro-optical modulators of this type the experimental setup may be significantly simplified (Fig. 3).

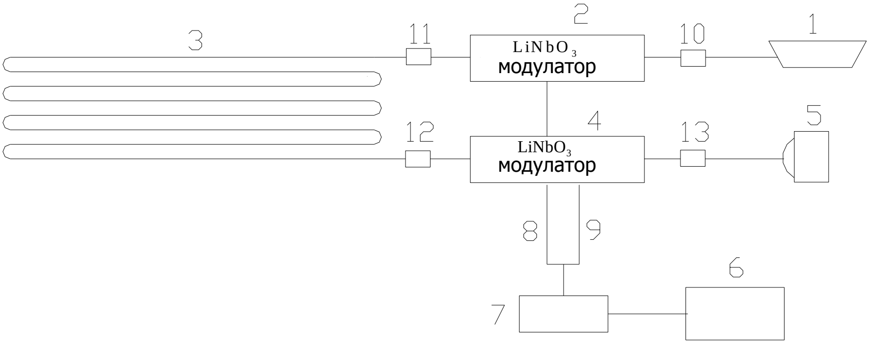

Fig. 3. Experimental set-up with integrated polarizers
1 - lasers; 2 and 4 - incoming and outgoing optical shutter (modulator) of crystal $LiNbO_3$; 3 - oblong coils (antenna) of optical fiber; 5 optical power meter; 6 - signal generator; 7 - driver amplifier; 8 and 9 - RF cables; 10, 11, 12, and 13 - optical connectors.

This experimental installation is no different from the described above in its operating principle. The light from the laser 1 passes through entry 2 and exit 4 electro-optical shutters (modulators) and via elongated coil of optical fiber 3 reaches the optical power meter 5. Since the two electro-optical shutters operate synchronously, the amount of light that will pass through them will depend on the relationship (3) between the travel time t_P and the opening time $t_\otimes$ of the optical shutters, i.e. everything said above here remains in force.

However, there is no movable mirror here. In this case, the calibration may be accomplished by amending the frequency of the signal generator.

Regarding the operating frequency of electro-optical modulators we want to note that would be reasonable to choose operating frequency of $f = 9$ GHz. We must keep in mind that a signal generator operating at the same frequency will be needed. Here we also take into account that the elongated coil of optical fiber is single and light travels in both directions ($L = 2l$). In this case, the optical path length will be:

$$L \approx 2,78\text{x}10^{24} \frac{1}{f V^2} \left[\text{m}\right] \tag{16}$$

- with optical shutter $f = 9$ GHz and $V = 600$ km/s

$$L \approx 858\,\mathrm{m}$$

- with optical shutter $f = 9$ GHz and $V = 400$ km/s

$$L \approx 1930\,\mathrm{m}\,.$$

Finally, let consider the length of the elongated coil of optical fiber and the respective length of the mast antenna. It depends on the location of the cosmic compass. A length of 5 to 10 m would be sufficient. If needed, the length of the mast antenna may be reduced up to 2-3 m; however, it should be kept in mind that in this case the error in determining the direction of motion of the Earth will increase.

Conclusions

If during rotation of the mast antenna in the plane of the meridian the output signal does not change, it will mean that the truth is on the side of Einstein. This means that the principle of relativity is correct. Conversely, if during a rotation of the antenna in the plane of the meridian the output signal changes, this means that the truth is on the side of Fresnel. In this case, it will be possible to determine the direction and speed at of Earth motion in space.

We are convinced that the truth is on the side of Fresnel!

Appendix A. Calculation of the time which is needed light to travel the optical path between the electro-optical modulators 3 and 12 (Fig. 1)

The classical formula for calculating the time in which light travels a given distance is:

$$time = \frac{\text{distance}}{speed}\,.$$

However, this classical formula is not applicable here. Here variables are as the distance also and speed. It is a fact that when the light travels a given distance twice once in the direction coincident with the direction in which to move the optical medium and vice versa are appear two important features, namely:

- The first feature is related to the Fresnel's formula (1). When the direction coincides with the direction of movement of the optical medium, the speed of propagation of light must be $u_0 + V\alpha$, and when these directions are opposite, the speed of propagation of light must be $u_0 - V\alpha$ where,

(A1) $$\alpha = 1 - \frac{1}{n^2}$$

is so-called Fresnel's coefficient for partial dragging of the ether, and *n* is the refractive index.

- A second feature relates to the fact that as a result of so-called delayed / preemptively position, the distance which the light must travel in both directions are different from the actual physical length l of the optical medium, i.e. this distance changed [4]

To make it more clear the above we first define the time, which is needed by light to travel the distance between electro-optical modulators 3 and 12 taking into account the physical length of the optical medium.

1. Determining the time to travel t_P when the distance l is physical length of the optical path.

In this case the time for which the light travels twice the path l must be

$$t_\mathrm{P} = \frac{l}{u_0 + V\alpha} + \frac{l}{u_0 - V\alpha} \tag{A2}$$

and after bringing (A2) in common denominator

$$t_\mathrm{P} = 2l \frac{u_0}{u_0^2 + (V\alpha)^2} = \frac{2l}{u_0} \frac{1}{1 - (V\alpha)^2 / u_0^2} \tag{A3}$$

and account of the fact that the relationship V^2 / u_0^2 is small quantity can be accepted

$$\frac{1}{1 - (V\alpha)^2 / u_0^2} \approx 1 + \frac{V^2}{u_0^2} \alpha^2 \tag{A4}$$

and will obtain

$$t_\mathrm{P} \approx \frac{2l}{u_0} \left(1 + \frac{V^2}{u_0^2} \alpha^2 \right). \tag{A5}$$

After taking $u_0 = c/n$ into account and replace in (A5) after appropriate conversions we will have

$$t_\mathrm{P} = \frac{2l}{c} n + \frac{l}{c} \frac{V^2}{c^2} 2n^3 \alpha^2 . \tag{A6}$$

However, it should be noted that the time (A6) is only a rough approximation. For a more precise definition of that, time should be taken into account and "increase" or "shortening" of this time as a result of so-called delayed / preemptively position [4].

2. Determining the time to travel t_P in the case when taking into account “increasing” or „reducing” of the optical path.

In this case the time for which the light travels twice the path between the two optical modulators will be

(A7) $$t_{\mathrm{P}} = \frac{l+\Delta l_+}{u_0+V\alpha} + \frac{l-\Delta l_-}{u_0-V\alpha},$$

where additives in both the numerator addends in (A7) are "extension" or "reduction" of the optical path.

To determine additives Δl_+ and Δl_- is starting from the following considerations. Time t for which the light beam travels the distance l, movable mirror will move on distance Δl_+ or Δl_-. Therefore, there will be in force proportions:

- for the case where the direction of light coincides with the direction of the Earth

(A9) $$t = \frac{l}{u_0+V\alpha} = \frac{\Delta l_+}{V}$$

- for the case where the direction of light opposes with the direction of the Earth

(A10) $$t = \frac{l}{u_0-V\alpha} = \frac{\Delta l_-}{V}$$

i.e. we will have

$$\Delta l_+ = l\frac{V}{u_0+V\alpha}$$

$$\Delta l_- = l\frac{V}{u_0-V\alpha}$$

and substituting in (A7) will be obtained,

(A11) $$t_{\mathrm{P}} = \frac{l+\Delta l_+}{u_0+V\alpha} + \frac{l-\Delta l_-}{u_0-V\alpha} = \frac{l+lV/(u_0+V\alpha)}{u_0+V\alpha} + \frac{l-lV/(u_0-V\alpha)}{u_0-V\alpha} =$$

$$= l\left(\frac{1}{u_0+V\alpha} + \frac{1}{u_0-V\alpha}\right) + lV\left[\frac{1}{(u_0+V\alpha)^2} - \frac{1}{(u_0-V\alpha)^2}\right].$$

Now (A11) is brought to a common denominator

(A12) $$t_{\mathrm{P}} = l\frac{2u_0}{u_0^2-V^2\alpha^2} - l\frac{4u_0V^2\alpha}{(u_0+V\alpha)^2(u_0-V\alpha)^2}\ .$$

But as here the product $(u_0+V\alpha)^2(u_0-V\alpha)^2 = \left(u_0^2-V^2\alpha^2\right)^2$ the equation (A12) will acquire type

(A13) $$t_P = l\frac{2u_0}{u_0^2 - V^2\alpha^2} - l\frac{4u_0V^2\alpha}{\left(u_0^2 - V^2\alpha^2\right)^2}.$$

Let the common multiplier in (A13) be subtracted before the brackets

(A14) $$t_P = \frac{2lu_0}{u_0^2 - V^2\alpha^2}\left(1 - \frac{2V^2\alpha}{u_0^2 - V^2\alpha^2}\right)$$

Equation (A14) can also be simplified if it is removed before the brackets and u_0^2

(A15) $$t_P = \frac{2l}{u_0}\frac{1}{1 - V^2\alpha^2/u_0^2}\left[1 - 2\alpha\frac{V^2}{u_0^2}\frac{1}{1 - V^2\alpha^2/u_0^2}\right]$$

and taking into account the (A4) we will have

(A16) $$t_P \approx \frac{2l}{u_0}\left(1 + \frac{V^2\alpha^2}{u_0^2}\right)\left(1 - \frac{2V^2\alpha}{u_0^2}\right).$$

Now once you do multiplication and ignore values of the fourth order for the time t_P to get

(A17) $$t_P \approx \frac{2l}{u_0}\left[1 + \frac{V^2}{u_0^2}\left(\alpha^2 - 2\alpha\right)\right].$$

Here in (A17) after substituting $u_0 = c/n$ will give final

(A18) $$t_P = \frac{2l}{c}n + \frac{2l}{c}n^3\left(\alpha^2 - 2\alpha\right)\frac{V^2}{c^2}.$$

References

1. Miller, D., The Ether-Drift Experiment and of the Absolute Motion of the Earth, Review of Modern Physics, volume 5, 1933, p. 234.
2. Fresnel, O., Sur l'influence du mouvement terrestre dans quelques phenomenes d'optique, Ann. Chim. et phys., 9, 57, 1818 (in French).
3. Fizeau, H., Sur les hypotheses relatives a l'ether lumineux et sur un experiment qui parait demontrer que le movement des coros change la vitesse, avec laquelle la lumiere se propage dans leur interieur, C. r., 33, 1851 , pp. 349-355 (in French).
4. Stoinov, D. G., Stoynov D. D., 2013 The dilemma: Fresnel's formula or the principle of relativity of Einstein, https://sites.google.com/site/dgstoinov/.
5. Stoinov, D. G., Stoynov D. D., 2014. The dilemma Fresnel-Einstein: Whether the speed of light dependent by the Earth's motion in space" (open letter), https://sites.google.com/site/dgstoinov
6. Stoinov, D. G., Stoynov D. D., 2014. The physical meaning of the Fresnel formula, https://sites.google.com/site/dgstoinov/

7. Karolus, A., Mittelstaedt O. Die Bestimmung der Lichtgeschwindigkeit unter Verwendung des elektrooptischen Kerrefektes, Phys. ZS. 1928, 29 **s**., pp. 698-702 (in German).
8. Marchenko, O. M., Mihalev V. S., Penykov S. N. Demonstration option definition speed of light in air - Vestnik Leningradskogo Unyversiteta, № 16, 1978, pp. 132-134 (in Russian).
9. Stoinov, D. G., Patent Application № 112022/27.05.2015 - Antenna for space compass, (in Bulgarian).
10. New Focus Optical Modulators, URL: http://www.newport.com/New-Focus-Optical-Modulators/994983/1033/content.aspx?icid=srch-lnk-0029
11. Optical Modulators, up to 40 GHz, PM type, http://www.oequest.com/cat/1164

ЕДИН НОВ ЕКСПЕРИМЕНТ ЗА ОПРЕДЕЛЯНЕ ГАЛАКТИЧНАТА СКОРОСТ НА ЗЕМЯТА

Д. Стойнов

Резюме

Поставя се въпроса за на скоростта, с която Земята се движи в космоса. До сега тази скорост не е определена с достатъчна точност. Много астрономи считат, че Земята заедно със Слънцето се движи спрямо наблюдаваните в близост галактики със скорост 600 km/s, но мненията на учените се колебае в широки граници, между 130 km/s и 1000 km/s. Това се дължи на фактът, че провежданите до сега експерименти преди всичко на изкуствени спътници на Земята *Прогноз 9* (СССР*)* и *COBE* (САЩ)*,* освен че са скъпи са и неточни. Разглежда се възможността да се проведе експеримент, тук на повърхността на Земята, без да се излиза в космоса, чрез който по-точно да се определи, както скоростта също така и посоката и на движение. Отбелязва се, че този експеримент ще бъде хиляди пъти по-евтин от експериментите с изкуствени спътници.

New Books

AN INTERESTING AND USEFUL NEW BOOK

Recently, a new book – “Remote Aerospace Technologies Fundamentals (in Ecology and Environment Studies)”, a publication of New Bulgarian University in Sofia, was issued. The book is dedicated to an interesting and attractive subject, namely the technologies for remote sensing of Earth, which is an exceptionally capable and efficient means for solving some of the global problems of our civilization – the problems of environment and its protection.

The author – professor, DSc of technical sciences and PhD in physics Garo Mardirossian – is a prominent scientist in the field of remote sensing of Earth and outer space. He has been working in this area for more than 35 years as a member of the Space Research and Technology Institute at the Bulgarian Academy of Sciences (SRTI-BAS), taking part in all large Bulgarian and international projects with Bulgarian participation about remote sensing of Earth. This is his fifth book running on this subject area.

Prof. Mardirossian gives prominence to the physical methods for remote sensing of Earth and space. The book discloses in detail the technologies, methods, apparatuses, and systems used by researchers to obtain remote sensing data about Earth and space either by means of satellites or aerial flights of manned and unmanned aircraft. A concise description is presented of aerial and space vehicles used for such studies such as balloons, aerostats, geophysical rockets, airplanes, helicopters, satellites, piloted spacecraft, space shuttles, and orbital stations. The author scrutinizes topics about the orbits commonly engaged for these tasks and the visual studies of Earth’s orbit, optimal space systems for continuous Earth monitoring, ground-based systems, and the complex synchronous aerospace experiment. Dedicated space in the book is allotted for the most significant achievements of the Bulgarian scientists and specialists in this field.

The book is written in an easy-to-read language. It is perceived that it makes it very suitable for a large readership, i.e. older and younger, skilled and novices students, who seek to learn the classical and contemporary methods and devices in the world used for remote sensing of the Earth as well as to acquaint themselves to the achievements of Bulgaria in space sciences.

The beautiful colour Appendix shall provide not only knowledge but also aesthetical pleasure to the observer. The attractive cover and the perfect graphical material impress the reader. Also very useful is the alphabetical index that significantly facilitates the reader to locate the topic of interest.

Such books are rarity even on a world scale. It could be claimed that with this book the Bulgarian reader has on his disposal one new and beneficial book, presented in an attractive scientific way, for the perspective scientific field of remote sensing of Earth.

Eng. Svetoslav Zabunov, PhD

Мардиросян, Г. Основи на дистанционните аерокосмически технологии. Нов български университет, 2015, 224 с.